NUMERICAL MODELING OF SOLID OXIDE FUEL CELL

ZHENG KEQING

Ph.D
The Hong Kong Polytechnic University
2016

The Hong Kong Polytechnic University
Department of Building and Real Estate

Numerical Modeling of Solid Oxide Fuel Cell

ZHENG Keqing

A thesis submitted in partial fulfillment of the
requirements for the degree of Doctor of Philosophy

October 2015

CERTIFICATE OF ORIGINALITY

I hereby declare that this thesis is my own work and that, to the best of my knowledge and belief, it reproduces no material previously published or written, nor material that has been accepted for the award of any other degree or diploma, except where due acknowledgement has been made in the text.

________________________________ (Signed)

__________Keqing Zheng___________ (Name of student)

ABSTRACT

Solid oxide fuel cell (SOFC) has attracted much attention for its great potential in solving the energy and environmental dual crisis. One major limitation for SOFC commercialization is its high cost, which can be decreased either by lowering down SOFC operating temperature or improving SOFC performance. This work investigates SOFC by numerical modeling aiming at improving SOFC performance. An SOFC basically consists of a dense electrolyte and two porous electrodes. Therefore, this work is divided into 2 parts focusing on SOFC electrolyte and SOFC electrode, respectively.

In chapter 2 and chapter 3, SOFC based on oxygen ion and proton co-ionic conducting electrolyte is investigated aiming at improving SOFC performance by optimizing SOFC electrolyte. In SOFC with such a co-ionic conducting electrolyte (co-ionic SOFC), both O^{2-} and H^{+} can transport through the electrolyte, and thus causes water generation in both electrodes. For comparison, in traditional SOFC with pure ion conducting electrolyte (SOFC with O^{2-} conducting electrolyte (O-SOFC) and SOFC with H^{+} conducting electrolyte (H-SOFC)), water is generated only in one electrode. The special mass transport phenomenon caused by the co-ionic conducting electrolyte affects SOFC actual performance. However, to what extent and how the cell performance is affected is still unclear. Therefore, in chapter 2, a one-dimensional (1D) hydrogen fed co-ionic SOFC model is developed first, followed by an extended 2D segment model using various fuels. Based on the developed models, the performance of co-ionic SOFC is simulated and analyzed. Results show that, co-ionic SOFC performs better than H-SOFC and O-SOFC. The co-ionic conduction property of

electrolyte can reduce the concentration loss at certain proton transfer number and thus improve SOFC performance. Besides, by comparing the cell performance using different fuels, it is found that syngas mixture is superior to humidified hydrogen when used as fuel in co-ionic SOFC. This work improves our understanding of co-ionic SOFC and provides theoretical guidance for experimental researchers to improve co-ionic SOFC performance. As a further step, in chapter 3, a numerical procedure is developed to construct the dual-phase composite co-ionic conducting electrolyte and predict the electrolyte partial conductivities, which are important property parameters of the co-ionic conducting electrolyte.

In chapter 4 and chapter 5, the relationship between SOFC electrode micro parameters and SOFC cell performance is developed, aiming at improving SOFC performance by optimizing SOFC electrodes. The whole relationship can be divided into 2 parts: the relationship between electrode micro parameters and electrode effective properties (content in Chapter 4) and the relationship between electrode effective properties and cell performance (content in Chapter 5).

The effective TPB length and effective conductivity are two important electrode effective parameters. However, by now, the relationship between electrode micro parameters and the effective TPB length are well investigated while the relationship between electrode micro parameters and the effective conductivity are still lacking. In chapter 4, the composite electrode is numerically constructed using a random particle packing procedure, followed by a particle geometric dilating to simulate the sintering process. The effects of various electrode micro parameters on the electrode effective conductivity are investigated, including material composition, porosity, particle size and contact angle. Results show that, the effective conductivity of electrode solid phase is mainly determined by its total volume fraction in electrode (including the gas phase). Based on the numerical results, the conventional percolation model describing the relationship between electrode micro parameters and electrode effective conductivity is improved.

In chapter 5, a macro SOFC model is developed bridging the electrode effective properties to the cell performance (section 5.1& 5.2). In the model, the electron transport, ion transport and gas transport are coupled with local electrochemical reactions in electrodes. The model can be used for SOFC electrode design and optimization by incorporating with electrode micro-models. As a step towards electrode optimization, the electrochemical active thickness (EAT) in SOFC anode is investigated using the developed multi-scale model (section 5.3). The EAT indicates the key part to be optimized in SOFC electrode. By both numerical and theoretical analysis, an positive relationship between the EAT and the ratio $R_{\mathrm{act,con}}/R_{\mathrm{ohmic}}$ is finally concluded.

LIST OF PUBLICATIONS

1. **Zheng, K.**, Sun, Q., & Ni, M. (2013). Local non-equilibrium thermal effects in solid oxide fuel cells with various fuels. *Energy Technology*, 1(1), 35-41.
2. **Zheng, K.**, Ni, M., Sun, Q., & Shen, L. (2013). Mathematical analysis of SOFC based on co-ionic conducting electrolyte. *Acta Mechanica Sinica*, 29(3), 388-394.
3. **Zheng, K.**, Li, L., & Ni, M. (2014). Investigation of the electrochemical active thickness of solid oxide fuel cell anode. *International Journal of Hydrogen Energy*, 39(24), 12904-12912.
4. **Zheng, K.**, Zhang, Y., Li, L., & Ni, M. (2015). On the tortuosity factor of solid phase in solid oxide fuel cell electrodes. *International Journal of Hydrogen Energy*, 40(1), 665-669.
5. **Zheng, K.**, & Ni, M. (2015). Effective conductivity of solid oxide fuel cell electrodes. *ECS Transactions*, 68(1), 2057-2066.
6. **Zheng, K.**, & Ni, M., (2015). Reconstruction of solid oxide fuel cell electrode microstructure and analysis of its effective conductivity**.** *Science Bulletin*, accepted for publication.
7. Li, L., **Zheng, K.**, Ni, M., Leung, M., & Xuan, J. (2015). Partial modification of flow-through porous electrodes in micro fluidic fuel cell. *Energy*, 88, 563-571.
8. Sun, Q., **Zheng, K.**, & Ni, M. (2014). Thermodynamic analysis of methane-fueled solid oxide fuel cells considering CO electrochemical oxidation. *Chinese Journal of Chemical Engineering*, 22(9), 1033-1037.
9. **Zheng, K.**, Ni, M, & Sun, Q. A detailed comparison of mass transport models

for predicting concentration overpotential of SOFC electrodes. (oral presentation, the 5th International Conference on "Fundamentals & Development of Fuel Cells", in Karlsruhe, Germany, April 16-18, 2013)

ACKNOWLEDGEMENTS

I would like to take this opportunity to thank all the individuals who give their time and support to this work.

Special thanks to my chief supervisor, Dr. NI Meng, for his continuous guidance and encouragement throughout my research work. From him, I learned not only how to conduct a research work, but also the attitude we should have towards science. These are of great importance to my work and life in future. Great thanks are also given to my co-supervisor, professor SHEN Liyin in Chongqing University, for all his constructive comments and kind help.

I would also like to thank all our group members, Miss SUN Qiong, Miss LI Meiling, Dr. HE Wei, Dr. DONG Feifei, Mr. CHEN Bin and Mr. XU Haoran. The interesting discussions with them always inspire me a lot. Special thanks to Miss LI Li in City University of Hong Kong for her great efforts and help to this work. I also thank Dr. Zhang Yanxiang in Harbin Institute of Technology for his valuable advice and information in the electrode construction part.

Great thanks to all those individuals who give their valuable comments and suggestions to improve this work.

Finally, I would like to thank my families and friends. Their deep love and understanding give me the freedom and support to do what I want.

TABLE OF CONTENTS

LIST OF FIGURES

LIST OF TABLES

LIST OF ABBREVIATIONS

a	chemical activity
d	particle radius, m
j	current density, A/m^2
j_0	exchange current density, A/m^2
j_{TPB}	electric current generated in unit TPB length, A/m
j_{ref}	reference exchange current density, A/m
p	partical pressure, pa
p_{atm}	operating pressure, pa
r	particle radius, m
r_{p}	pore radius, m
t_H	proton transfer number
n	electron number involved in reaction
n_{el}	particle number of electron conducting particles
v_{i}	stoichiometric coefficient
x	gas molar fraction
$B_{\mathrm{A/C}}$	anode/channel interface
$B_{\mathrm{C/C}}$	cathode/channel interface
$B_{\mathrm{A/E}}$	anode/electrolyte interface
$B_{\mathrm{C/E}}$	cathode/electrolyte interface
D_{n}	computational domain height, μm
E	reversible open circuit voltage, V
E_{T}	Temperature related open circuit voltage, V
E_{eq}	equilibrium electric potential difference, V

E_{Nernst}	reversible electrode potential, V
F	Faraday constant, 96485 C/mol
G	Gibbs free energy, J
H	enthalpy, J
L	thickness of electrolyte
L_{cube}	cube length, μm
L_{vox}	voxel length, μm
N	molar flux of gas species, mol/(m^2 s)
P_{erco}	percolation probability
R_{ohmic}	ohmic loss, V
R_{act}	activation loss, V
R_{con}	concentration loss, V
$R_{\mathrm{act,con}}$	concentration related activation loss, V
R	ideal gas constant, 8.314 J/(mol K)
T	operating temperature, K
V_{cell}	output voltage, V
$Z_{\mathrm{i,i}}$	coordinate number among the *i*-conducting particles

Greek letters

η_{local}	local overpotential, V
η_{thermal}	Thermodynamic efficiency
η_{act}	activation overpotential, V
η_{ohmic}	ohmic overpotential, V
η_{con}	concentration overpotential, V
ϕ	electric potential, V
σ	ionic effective conductivity in electrolyte, S/m

σ_0	material intrinsic conductivity, S/m
σ_{eff}	effective conductivity, S/m
λ_{TPB}	TPB length in unit volume (m/m^3)
ξ	tortuosity factor for gas diffusion
Ψ	volume fraction

Subscripts:

el	electronic conducting phase
io	ionic conducting phase
inlet	inlet conditions
r	reaction sites
local	local reaction sites
ref	reference conditions
TPB	triple phase boundaries
CO	carbon dioxide
H_2	hydrogen
O_2	oxygen
H_2O	water
y	position y

Superscripts:

a	anode side
c	cathode side

CHAPTER 1 INTRODUCTION

1.1 Fuel cell in brief

The increasing energy demand and environmental crisis are two challenges for the world. It is predicted by the International Energy Agency (IEA) that the world's energy demand and carbon-dioxide emission in 2035 will be about 18 billion tonne oil equivalent (t.o.e) and 36 gigatonnes per year (Gt/yr) respectively [1-2]. In 2009, the values were only 12 billion t.o.e and 29 Gt/yr, respectively. Fuel cell has great potential to solve the energy and environmental crisis. Fuel cell is a kind of electrochemical power generation device that can convert the chemical energy of fuel into electric energy directly through electrochemical reactions [3-5]. Therefore, it is not limited by the Carnot efficiency as internal combustion engine and has a high theoretical efficiency. Besides, when hydrogen is used as fuel, only water is generated as byproduct and thus it is quite environmental friendly. As a clean and efficient power generation device, fuel cell has attracted much attention.

The first fuel cell was invented in 1839. William Grove demonstrated that hydrogen (H_2) and oxygen (O_2) could be produced at two platinum electrodes respectively, by supplying an electric current to the dilute acid solution, i.e. the electrolysis process [5]. The operation of fuel cell is the reverse electrolysis process. By supplying O_2 and H_2 separately to the electrodes, electricity can be produced.

1.1.1 Thermodynamic mechanism of fuel cell

A basic fuel cell consists of 3 key components: a porous anode, a porous cathode and an electrolyte. The electrodes provide sites for half reactions while the electrolyte separates them from each other [3-5]. For a typical fuel cell with H_2 as fuel, the overall reaction is:

$$H_2 + 0.5O_2 \rightarrow H_2O \qquad (1.1)$$

It should be noted that, although H_2 and O_2 are the most commonly used fuel and oxidant in fuel cells, any other substance that can be chemically oxidized (reduced) can be used as the fuel (oxidant) of a fuel cell theoretically [4, 6].

The output energy of a fuel cell directly comes from the fuel chemical energy. The total amount of energy released from a reaction equals to the enthalpy change of the reaction. However, only part of the chemical energy can be converted into electric energy in a fuel cell while the remaining part is released as heat. For a reversible electrochemical reaction, the maximum electric power output is determined by the Gibbs free energy change of the reaction. Therefore, the maximum conversion efficiency of fuel chemical energy to electric energy (i.e. thermodynamic efficiency) in a fuel cell is:

$$\eta_{\text{thermo}} = \frac{\Delta G}{\Delta H} \qquad (1.2)$$

The reversible open circuit voltage (OCV) or electrochemical motive force (EMF) of a fuel cell is:

$$E = \frac{-\Delta G}{nF} \qquad (1.3)$$

where, E is the reversible open circuit voltage (V); G is the Gibbs free energy (J); n is the number of electrons involved in the reaction; F is the Faraday constant (96,485 C/mol).

Since ΔG of a chemical reaction changes with temperature, pressure and reactant /product concentration. The Nernst equation is derived to include these effects on E:

$$E_{\text{Nernst}} = E_{\text{T}} - \frac{RT}{2F} \ln \left(\frac{\prod a_{\text{products}}^{\text{vi}}}{\prod a_{\text{reactants}}^{\text{vi}}} \right) \tag{1.4}$$

Where, a represents the activity and v_{i} is the stoichiometric coefficient.

For a typical H_2 fed solid oxide fuel cell, E_{Nernst} can be written as [7-9]:

$$E_{\text{Nernst}} = E_{\text{T}} - \frac{RT}{2F} \ln \left(\frac{p_{\text{H2O,TPB}}}{p_{\text{H2,TPB}}\, p_{\text{O2,TPB}}^{0.5}} \right) \tag{1.5}$$

$$E_{\text{T}} = 1.253 - 0.00024516T \tag{1.6}$$

1.1.2 Cell performance

In actual operation, the cell output voltage is usually lower than E_{Nernst} due to various losses. Major losses affecting the cell actual performance include:

1) Activation loss:

The activation loss is caused by the local activation reaction barriers for electrochemical reactions. The activation loss and local current density are linked by the Butler-Volmer (B-V) equation as [10-11]:

$$\eta_{act,i} = \frac{RT}{F} \ln \left(\frac{j}{2 j_{0,i}} + \sqrt{\left(\frac{j}{2 j_{0,i}} \right)^2 + 1} \right) \qquad i = a \text{ or } c \tag{1.7}$$

where, j_{o} is the exchange current density (A/m^2), which represents the electrochemical activity of the electrode. j_{o} is a very important parameter in fuel cell modeling and its value depends on temperature, materials properties and microstructure of the electrodes, and the composition of the reactants/products.

2) Ohmic loss:

The ohmic loss is caused by the electron and ion transport in fuel cell. Traditionally, the major part of ohmic loss is attributed to the ion transport in the electrolyte, which can be determined by the Ohm's law as:

$$\eta_{ohmic} = j\frac{L}{\sigma} \tag{1.8}$$

where, L is the thickness of the electrolyte (m), j is the current density (A/m^2), σ is the ionic conductivity (S/m).

3) Concentration loss:

In the Nernst equation for calculating the equilibrium potential, the activities of the reactants and products at the electrode surface are used. In reality, the activities of the reactants/products at the reaction sites can differ significantly from those at the electrode surface due to the transport resistance. Thus, the Nernst potential needs to be corrected by the transport process. The potential difference for potential correction is the concentration overpotential, and it can be calculated as:

$$\eta_{con} = \frac{RT}{2F}\ln\left(\frac{\prod a_{\mathrm{products}}^{\mathrm{vi}}}{\prod a_{\mathrm{reactants}}^{\mathrm{vi}}}\right)_{\text{reference condition}} - \frac{RT}{2F}\ln\left(\frac{\prod a_{\mathrm{products}}^{\mathrm{vi}}}{\prod a_{\mathrm{reactants}}^{\mathrm{vi}}}\right)_{\text{actual condition}} \tag{1.9}$$

The actual output voltage of a fuel cell can be obtained by subtracting all the above-mentioned losses from the E_{Nernst}, as shown in Eq. (10). Figure 1.1 shows a schematic diagram of the I-V curve of a typical fuel cell. In ideal situation without any overpotential loss, the output voltage U should be a constant with varying current density j. However, in actual situation, the output voltage U decreases with increasing j as the 3 losses all increase with increasing j. Moreover, as j increases, the dominant loss changes from the activation loss to the ohmic loss and finally the concentration loss. The cell performance degrades significantly under large current densities due to insufficient mass transport, which should be avoided for fuel cell in operation [12].

$$U = E_{Nernst} - \eta_{act}^{a} - \eta_{act}^{c} - \eta_{ohmic} - \eta_{con}^{a} - \eta_{con}^{c} \tag{1.10}$$

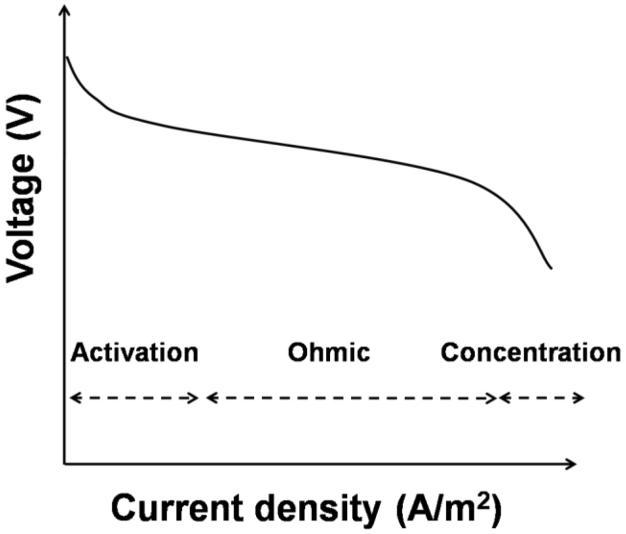

Figure 1.1 Schematic diagram of typical I-V curve of fuel cell

1.2 Solid oxide fuel cell

1.2.1 Benefits of SOFC

SOFC is a kind of fuel cell characterized by its solid electrolyte and high operating temperature. Traditionally, oxygen ion conducting materials (e.g. YSZ) are used as the electrolyte. SOFC is more attractive than other low temperature fuel cells because [13-16]: 1) High temperature (commonly 1073 K~1273 K) improves the electrochemical reaction rates, ion/electron conductions and gas transport, thus decreases the losses affecting SOFC actual performance. 2) The high electrochemical reaction rates at high operating temperatures allow the use of non-expensive metal catalysts and therefore reduce the cell cost. 3) The high operating temperature allows the direct internal reforming of hydrocarbon fuels and cracking of ammonia. Therefore, not only hydrogen, but also hydrocarbon fuels (such as methane, methanol etc.) and ammonia can be directly used in SOFC. This separates SOFC from the hydrogen economy and makes it possible to be used in very near future. It should be noted that, carbon monoxide (CO) is generated in nearly all the fuel reforming process. CO is a poison to low temperature fuel cells and a low concentration of only tens of ppm can kill the catalyst. For comparison, CO does not poison the catalyst of SOFC, instead, it can be used as fuel for power generation. 4) The high quality waste heat can be more effectively recovered by combining SOFC with other industry systems (such as heat recovery system or combined heat and power system: CHP) with greatly enhanced system efficiency. For example, the power generation efficiency of fuel cell is about 45%~65%, while the efficiency of a SOFC-based CHP system can reach 85% [15-17]. 5) The whole solid structure makes the cell to be highly reliable, long life and quiet.

1.2.2 Working mechanism of SOFC

An SOFC basically consists of three components: the porous anode and the porous cathode provide transport paths (for ions, electrons and gases) and reaction sites for the electrochemical reactions, while the dense electrolyte functions as an ion transport medium between the electrodes and separates the fuel gas and the oxidant gas in the two electrodes. Figure 1.2 shows the basic working mechanism of an SOFC with oxygen-ion (O^{2-}) conducting electrolyte. Hydrogen (H_2) and air are supplied from the inlets of gas channels in the anode and cathode, respectively. In operation, H_2 will transport from anode gas channel to anode reaction sites while oxygen (O_2) will transport from cathode gas channel to cathode reaction sites. Oxygen is separated into 2 oxygen ions (O^{2-}) at the cathode reaction sites (as shown in Eq. (11)). The generated O^{2-} will transport from the cathode reaction sites to the anode reaction sites through the electrolyte.

After that, the O^{2-} will react with H_2 to generate water steam (H_2O) and release electrons (e^-) at the anode reaction sites (as shown in Eq. (12)). The generated H_2O will transport from anode reaction sites to anode gas channel, and the released e^- will transport from anode reaction sites to cathode reaction sites through external electric circuit to form a complete circuit cycle. It should be noted that, the reaction sites refer to the triple phase boundaries (TPBs) where the gas phase, the ion conducting phase and electron conducting phase meet, as labeled in Figure 1.2.

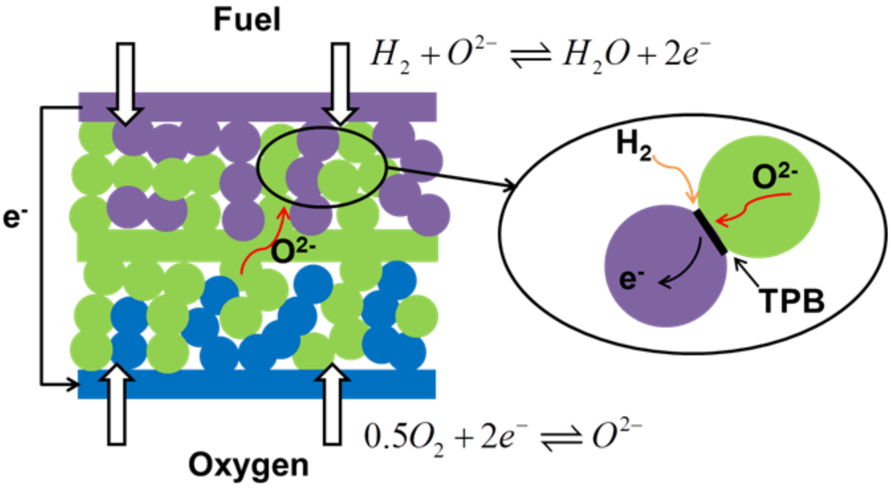

Figure 1.2 Working mechanism of SOFC with oxygen-ion conducting electrolyte

The electrochemical reactions involved in cathode and anode are:

Cathode:

$$0.5O_2 + 2e^- \rightarrow O^{2-} \tag{1.11}$$

Anode:

$$H_2 + O^{2-} \rightarrow H_2O + 2e^- \tag{1.12}$$

The whole reaction in the cell can be written as:

$$H_2 + 0.5O_2 \rightarrow H_2O \tag{1.13}$$

1.2.3 Status of SOFC

By now, a major limitation for SOFC commercialization is its high cost [15-16]. On the one hand, the high cost can be reduced by improving the cell performance and thus lowers down the cost per unit energy. On the other hand, the high cost can be reduced by lowering down SOFC operating temperature so that cheaper materials can be used as SOFC components. However, it should be noted that, as the operating temperature decreases, the cell performance also degrades, mainly due to the reduced catalyst activity and electrolyte conductivity. The degraded cell performance partly negates the cost benefit. Therefore, it can be concluded that improving SOFC performance is of great importance.

An SOFC basically consists of a dense electrolyte and two porous electrodes. Therefore, research efforts aim to improve SOFC single cell performance can be classified as: 1) Developments of new electrolyte materials with high ionic conductivities [18-19] and new methods to fabricate thin electrolytes [20-22] to reduce the ohmic loss in the electrolyte. 2) Developments of new catalysts with high electrode activity [23-24] and electrode design and optimization [25-26] to reduce the losses in electrode.

Nowadays, the electrolyte thickness is reduced to less than 10 μm [20, 27]. Further decrease of electrolyte thickness will be very difficult. Therefore, more and more research efforts on SOFC electrolyte focusing on the development of new electrolyte materials. Proton-conducting materials (such as $BaCeSmO_3$) are promising SOFC electrolyte candidates for their high conductivities. Comparing with traditional oxygen-ion conducting electrolyte based SOFC (O-SOFC), proton-conducting electrolyte based SOFC (H-SOFC) has a higher theoretical efficiency [28] because water steam is generated in the cathode and therefore complete fuel utilization can be achieved [29-30]. However, it's also reported that most proton conducting oxides show both oxygen ion and proton conductivity, which are called as the "co-ionic" conducting oxides [31-32]. As it is expected that SOFC with such a co-ionic conducting electrolyte might further lower down the electrode loss [33], it is of theoretical and practical interest to conduct more research in this field (**chapter 2 and chapter 3**). Literature review on SOFC with co-ionic conducting electrolyte is shown in **section 1.2.3.1**.

In addition to electrolyte, it is more promising to further improve the SOFC performance by improving SOFC electrodes. Zhao et al. [27] tested the ohmic contribution in SOFC using current interruption technique and reported that at 1073 K, the area specific ohmic resistance (ASR) of the 8 μm electrolyte only contributed about 19% of the total ohmic ASR. For comparison, Andersson et al. [9] developed a 3D numerical model of SOFC and found that at 1010 K, only 10% of the total voltage loss occurred in electrolyte, while the remaining 30% was in cathode and 60% was in anode for SOFC with 10 μm YSZ electrolyte. All of the results validate that the ohmic loss in SOFC electrolyte is already significantly reduced by thin electrolyte thickness, and the major part of loss affecting SOFC actual performance occur in electrodes.

SOFC electrode performance is mainly determined by three kinds of losses: the activation losses related to local electrochemical reaction rates, the ohmic losses related to ion and electron conductions and the concentration losses due to concentration differences between local reaction sites and reference conditions. In addition to material developments with high conductivities and electrochemical activities, SOFC electrode performance can be also improved by optimizing electrode micro parameters, such as composition, porosity and particle size etc. A typical example in this field is the development of functionally graded electrode (FGE), which refers to electrode with composition or microstructure (particle size, porosity) varying along the electrode thickness [14, 34-35]. Experimental results show that FGE can dramatically increase the TPB length [36], lower down the interfacial resistance [37-39] and therefore enhance the cell performance. However, the underlying mechanism from FGE modeling works [40-44] is still unclear which requires a better understanding of the relationship between SOFC electrode micro parameters and SOFC cell performance (**chapter 4 and chapter 5**). Literature review on the relationship is shown in **section 1.2.3.2**.

Besides, the design of FGE depends on a good knowledge of electrode local functions in local sites, so that the local electrode structure can be purposely design to play its role. Nowadays, a common practice is to fabricate SOFC electrode as two different layers with different micro-parameters [45], which is a kind of FGE in nature and is easier to be realized than other continuous or multi-layer graded electrodes. In such an electrode, the inter layer (the layer near the electrolyte) functions as the reaction layer and provides most of the reaction sites while the outer layer (the layer near the gas channel) functions as the support layer and provides mechanical support and transport paths for reaction gases and electrons. To develop such a structured electrode with good performance, one primary parameter is the interlayer thickness. In ideal situation, the interlayer thickness should be the electrode thickness with the best SOFC performance (the optimal thickness). However, from literature review, it is found that the optimal thickness is still to be determined (**chapter 5**). The thicknesses obtained from literatures varied in a wide range, even for electrodes with the same materials and/or same structure parameters, as shown in **section 1.2.3.3**.

1.2.3.1 Review of SOFC based on co-ionic conducting electrolyte

Extensive studies have been conducted on the charge transfer properties of the co-ionic conducting oxides [31, 46-49], however, limited works considered the performance behavior of SOFC based on co-ionic conducting electrolyte (co-ionic SOFC). Iwahara et al. [33] synthesized the $BaCe_{1-x}Sm_xO_{3-a}$ ceramics oxides and found that $BaCe_{1-x}Sm_xO_{3-a}$ showed oxygen ion and proton co-conduction property in fuel cell conditions. As the operating temperature increased from 973 K to 1273 K, the dominant conduction in $BaCe_{1-x}Sm_xO_{3-a}$ oxides changed from proton conduction to oxygen ion conduction. They also constructed the hydrogen-air fuel cell using $BaCe_{1-x}Sm_xO_{3-a}$ electrolytes (x= 0.05, 0.10, 0.15) and found that the cell based on $BaCe_{0.9}Sm_{0.1}O_{3-a}$ electrolyte exhibited the best performance. Demin et al. [50] investigated the co-ionic SOFC performance by numerical analysis. They reported that the partial current caused by proton conduction (j_H) and the partial current caused by oxygen ion conduction (j_O) were not proportional to their transfer numbers (t) in the co-ionic conducting electrolyte. The transfer number t is commonly used to characterize the charge transfer properties in co-ionic conducting oxides, and it is defined as the ratio of the partial conductivity of a charge carrier (oxygen ion or proton) to the oxide total conductivity. It should be mentioned that the transfer numbers in a co-ionic conducting oxide are difficult to be exactly determined due to the complex electrochemical process involved [46, 48-49]. Huang et al. [51] developed a mathematical model to describe the fuel cell based on mixed conducting ceria-based composites (CBCs) electrolyte (including the conduction of oxygen ion, proton and electron). The effects of different gas partial pressures on cell performance were investigated. It was found that, the anode steam partial pressure and hydrogen partial pressure significantly affected the OCV, cell efficiency and power density. In comparison, the cathode steam partial pressure only had slight influence on fuel cell performance. It was also stated that, SOFC with CBCs electrolyte showed superior performance than SOFC with pure SDC electrolyte, indicating the promising prospect of CBCs electrolyte in low temperature SOFC. Bavarian et al. [52] built a mathematical model of co-ionic SOFC using the $BaCe_{0.9}Sm_{0.1}O_{3-a}$ electrolyte and conducted the cell steady-state analysis under three different operating modes. It was found that, under constant ohmic load and constant voltage operation modes, three stable states existed while only one stable state existed under constant current mode. Bavarian et al. [53] also developed a control system for a heat integrated co-ionic SOFC system. With the control system, the solid temperature and the cell voltage could be controlled.

Above-mentioned studies provide valuable information on co-ionic SOFC, however, most of the work only considered the theoretical performance of co-ionic SOFC and neglected the various losses affecting SOFC actual performance. For design and optimization of co-ionic SOFC, a fundamental understanding on the transport and reaction processes is essential but is lacking in the current literature.

1.2.3.2 Review of electrode effective conductivity

The effective TPB length and effective conductivity are two important electrode effective parameters. However, by now, the relationship between electrode micro parameters and the effective TPB length are well investigated [54-61] while the relationship between electrode micro parameters and the effective conductivity (σ_{eff}) are still lacking.

Great efforts have been devoted to linking the σ_{eff} with electrode microstructure parameters [59, 61-75]. Previous numerical studies in this field can be mainly classified into 3 kinds: (1) Numerical modeling based on the reconstructed actual electrodes using experimental methods, such as the focused ion beam scanning electron microscope technique [59, 61-63]; (2) Numerical modeling based on the constructed electrodes using numerical methods (for example, the random particle packing procedure [64-65]; (3) Analytical works based on the percolation theory [66-72]. The research approach based on experimental techniques provides a microstructure characterization of the actual electrode, however, it doesn't have any predictive ability and may be more suitable to be used to adjust and verify the developed relationship between electrode micro parameters and electrode effective properties. In addition, this approach relies on both of the experimental technique and image processing technique, which may also cause some uncertainty [70, 75]. In comparison, the particle packing electrode construction method only presents a simplified electrode structure [70], however, it is comparable easy to be accomplished [72] and thus more suitable to conduct detailed parametric analysis between σ_{eff} and its affecting factors. Furthermore, the particle packing procedure can simulate the actual electrode fabrication process and thus makes it possible to investigate the fabrication parameter (for example, the sintering process) effect on σ_{eff} [55, 72, 76]. The percolation model can be regarded as an extended theory of the particle packing electrode construction method, and it mainly includes two parts: the relationship between electrode micro parameters and the coordinate numbers and the relationship between coordinate numbers and electrode effective properties [66, 70, 72]. Although percolation model cannot show a specific electrode microstructure and can only reflect an averaged situation of an SOFC electrode, it is easy to be incorporated into a high level model to establish a complete relationship between electrode micro parameter and SOFC cell performance [72].

However, present information is still not enough to build a clear and reliable relationship between σ_{eff} and its affecting factors. Most of works in literatures were based on certain electrode structures and investigated the effect of electrode porosity and composition on σ_{eff}, while rare study considered the effect of the electrode particle size and the contact angle among electrode particles (mainly related to the sintering process). Besides, although the percolation models describes the relationship between the electrode micro parameters and coordinate numbers were well developed by [9-10] and then improved by [66, 70-71], the effects of porosity and contact angle on the average coordinate number (Z_{ave}) still need more investigation. Bertei et al. [72] studied the sintering effect on Z_{ave} in random packing structures. However, the porosity effect is examined by adding additional pore-former particles into the rigid particle packing structures (8^{o} contact angle among particles) and the minimum porosity considered is 0.41 (without pore-former). In addition, the electrode porosity decrease from 0.404 to 0.329 as the contact angle increases from 30^{o} to 46^{o} in their study, and thus it is not reasonable to conclude that large contact angle leads to large Z_{ave}, which also might be caused by the low porosity. Furthermore, the commonly used percolation model describes the relationship between the coordinate number and

σ_{eff} is still unconvinced (as shown in Eq. (4.1) [66] & Eq. (4.2) [71]). While other parameters involved in the relationship possess clear physical meanings and are easy to be accessed, the Bruggeman factor μ is experimentally assumed as 1.5, which is doubted to be too small to overestimate the σ_{eff} [77].

$$\sigma_{eff,i} = \sigma_{0,i}\left[(1-\varepsilon)\psi_i P_{erco,i}\right]^{\mu} \quad i = el \ \ or \ \ io \tag{4.1}$$

$$P_{erco,i} = 1 - \left(\frac{4.236 - Z_{i,i}}{2.472}\right)^{3.7} \quad i = el \ \ or \ \ io \tag{4.2}$$

where, σ_{eff} and σ_0 refer to the effective conductivity and material intrinsic conductivity of the *i*-conducting phase, (S/m); ε is the electrode porosity; Ψ is the volume fraction of the *i*-conducting phase; P_{erco} is the percolation probability; $Z_{\text{i,i}}$ is the coordinate number among the *i*-conducting particles.

Consequently, a more comprehensive study is still necessary to build the relationship between electrode micro parameters and electrode effective conductivity.

1.2.3.3 Review of electrode optimal thickness

Optimal thickness in SOFC anode:

Fukunaga et al. [78] studied the optimal thickness by fabricating electrodes with different anode thickness. It was found that for Ni-SDC (Ni-Sm-Doped Ceria) anode, the optimal thickness should be about 110 µm. The large optimal thickness was attributed to the high sintering temperature. Menzler et al. [79] reported that SOFCs with anodes of 1-13 µm thickness showed slightly better performance than those with thicker anodes. Suzue et al. [80] modeled SOFC anode with stochastic reconstruction technique and evaluated the cell performance with lattice boltzmann method (LBM). Results showed that the optimal thickness should no more than 5 μm and 15 μm under 873K and 1073K, respectively. Shikazono et al. [60] reconstructed the 3D anode microstructure using focused ion beam scanning electron microscope (FIB-SEM) technique and conducted performance analysis which indicated that the optimal thickness in anode should be around 1~15 μm. Primdahl et al. [81] tested the optimal thickness of Ni/YSZ anode by impedance spectroscopy and reported an optimal thickness less than 20 μm at 1273 K. Xia et al. [82] established a 1D micro model of SOFC anode in which an optimal thickness of about 50 μm was reported for Ni/SDC anode at 1073 K. Chan et al. [83] reported an optimal thickness of 160 μm. They also indicated that the bigger the particle radius, the higher the optimal thickness. Abudula et al. [84] investigated the optimal anode thickness by experiments: the optimal thickness was 120 μm for pure H_2 and 70 μm for 4.6% of CH_4 under 1273 K. Sunde [56] reported an optimal thickness of 30-40 μm for Pt/EDB (Erbia-Doped Bismuth oxide) electrode. Tanner et al. [85] presented an optimal thickness of about 100 μm. Kawada et al. [86] analyzed SOFC polarization behaviors with an equivalent circuit model and presented an optimal thickness of about 50 μm under 1273 K (when resistance of grain boundaries are not considered). Koyama et al. [87] regarded the optimal thickness of porous SSC ($Sm_{0.5}Sr_{0.5}CoO_3$) electrode as 15 μm. Brown et al. [88] reported that the optimal thickness of Ni/YSZ anode should be around 10 μm when anode size was between 0.5~1 μm under 1273 K. Hussain et al. [45] reported an optimal anode thickness of about 20 μm at 5000 A/m^2 and 1273 K. It was also noted that the optimal thickness might be reduced with a decreased volume fraction of ionic conducting phase.

Optimal thickness in SOFC cathode:

Deseure et al. [41] conducted a micro-modeling of SOFC with functionally graded cathodes and reported that the optimal thickness of cathode should be nearly 15 μm. Lu et al. [89] reported an optimal thickness of LSCF cathode of 13 μm. They found that the cell performance remained constant when cathode thickness was further increased. Chan et al. [90] developed a micro-model of SOFC cathode and reported that the optimal thickness for YSZ/LSM cathode should be 170 μm and 40 μm for particle size of 1 μm and 0.1 μm respectively indicating the significant effect of particle size on optimal electrode thickness. Costamagna et al. [91] reported an optimal thickness of YSZ/LSM cathode of about 15 μm at 1073 K and an optimal thickness of YSZ/Ni anode of about 160 μm at 1273 K. Chen et al. [92] conducted a multi-scale modeling and concluded that the optimal thickness for SOFC cathode should be between 10-20 μm for all microstructures and material choices. Kenjo et al. [93] studied the EDB/Pt cathode and reported that the larger the composition ratio of EDB/Pt, the larger the optimal thickness. But, if the composition ratio of EDB/Pt was less than 0.2 wt%, no thickness effect could be found. When the composition ratio of EDB/Pt equaled to 0.3, the optimal thickness was about 50 μm at 1173 K. Zhao et al. [27] showed an optimal thickness of cathode of about 20 μm at 1073 K. Jiang et al. [94] examined the effect of electrode microstructure, material properties and operating conditions on the optimal thickness. Their simulation result showed that for LSM/YSZ electrode at 1073 K, the optimal thickness increased from 59 μm to 253 μm when the volume fraction of YSZ was changed from 0.295 to 0.705. However, it should be noted that, in their study, the gas concentration effect is neglected.

From above literature review, we can conclude that the electrode optimal thickness is still to be investigated. The values reported in literatures varied in a wide range. A better understanding of the results is required.

1.3 Study objectives and main contents

This work investigates SOFC by numerical modeling aiming at improving SOFC performance. Compared with experimental approach, numerical modeling provides a more efficient and economic way to establish the relationship between the SOFC electrode micro-parameters and cell performance, to conduct SOFC performance analysis and in particular to understand the complex physical/electrochemical process for SOFC in operation. An SOFC basically consists of a dense electrolyte and two porous electrodes. Therefore, this work can be divided into 2 parts focusing on different components of a fuel cell:

Part 1: the co-ionic conducting electrolyte is investigated. In chapter 2, a one-dimensional (1D) model of SOFC with co-ionic conducting electrolyte is developed first, followed by an extended 2D segment model using various fuels. The effect of the co-ionic conducting electrolyte on SOFC cell performance is analyzed. In chapter 3, a numerical procedure is developed to numerically construct the dual-phase composite co-ionic electrolyte and predict the electrolyte partial conductivities.

Part 2: the composite electrode is numerically constructed and the relationship between electrode micro parameters and SOFC cell performance is built. The whole relationship is divided into 2 parts: The relationship between electrode micro parameters and electrode effective properties is studied in chapter 4 and the relationship between electrode effective properties and cell performance is studied in chapter 5.

CHAPTER 2 PERFORMANCE SIMULATION OF SOFC BASED ON CO-IONIC CONDUCTING ELECTROLYTE

In chapter 2 and chapter 3, SOFC based on co-ionic conducting electrolyte is investigated aiming at improving SOFC performance by optimizing SOFC electrolyte. In SOFC with such a co-ionic conducting electrolyte (co-ionic SOFC), both oxygen ion (O^{2-}) and proton (H^{+}) can transport through the electrolyte, which causes water generation in anode and cathode at the same time [33]. For comparison, in traditional SOFC with pure ion conducting electrolyte (SOFC with O^{2-} conducting electrolyte (O-SOFC) and SOFC with H^{+} conducting electrolyte (H-SOFC)), water is generated only in one electrode. The special mass transport phenomenon caused by the co-ionic conducting electrolyte affects SOFC actual performance. However, to what extent and how the cell performance is affected is still unclear. Therefore, in this chapter, numerical models of co-ionic SOFC are developed for performance simulation, with a focus on the investigation of the particular mass transport effect on cell performance [95].

2.1 Introduction to co-ionic SOFC

A schematic diagram of the working mechanism of co-ionic SOFC is shown in Figure 2.1. Hydrogen fuel and air are fed to the anode and cathode, respectively. In operation, reactant gases (hydrogen and air) transport from the gas channels to the triple-phase boundaries (TPBs) – the reaction sites in the porous electrodes. Then, 4 types of half-reactions occur in the reaction sites of anode and cathode (Eq. (2.1)-Eq. (2.4)):

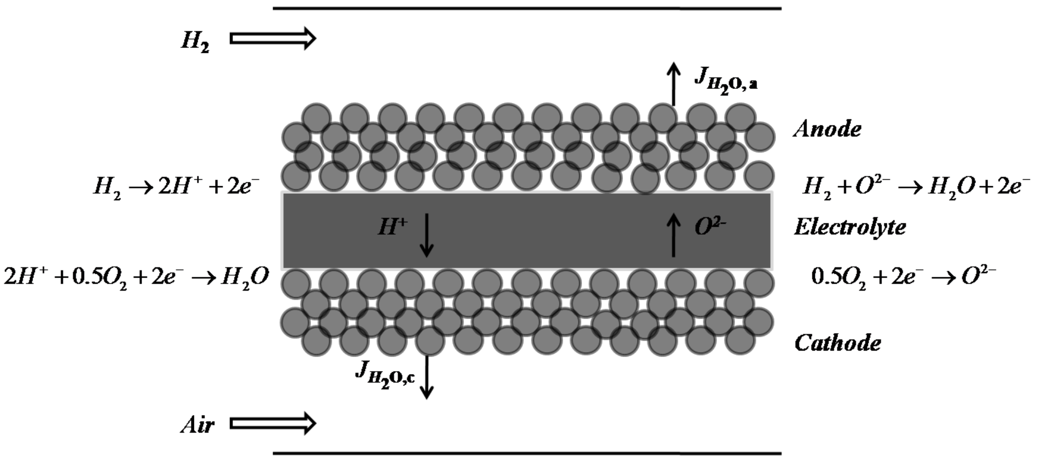

Figure 2.1 Working mechanism of H_2 fed co-ionic SOFC

Anode:

$$H_2 \rightarrow 2H^+ + 2e^- \tag{2.1}$$

$$H_2 + O^{2-} \rightarrow H_2O + 2e^- \tag{2.2}$$

Cathode:

$$2H^+ + 0.5O_2 + 2e^- \rightarrow H_2O \tag{2.3}$$

$$0.5O_2 + 2e^- \rightarrow O^{2-} \tag{2.4}$$

Subsequently, in the anode, the generated protons (Eq. (2.1)) transport from the reaction sites to the cathode through the co-ionic electrolyte, and the generated water (Eq. (2.2)) transport from the reaction sites to the anode gas channel. In the cathode, the generated oxygen ions (Eq. (2.4)) transport from the reaction sites to the anode through the co-ionic electrolyte, and the generated water (Eq. (2.3)) transport from the reaction sites to the cathode gas channel. The generated electrons (Eq. (2.1) & Eq. (2.2)) in anode are collected by the current collector and then transport to the cathode through external circuit to participate in reactions (Eq. (2.3) & Eq. (2.4)) in cathode.

It can be seen from the working mechanism of co-ionic SOFC that water steam is generated in both anode and cathode. This special phenomenon affects co-ionic SOFC actual performance. However, most current studies in this field are experimental investigations focusing on the development of novel electrolyte materials [33, 96-97]. For comparison, mathematical modeling provides a more efficient and economic way to understand the complex physical/electrochemical process for SOFC in operation [98]. Although some preliminary modeling works can be found in literature [50-52], the actual performance of co-ionic SOFC has been rarely studied numerically. Therefore, in this chapter, numerical models are developed to investigate the co-ionic SOFC, with a focus on the effect of the particular mass transport on SOFC performance.

2.2 One-dimensional (1D) model of co-ionic SOFC fed with H2

In this section, a one-dimensional (1D) model considering various kinds of losses is developed to simulate the co-ionic SOFC actual performance. For simplicity, it is assumed that electrochemical reactions only occur at the electrode/electrolyte (E/E) interfaces and only parameter variations in the electrode thickness direction are considered. Therefore, given various losses, the cell output voltage (*U*) can be obtained as:

$$V_{cell} = E_{Nernst} - \eta_{act}^{a} - \eta_{act}^{c} - \eta_{ohm} \tag{2.5}$$

where, *E* refers to the Nernst voltage under certain operating conditions; η_{act}^{a} and η_{act}^{c} refer to the activation loss in anode and cathode, respectively; η_{ohmic} refer to the ohmic loss in electrolyte.

2.2.1 Nernst voltage

Considering that electrochemical reactions only occur at the E/E interfaces, the electromotive forces caused by H^{+} and O^{2-} conduction can be described by the

Nernst equation as [52]:

$$E_H = E_T - \frac{RT}{2F}\ln\left(\frac{P^c_{H2O,r}}{P_{H2,r}P^{0.5}_{O2,r}}\right) \tag{2.6}$$

$$E_O = E_T - \frac{RT}{2F}\ln\left(\frac{P^a_{H2O,r}}{P_{H2,r}P^{0.5}_{O2,r}}\right) \tag{2.7}$$

$$E_T = 1.253 - 0.00024516T \tag{2.8}$$

Where, T, R and F refer to operating temperature (K), ideal gas constant (8.314 J/(mol K)) and Faraday constant (96485 C/mol); subscript r represents reaction sites; superscripts a and c represent the anode and the cathode, respectively. It can be found that the concentration losses caused by gas transport are already implicitly included in Eq. (2.6) and Eq. (2.7), because the gas partial pressures (P) at the reaction sites are used.

2.2.2 Activation loss

The activation loss in SOFC electrodes can be calculated by the Butler-Volmer equation as (assume the symmetric factors are 0.5) [10]:

$$\eta_{act,i} = \frac{RT}{F}\ln\left(\frac{j}{2j_{0,i}} + \sqrt{\left(\frac{j}{2j_{0,i}}\right)^2 + 1}\right) \qquad i = a \; or \; c \tag{2.9}$$

where, j_0 is the exchange current density (A/m^2); j is the operating current density (A/m^2).

2.2.3 Ohmic loss

Since it is assumed that all the electrochemical reactions occur in the E/E interface, the ohmic losses related to ion conduction in electrodes are ignored. In addition, the ohmic losses caused by electron conduction in electrodes can be also neglected, because the electron conductivity is several orders of magnitude higher than the ion conductivity [27]. Therefore, in present model, only the ohmic loss related to H^+ and O^{2-} conduction in the co-ionic electrolyte is considered. According to the Ohm's law, the ohmic loss (η_{ohmic}) can be calculated as:

$$\eta_{ohmic} = j\frac{L}{\sigma} \tag{2.10}$$

where, L and σ are the thickness (m) and total conductivity (S/m) of the electrolyte, respectively.

2.2.4 Concentration loss

Different gas distributions in SOFC electrodes mainly affect SOFC cell performance by affecting the concentration losses in anode and cathode (η_{con}^{a} and η_{con}^{c}). Although the gas distribution effects are already incorporated in the calculation of E (Eq. (2.6) and Eq. (2.7)), they are calculated separately to show how the particular mass transport in co-ionic SOFC electrodes affects the cell performance:

$$\eta_{conc,a} = \frac{RT}{2F}\ln\left(\frac{P_{H2O,r}^{a}P_{H2}}{P_{H2O}^{a}P_{H2,r}}\right) \tag{2.11}$$

$$\eta_{conc,c} = \frac{RT}{2F}\ln\left(\frac{P_{H2O,r}^{c}P_{O2}^{0.5}}{P_{H2O}^{c}P_{O2,r}^{0.5}}\right) \tag{2.12}$$

2.2.5 Mass transport

As the gas partial pressures (P) at the electrode/channel (E/C) interfaces are input parameters in present model, their values at the reaction sites of electrodes can be obtained based on the dusty gas model (DGM) as [99-100]:

$$\frac{N_i}{D_{i,k}^{eff}} + \sum_{j=1, j\neq i}^{n} \frac{y_j N_i - y_i N_j}{D_{ij}^{eff}} = -\frac{P}{RT}\frac{dy_i}{dz} \tag{2.13}$$

where, N is the molar flux (mol/(m^{2}s)); y_i is the molar fraction; $D_{i,j}^{eff}$ and $D_{i,k}^{eff}$ are the effective binary diffusion coefficient and the effective Knudsen diffusion coefficient, respectively.

The effective diffusion coefficients can be obtained from the diffusion coefficients by multiplying a ratio of the electrode porosity (ε) to the tortuosity factor of gas phase (ξ) [11], as shown in Eq. (2.14) and Eq. (2.15).

$$D_{i,j}^{eff} = \frac{\varepsilon}{\xi} D_{i,j} \tag{2.14}$$

$$D_{i,k}^{eff} = \frac{\varepsilon}{\xi} D_{i,k} \tag{2.15}$$

The binary diffusion coefficient between two gas species (cm^2/s) can be calculated by the Fuller's method as [101-102]:

$$D_{i,j} = \frac{0.00143 T^{1.75}}{p M_{ij}^{1/2} \left[V_i^{1/3} + V_j^{1/3} \right]^2} \tag{2.16}$$

$$M_{ij} = 2\left[(1/M_i) + (1/M_j) \right]^{-1} \tag{2.17}$$

where, T and p are the temperature (K) and pressure (bar); M is the molecular mass (g/mol); V is the diffusion volume (for H_2, O_2, N_2, H_2O, the values are 6.12, 16.3, 18.5, 13.1). It should be mentioned that, among various calculation methods, the binary diffusion coefficient calculated by Fuller's method leads to the largest value [101]. For reference, under 1073 K, the calculated binary diffusion coefficient between H_2 and H_2O is 8.65×10^{-4} m^2/s.

The Knudsen diffusion coefficient (m^2/s) can be calculated using the kinetic theory as [11, 103]:

$$D_{i,k} = 97 r_p \sqrt{\frac{T}{M_i}} \tag{2.18}$$

where, r_p is the average pore radius (m); M is the molecular mass (g/mol). Under 1023 K and with an average pore radius of 2.6 μm, the calculated Knudsen diffusion coefficient is 5.7×10^{-3} m^2/s, quite similar to the value (5.68×10^{-3} m^2/s) reported in literature [104].

When H_2 is used as fuel, no chemical reactions occur inside anode. At steady state, the mass transport rates of water steam in anode (N^a_{H2O}) and cathode (N^c_{H2O}) are determined separately using current densities j_H and j_O, while the mass transport rates of hydrogen in anode (N_{H2}) and oxygen in cathode (N_{O2}) are co-determined by j_H and j_O, that is,

$$N_{H2} = \frac{j_O + j_H}{2F} \tag{2.19}$$

$$N_{O2} = \frac{j_O + j_H}{4F} \tag{2.20}$$

$$N^a_{H2O} = -\frac{j_O}{2F} \tag{2.21}$$

$$N^c_{H2O} = -\frac{j_O}{2F} \tag{2.22}$$

2.3 Calculation procedure and model validation

A flow diagram of the calculation procedure is shown in Figure 2.2. For a given output voltage U, the corresponding current densities j_H and j_O are computed. The procedure begins with assuming the values of j_H and j_O, based on which the partial pressures ($P^c_{H2O,r}, P^a_{H2O,r}, P_{H2,r}, P_{O2,r}$) at reaction sites can be calculated using Eq. (2.13). Then, E_H and E_O can be determined using Eq. (2.6) and Eq. (2.7). Activation losses ($\eta_{H,act,a}$, $\eta_{H,act,c}$, $\eta_{O,act,a}$, $\eta_{O,act,c}$) and ohmic losses ($\eta_{H,ohmic}$, $\eta_{O,ohmic}$) related to O^{2-} conduction and H^+ conduction can be calculated directly with the assumed j_O and j_H separately. Finally, the calculated output voltages U_H' and U_O' using Eq. (2.5) are compared with the given U to judge the calculation loop to be continue or not.

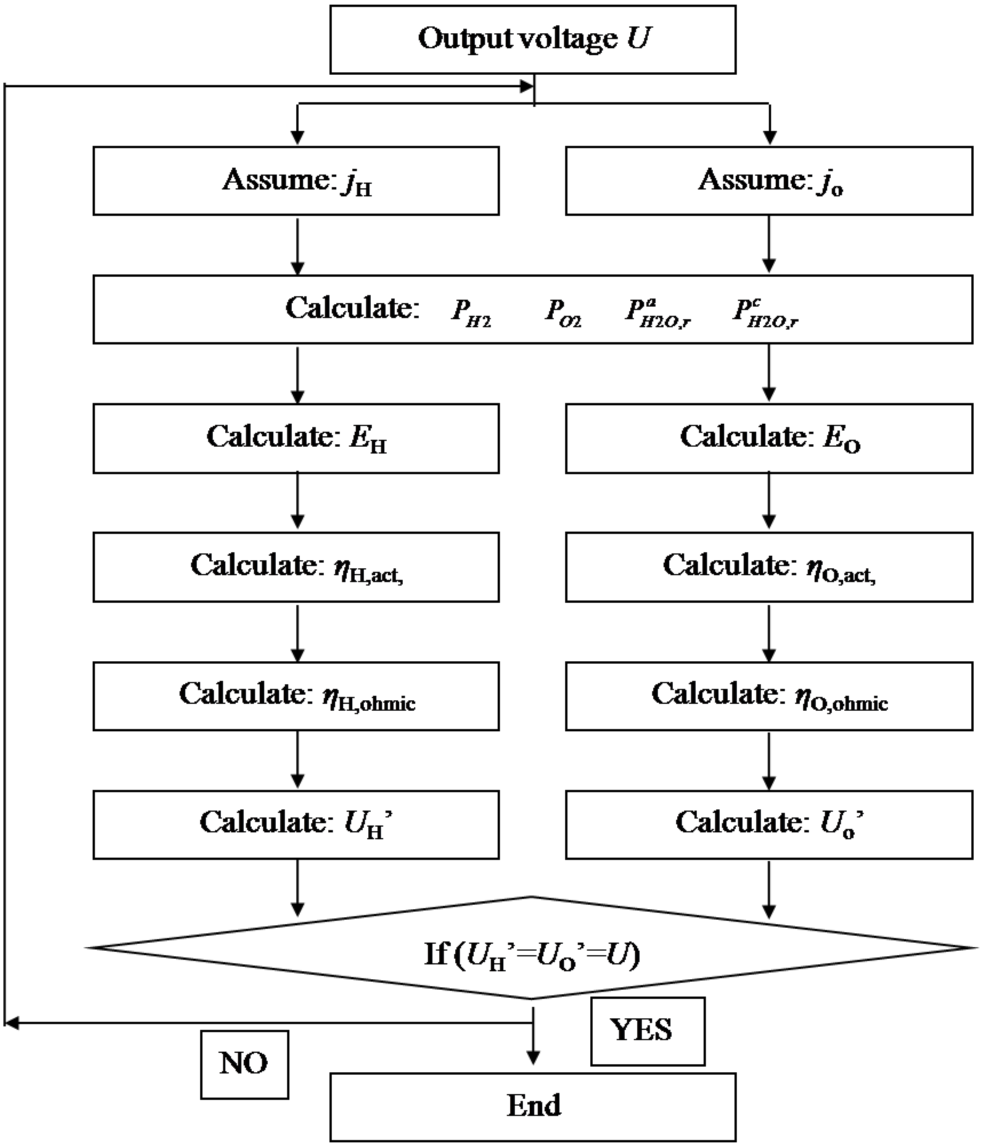

Figure 2.2 Flow diagram of the calculation procedure

The calculation procedure is performed with MATLAB® and the DGM is solved with the built-in solver *ode45*. To conduct model validation, an oxygen ion conducting SOFC is simulated by setting t_H=0 in present model. The values of parameters used for model validation are summarized in Table 2.1. The cell performance and various losses are calculated and compared with results in [11]. As shown in Figure 2.3, results from present model fit well with the literature data. The slight difference between the anode concentration losses is due to the different calculation methods used to calculate the gas distribution in present model and in literature.

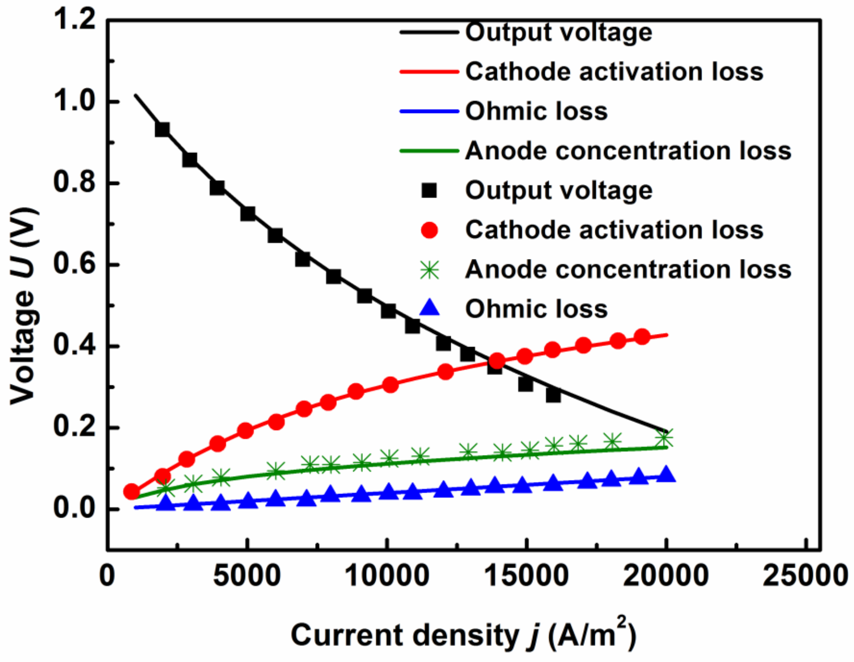

Figure 2.3 Comparison between present model and literature model [11]

2.4 Results and discussion

In this section, the performances of co-ionic SOFCs with three different supporting structures are simulated and compared: the anode-supported, the cathode-supported and the electrolyte-supported. A total conductivity of 3.86 S/m (from $BaCe_{0.9}Sm_{0.1}O_{3-a}$ at 1073 K, a typical co-ionic conducting material) is used for the electrolyte [33]. The gas molar ratio in the anode channel is H_2:H_2O=0.968:0.032 (humidified at 298 K) [83], while the ratio in cathode

Table 2.1 Parameters used for simulation and model validation

Parameter	Value	Unit
Operating temperature, T	1073	K
Operating pressure, P	10^5	Pa
Thickness of anode/electrolyte/cathode anode-supported cathode-supported electrolyte-supported (for model validation)	500/50/50 50/50/500 50/500/50 750/40/50 [11]	µm
Porosity, θ_p	0.3	
Tortuosity, τ (for model validation)	3 6 [11]	
Conductivity, σ (for model validation)	3.86 [33] 10 [11]	S/m
Average pore radius, r_p	0.5	µm
Universal gas constant, R	8.314	J/(mol K)
Faraday constant, F	96485	C/mol
Exchange current densities, j_0 anode cathode	5300 [11] 2000 [11]	A/m^2
Gas molar ratio in anode channel	H_2:H_2O=0.968:0.032 [83]	
Gas molar ratio in cathode channel	O_2:N_2:H_2O=0.21:0.78:0.01	

channel is O_2:N_2:H_2O=0.21:0.78:0.01 (simulate the air). Other parameters used for simulation are summarized in Table 2.1. It should be mentioned that, the exchange current densities in anode and cathode are assumed to be the same as O-SOFC, due to lack of experimental data. As a result, with fixed current density, the differences between the output voltages obtained upon different conditions, are caused by the different mass transport in electrodes.

2.4.1 Co-ionic SOFC performance upon different supporting structure

The performances of co-ionic SOFCs with different supporting structures are shown in Figure 2.4~Figure 2.6. It is interesting to see that co-ionic SOFCs (when $t_H = 0.5$) always perform better than O-SOFCs ($t_H = 0$) and H-SOFCs ($t_H = 1$). However, it should be noted that limiting current densities occur in the cathode-supported configurations first, due to the insufficient oxygen transport under large current densities.

In addition, it is found that H-SOFCs have better performance than O-SOFCs in anode-supported configurations (Figure 2.4) while O-SOFCs perform better than H-SOFCs in cathode-supported configurations (Figure 2.6). For comparison, the differences between O-SOFCs and H-SOFCs seem to be small in electrolyte-supported configurations (Figure 2.5), as the concentration loss is small in thin electrodes. Besides, by comparing Figure 2.4 and Figure 2.6, it can be found that the cathode-supported structure is more favorable for O-SOFC (before limiting current densities occur at quite low operating voltages) while the anode-supported structure is preferred for H-SOFC. The results seem to indicate that the diffusion of water is predominant and the electrode which generates water is not suitable to be the supporting part. It should be noted that, for co-ionic SOFC with $t_H = 0.5$, the anode supported structure stands out as clearly superior over the other two structures.

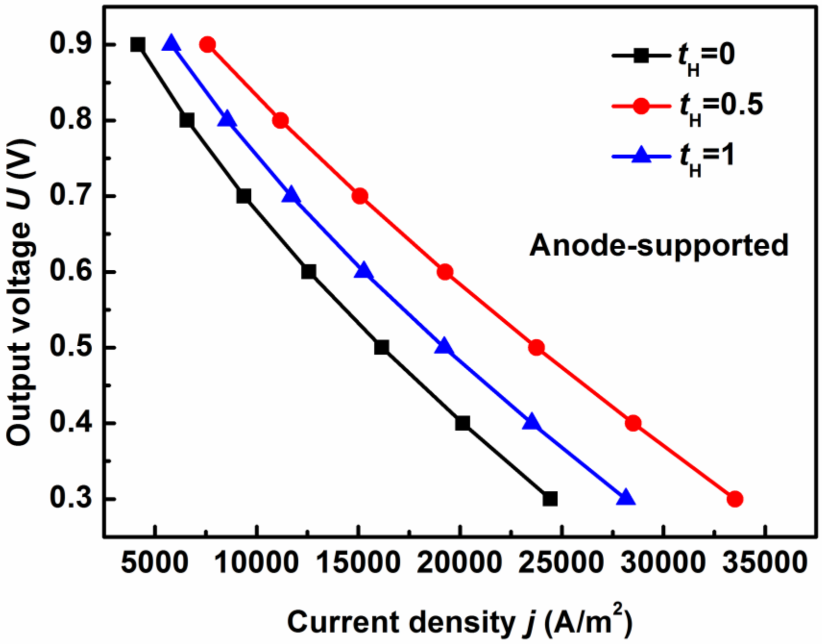

Figure 2.4 SOFC performance with anode-supported structure

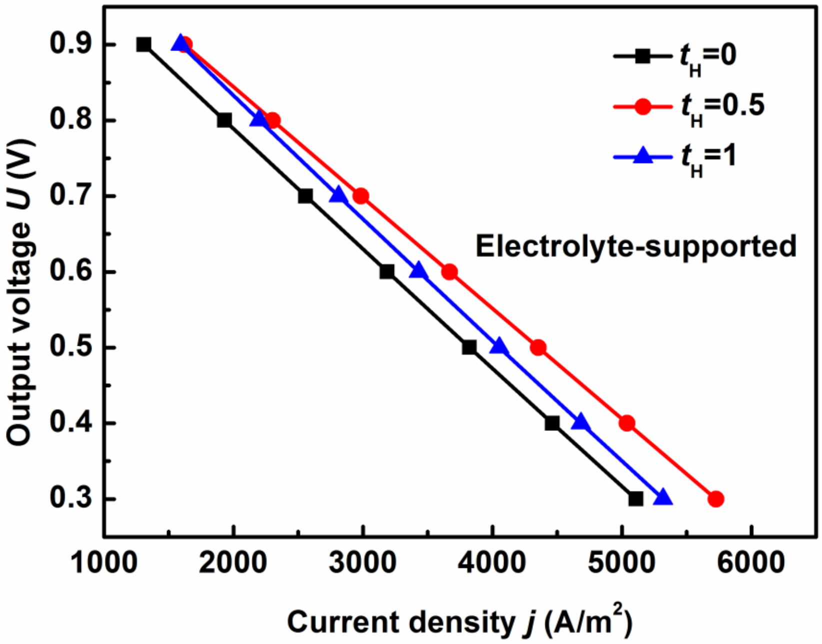

Figure 2.5 SOFC performance with electrolyte-supported structure

After that, performance simulations are conducted to investigate the effect of proton transfer number (t_H) on co-ionic SOFC with different supporting structures. Three output voltages (U=0.9 V, 0.6 V and 0.3 V) are chosen to represent different operating regions. With a given U, the current densities with different t_H can be obtained, as shown in Figure 2.7~Figure 2.9. For anode-supported SOFC (as shown in Figure 2.7), the current densities increase first with increasing t_H, and then decrease, upon the same output voltages. The best performance occur when t_H are about 0.6. For comparison, the maximum current densities are found at a t_H value of 0.4 for cathode-supported SOFC when the output voltages are 0.9 V and 0.6 V, as shown in Figure 2.9. However, at a low output voltage of 0.3 V, the O-SOFC performs best among co-ionic SOFCs with different t_H. The effect of t_H on co-ionic SOFC with electrolyte-supported structure is not obvious probably because the thin electrodes facilitate the gas transport. The results indicate the feasibility of improving the co-ionic SOFC performance by chosen an appropriate t_H value.

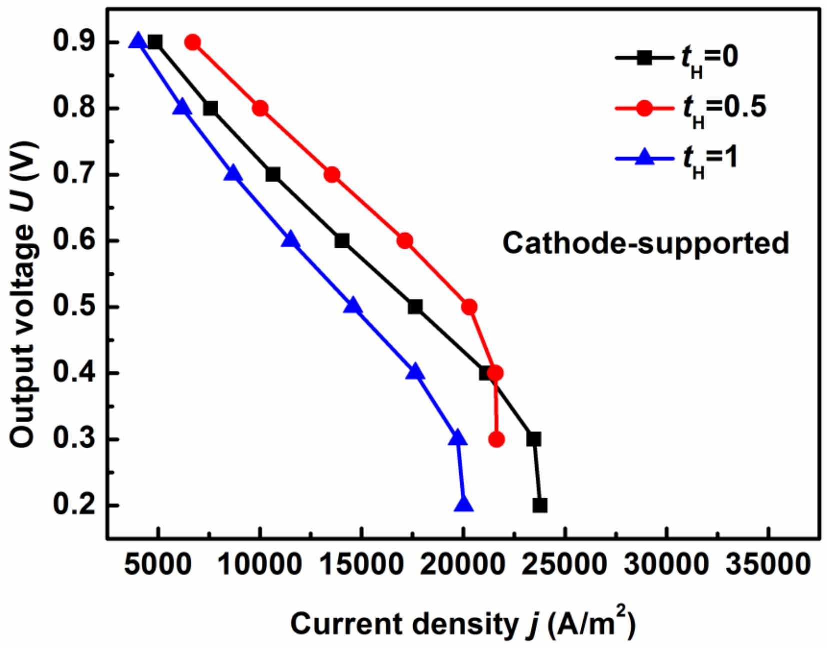

Figure 2.6 SOFC performance with cathode-supported structure

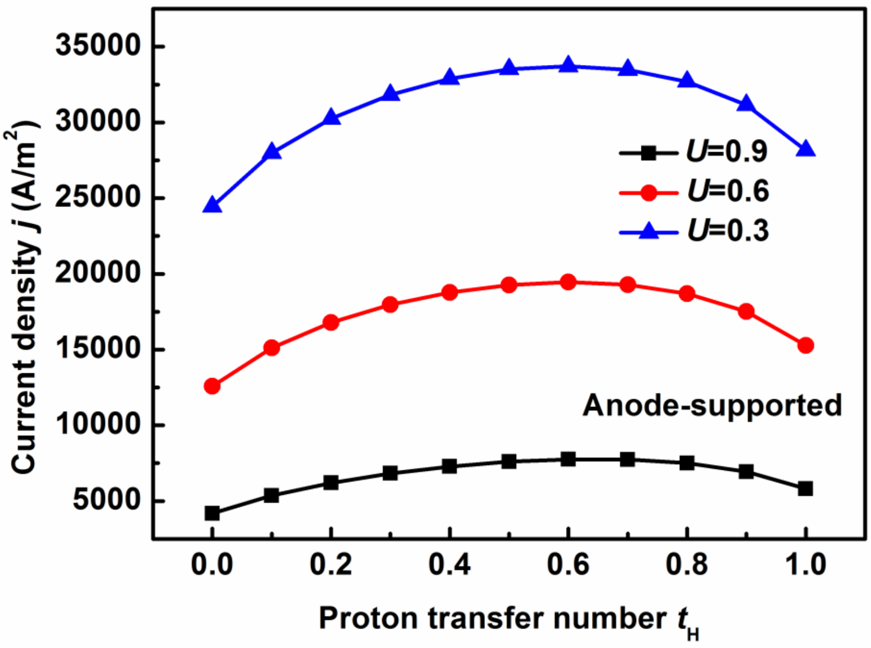

Figure 2.7 Effect of t_H on anode-supported co-ionic SOFC

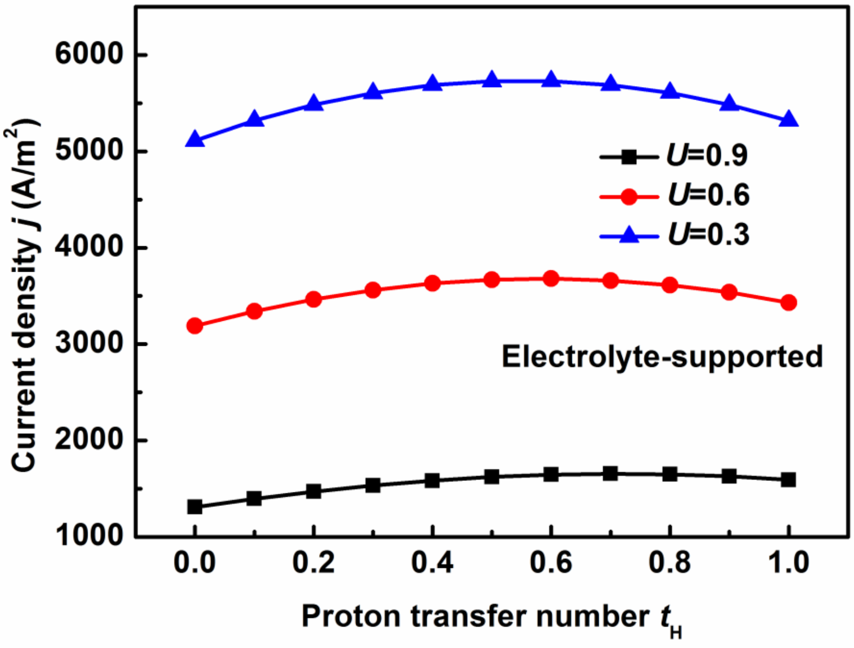

Figure 2.8 Effect of t_H on electrolyte-supported co-ionic SOFC

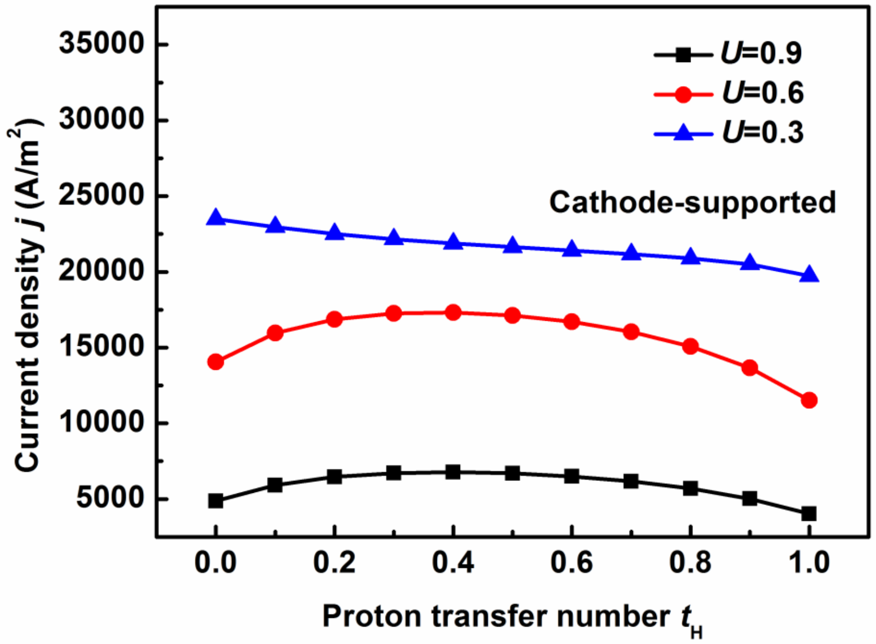

Figure 2.9 Effect of t_H on cathode-supported co-ionic SOFC

2.4.2 Concentration losses in co-ionic SOFC electrodes

As declared above, the co-ionic property only affects the mass transport in electrodes when the electrolyte conductivity is fixed. In addition, the gas transport only affects the cell performance by the concentration loss in present model. Therefore, results in section 2.4.1 also reflect the effects of the co-ionic property on the total concentration losses in co-ionic SOFC. For a better understanding of the co-ionic effect on the particular mass transport in co-ionic SOFC electrodes, variation of the concentration loss in each electrode with different t_H is shown in Figure 2.10. For anode-supported co-ionic SOFC, the anode concentration loss decreases while the cathode concentration loss increases as t_H changes from 0 to 1. As a result, the anode concentration loss dominates in O-SOFC while the cathode concentration loss dominates in H-SOFC. Besides, it can be found from Figure 1.10 that the differences between the anode concentration loss and the cathode concentration loss can be reduced at certain proton transfer numbers.

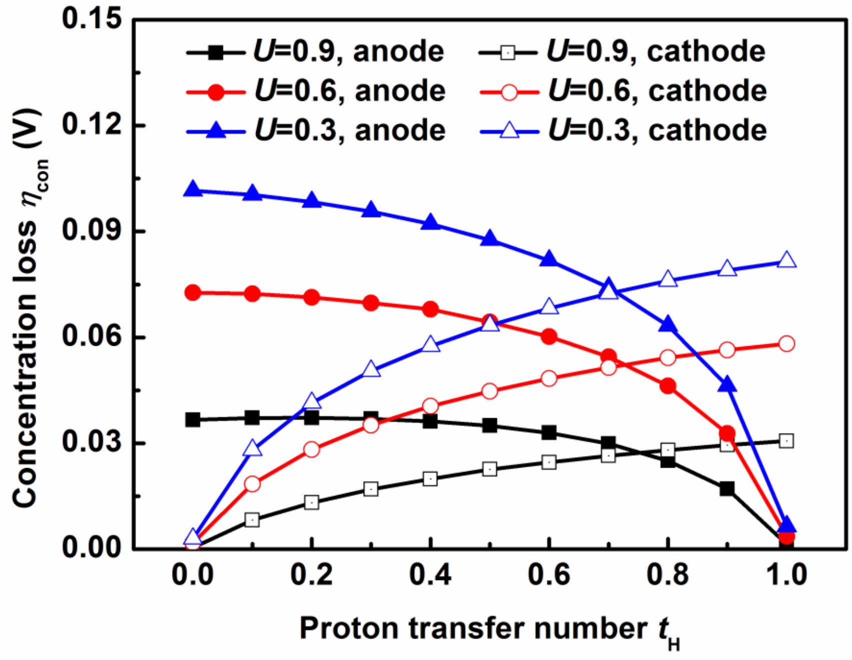

Figure 2.10 Variations of concentration losses with different t_H

2.5 Two-dimensional (2D) model of co-ionic SOFC fed with various fuels

The model presented in the previous section can be used to predict the performance of a lab-scale SOFC. But it's insufficient to analyze the performance of a real SOFC as the gas composition and current density vary along the channel. In this section, a 2D segment model is developed to account for the parameter variations of the co-ionic SOFC along the flow channel direction. As high fuel flexibility is one of the main attractions of SOFC, both pure hydrogen and syngas are considered as fuel.

Figure 2.11 shows the schematic diagram of the developed 2D co-ionic SOFC model fed with H_2 and CO mixture. The cell consists of 5 parts: the fuel gas channel, the oxidant gas channel, the porous anode, the porous cathode and the dense electrolyte. To simplify calculation, the cell is separated into many equal-length segments along the gas flow direction (z direction, as illustrated in Figure 2.11). In each segment (except the channels), the cell performance is simulated by the 1D model along the cell thickness direction (x direction).

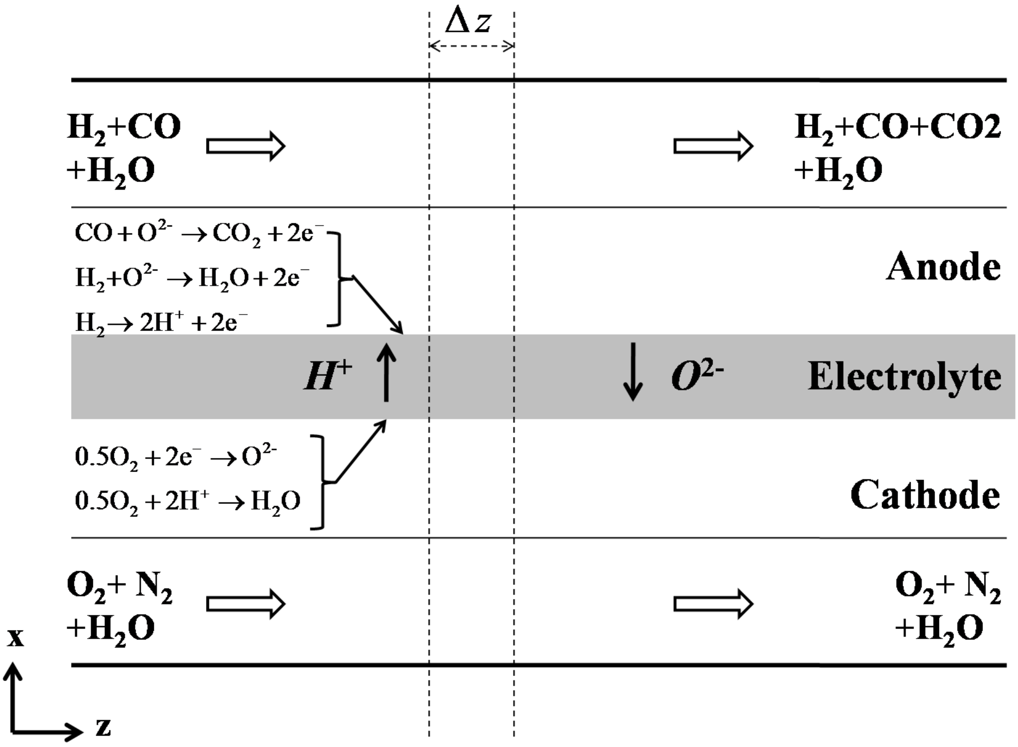

Figure 2.11 Schematic diagram of the 2D segment model of co-ionic SOFC

In gas channels:

For mass transport in gas channels, only the main stream flow direction (z direction) is considered. The gas velocity (u) is assumed to be constant, i.e. u always equal to the inlet gas velocity (u_{inlet}). Since there are electrochemical reactions (and chemical reactions when CO is involved) in electrodes, net mass fluxes (N_{i}) exist in the electrode/channel (E/C) interfaces. Therefore, for any species in gas channels, the concentration change in each segment can be described as [105]:

$$u\frac{\Delta c_i}{\Delta z} = \frac{N_i}{H_{channel}} \tag{2.23}$$

Where, u is the velocity in gas channel, (m/s); H_{channel} is the height of gas channel, (m); c_{i} is the molar concentration of gas species i and N_{i} is the molar flux of gas species i in E/C interface, (mol/(m^2 s)).

The 1D model:

When pure H_2 is used as fuel, the 1D model in each segment is exactly the same as described in section 2.2. However, when syngas (a mixture of H_2 and CO) is used as fuel, the 1D electrochemical model needs to be improved in the following parts:

1) Water gas shift reaction ((WGSR, Eq. (2.24)) occurs inside SOFC anode, leading to varying mass fluxes along the cell thickness direction (Eq. (2.20)).

$$CO + H_2O \leftrightarrow CO_2 + H_2 \tag{2.24}$$

$$-\frac{dN_{H2O}}{dx} = -\frac{dN_{CO}}{dx} = \frac{dN_{H2}}{dx} = \frac{dN_{CO2}}{dx} = r_{WGSR} \tag{2.25}$$

Where, r_{WGSR} refers to the reaction rate of WGSR (mol/(m^{3}s))and it can be determined by the relationship proposed by Haberman et al. [106-107]:

$$r_{WGSR} = k_{sf}\left(P_{H2O}P_{CO} - \frac{P_{H2}P_{CO2}}{K_{ps}}\right) \tag{2.26}$$

$$k_{sf} = 0.0171\exp\left(\frac{-103191}{RT}\right) \tag{2.27}$$

$$K_{ps} = \exp\left(-0.2935Z^3 + 0.6351Z^2 + 4.1788Z + 0.3169\right) \tag{2.28}$$

$$Z = \frac{1000}{T} - 1 \tag{2.29}$$

2) Both H_2 and CO can be oxidized in SOFC anode. Therefore, when CO is included in the fuel gas mixture, the electrochemical reactions involved in the E/E interface of anode and cathode should be:

Anode:

$$CO + O^{2-} \rightarrow CO_2 + 2e^- \tag{2.30}$$

$$H_2 + O^{2-} \rightarrow H_2O + 2e^- \tag{2.31}$$

$$H_2 \rightarrow 2H^+ + 2e^- \tag{2.32}$$

Cathode:

$$0.5O_2 + 2e^- \rightarrow O^{2-} \tag{2.33}$$

$$0.5O_2 + 2H^+ \rightarrow H_2O \tag{2.34}$$

The extra electromotive force caused by the CO oxidation can be obtained as:

$$E_{CO} = 1.46713 - 0.00024527T - \frac{RT}{2F}\ln\left(\frac{P^a_{CO2,r}}{P_{CO,r}P^{0.5}_{O2,r}}\right) \tag{2.35}$$

2.6 Results of the 2D model

In this part, the distributions of current densities and molar fractions of gas species along the gas flow direction are presented. The calculations are based on the anode-supported co-ionic SOFC (t_H=0.5) operated at 0.7 V. Two kinds of gases are used as fuel: 1) humidified H_2 consists of 96.8% H_2 and 3.2% H_2O; 2) syngas consists of 45% H_2, 45% CO and 10% H_2O. As reported by Matsuzaki et al. [108] that the H_2 electrochemical oxidation rate was 1.9~3.1 times higher than that of CO, therefore, in this work, the anode exchange current density for CO oxidation is assumed to be 1/2.5 times of that for H_2 oxidation (5300 A/m^2), i.e. 2120 A/m^2 [109]. The gas channel height and channel length are 1 mm and 5 cm, respectively. Along the gas flow direction, the channels are segmented into 50 parts.

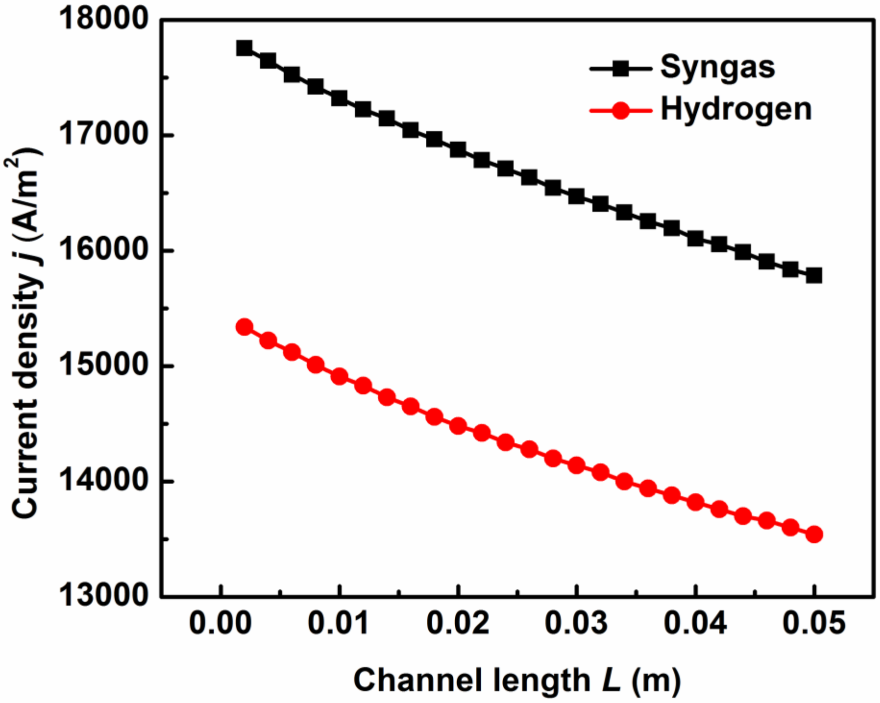

Figure 2.12 Distribution of total current densities along gas channels

Figure 2.12 shows the total current density distributions in gas channels of co-ionic SOFC fed with hydrogen and syngas, respectively. Large variations of current density along the gas channel are observed, indicating that the model is capable of capturing the parameter variation in a practical SOFC. It can be seen that the syngas fueled SOFC performs better than hydrogen fueled SOFC. For a better understanding of the result, the detailed current densities caused by different mechanisms are shown in Figure 2.13. When hydrogen is used as fuel, two kinds of current involved in the cell: the current caused by the proton conduction (j_{H}) and current caused by oxygen ion conduction (j_{O}). When CO is involved, an extra current exists due to the CO oxidation reaction (j_{CO}). It can be seen from Figure 2.13 that the j_{H} and j_{O} of hydrogen fueled SOFC are larger than their counterparts in syngas fueled SOFC because of the high hydrogen concentration. Therefore, the better performance of syngas fueled SOFC is attributed to the extra CO oxidation reaction. In addition, compared with the small variations of j_{O} and j_{CO} along the gas channel, variations of j_{H} are more significantly in both hydrogen fueled SOFC and syngas fueled SOFC (as shown in Figure 2.13). Along the gas channel, the electrode structures are always the same and only gas distributions are varied. Besides, the gas distributions affect j_{O} and j_{H} through the concentration items in the Nernst equation (Eq. (2.6) & Eq. (2.7)), therefore, the results seem to indicate that j_{H} is more sensitive to the water partial pressure in SOFC cathode than j_{O} to the water partial pressure in SOFC anode.

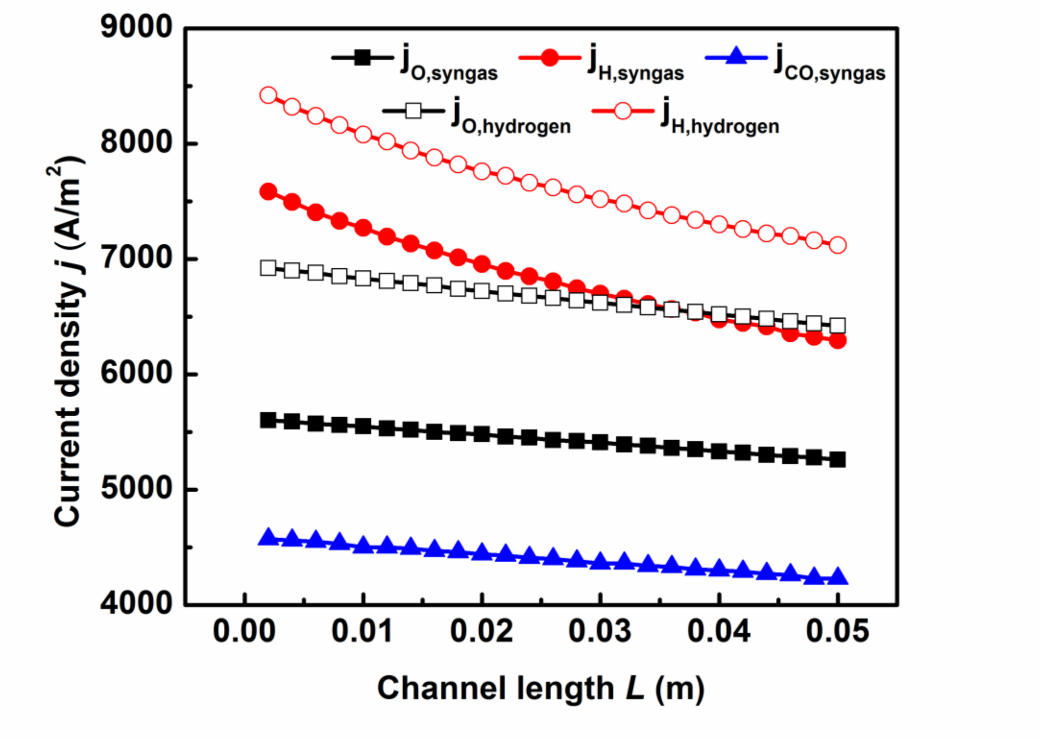

Figure 2.13 Distribution of separate current densities along gas channels

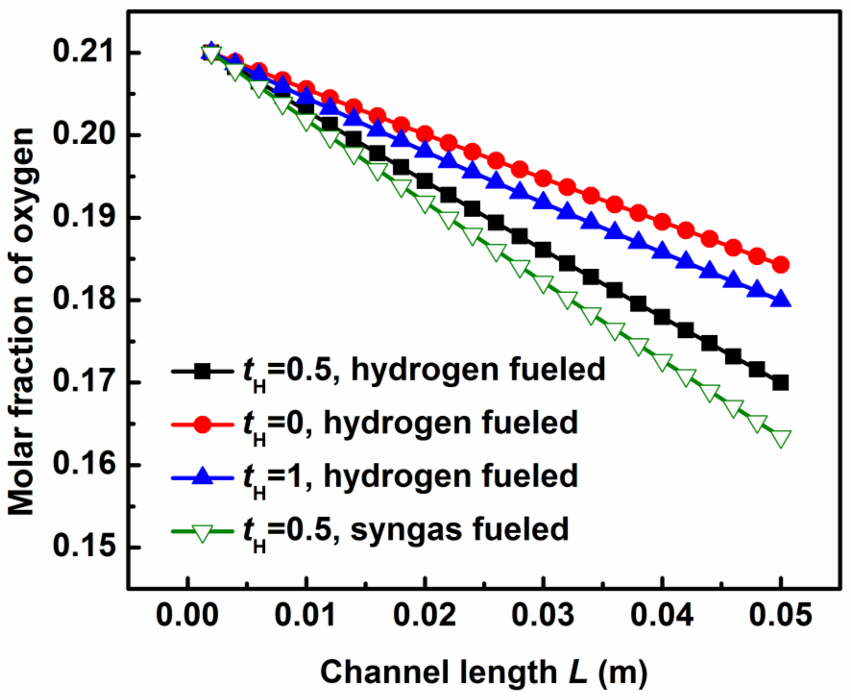

Figure 2.14 Distribution of O_2 in cathode

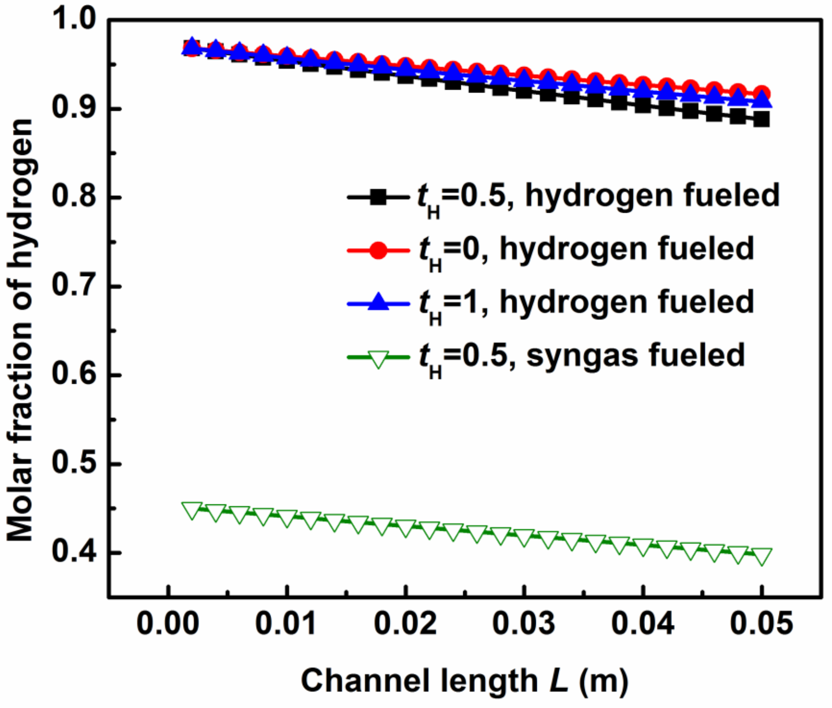

Figure 2.15 Distribution of H_2 in cathode

The distributions of oxygen and hydrogen along the gas channels are shown in Figure 2.14 and 2.15, respectively. For comparison, O-SOFC and H-SOFC fueled with humidified H_2 are also calculated and presented. Since co-ionic SOFC has better performance than SOFC with pure conducting electrolyte and higher current density can be obtained under the same operating voltage (shown in section 2.4), it is easy to understand why co-ionic SOFCs also have higher oxygen and fuel utilization efficiencies.

2.7 Conclusions

In this chapter, mathematical models for SOFC with co-ionic conducting electrolyte (co-ionic SOFC) are developed for performance analysis. Based on the 1D model, the effects of different supporting structures and proton transfer numbers (t_H) are investigated. Results show that, comparing with previous pure ion (O^{2-} or H^+) conducting electrolytes, the co-ionic conducting electrolyte can improve the cell performance and reduce the concentration loss difference between anode and cathode at certain proton transfer number. After that, the 1D model is extended to 2D, based on which the distributions of current densities and gas molar fractions along the gas channel direction in co-ionic SOFC fed with various fuels are examined. Results show that, syngas mixture is superior to hydrogen when used as fuel in co-ionic SOFC. Furthermore, comparing with pure ion conducting SOFC, co-ionic SOFC has higher oxygen and fuel utilization efficiencies. This work improves our understanding of co-ionic SOFC and provides theoretical guidance for experimental researchers to improve co-ionic SOFC performance.

CHAPTER 3 PREDICTION OF PARTIAL CONDUCTIVITY IN CO-IONIC CONDUCTING ELECTROLYTE

In chapter 2, the effect of the co-ionic conducting electrolyte on SOFC performance is investigated. As a further step, in this chapter, a numerical procedure is developed to numerically construct the dual-phase composite co-ionic electrolyte and predict the electrolyte partial conductivities, which are important property parameters of the co-ionic electrolyte. The partial conductivities are also necessary inputs of the mathematical models developed in chapter 2.

3.1 Introduction

For SOFC with co-ionic conducting electrolyte, the cell performance is affected by the partial conductivities of different conducting phases in the electrolyte [33, 50, 95]. However, unlike electrolytes conducting a single type of ions, the partial conductivities of different conducting phases in the co-ionic conducting electrolyte are difficult to be measured precisely [49, 110]. In addition, the partial conductivities of different conducting phases in co-ionic conducting electrolyte are linked with the electrolyte micro parameters, such as electrolyte composition and electrolyte particle sizes. Therefore, comparing with experimental investigation, it’s cost-effective to develop a numerical model to establish a relationship between the partial conductivities of different conducting phases of the co-ionic conducting electrolyte and the electrolyte micro parameters. The model can be conveniently used for parametrical simulations and can provide useful guidance for the future electrolyte material design. It should be mentioned that, although a general relation is already proposed by Wu et al. [111] to predict the conductivity in randomly mixed multi-phase composite, the relationship totally neglects the electrolyte microstructure effect, which describes the distributions of different constituent phases and determines the effective conducting paths.

In this chapter, a 3D model of the dual phase composite co-ionic conducting electrolyte is numerically constructed using a random cube packing procedure. The constructed electrolyte consists of two separate phases [112]: one phase is the oxygen ion conductor (e.g. SDC ($Ce_{0.8}Sm_{0.2}O_{1.9}$)) for oxygen ion conduction, and another phase is the proton conductor (e.g. BCS ($BaCe_{0.8}Sm_{0.2}O_{2.9}$)) for proton conduction. The partial conductivities of different conducting phases (σ_{eff}) are obtained by solving the steady-state charge conservation equations in the conducting phase and the free space, respectively [65, 113].

3.2 Methodology

Although SOFC electrolyte is fabricated from powders with various shapes and of a wide size distribution in reality, the electrolyte powers are approximated by uniformly sized cubes in this work for simplicity. The detailed procedure is designed as following (implemented with MATLAB®):

First, the co-ionic conducting electrolyte consisting of 2 separate phases is numerically constructed using a random cube packing procedure, as shown in Figure 3.1. The ratio of cube size to voxel size (L_{cube} / L_{voxel}) is set as 5, that is, each cube contains 5^3 voxels. One phase is assigned with positive values to represent the oxygen ion conductor while another phase is assigned with negative values to represent the proton conductor. The composition of the electrolyte can be handled by controlling the cube number ratio between different conducting phases.

Second, steady-state charge conservation equations (Eq. (3.1)) are solved in a conducting phase and the free space to obtain current fluxes j_{eff} and j_0, respectively [65, 113]. The boundary conditions required for the calculation are labeled in Figure 3.1. The effective conductivity ratio ($\sigma_{\mathrm{eff}}/\sigma_0$) of the computed conducting phase can be obtained by Eq. (3.2). Since no physical property parameter is involved in the computing process, the $\sigma_{\mathrm{eff}}/\sigma_0$ of another conducting phase can be obtained in the same way. It is worth noting that in this work, the effective conductivity ratio $\sigma_{\mathrm{eff}}/\sigma_0$ is used so that all the results are free of any material property and can be applied to any material.

$$j_i = \sigma_i \nabla \phi \quad i = 0 \ or \ eff \tag{3.1}$$

$$\frac{\sigma_{eff}}{\sigma_0} = \frac{j_{eff}}{j_0} \tag{3.2}$$

where, σ_0 refers to the intrinsic conductivity of the computed conducting phase (S/m). Subscripts *0* and *eff* represent the intrinsic and effective properties, respectively.

Finally, for a better understanding of the microstructure effect on the partial conductivities, the percolation probability (P_{erco}) which refers to the probability that one conductive particle belongs to a continuous conduction network throughout the electrolyte is also calculated as:

$$P_{erco} = \frac{N_{i,perco}}{N_i} \tag{3.3}$$

where, N_{i} and $N_{\mathrm{i,perco}}$ refer to the voxel number of the conducting phase in the electrolyte and in the percolated network, respectively.

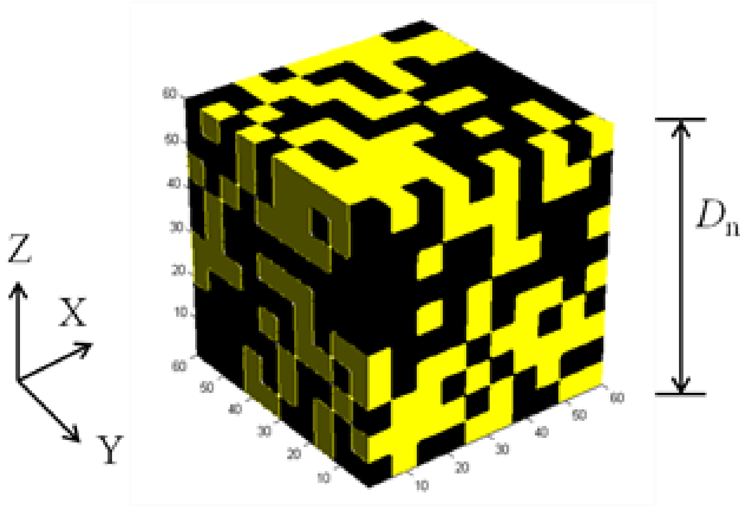

Boundary conditions for σ:

face $Z=0,\ \phi=0;$

face $Z=D_n,\ \phi=1;$

other faces, $\nabla\phi=0.$

Figure 3.1 Constructed co-ionic electrolyte

3.3 Results and Discussion

3.3.1 Effect of computational parameters

To adequately represent the complex microstructure of a composite material, a sufficient large computational domain is necessary [62, 64]. Therefore, the computational domain size effect is examined first. Since the electrolyte thicknesses are usually less than 20 μm, 10 cases including 2 kinds of electrolyte thicknesses (Z direction) and 5 kinds of cross section areas (X direction×Y direction) are designed, as shown in Figure 3.2. Each cube represents an electrolyte particle and the cube length is 1 μm (i.e., $L_{\mathrm{cube}}=1$ μm). It should be mentioned that, considering the random nature of the packing process to generate the electrolyte and different electrolyte microstructure can be produced even with the same manufacturing parameters, each case is repeated for 20 times to ensure the results are statistically invariant. The volume ratio of the two conducting phase is kept as 1:1 during calculation.

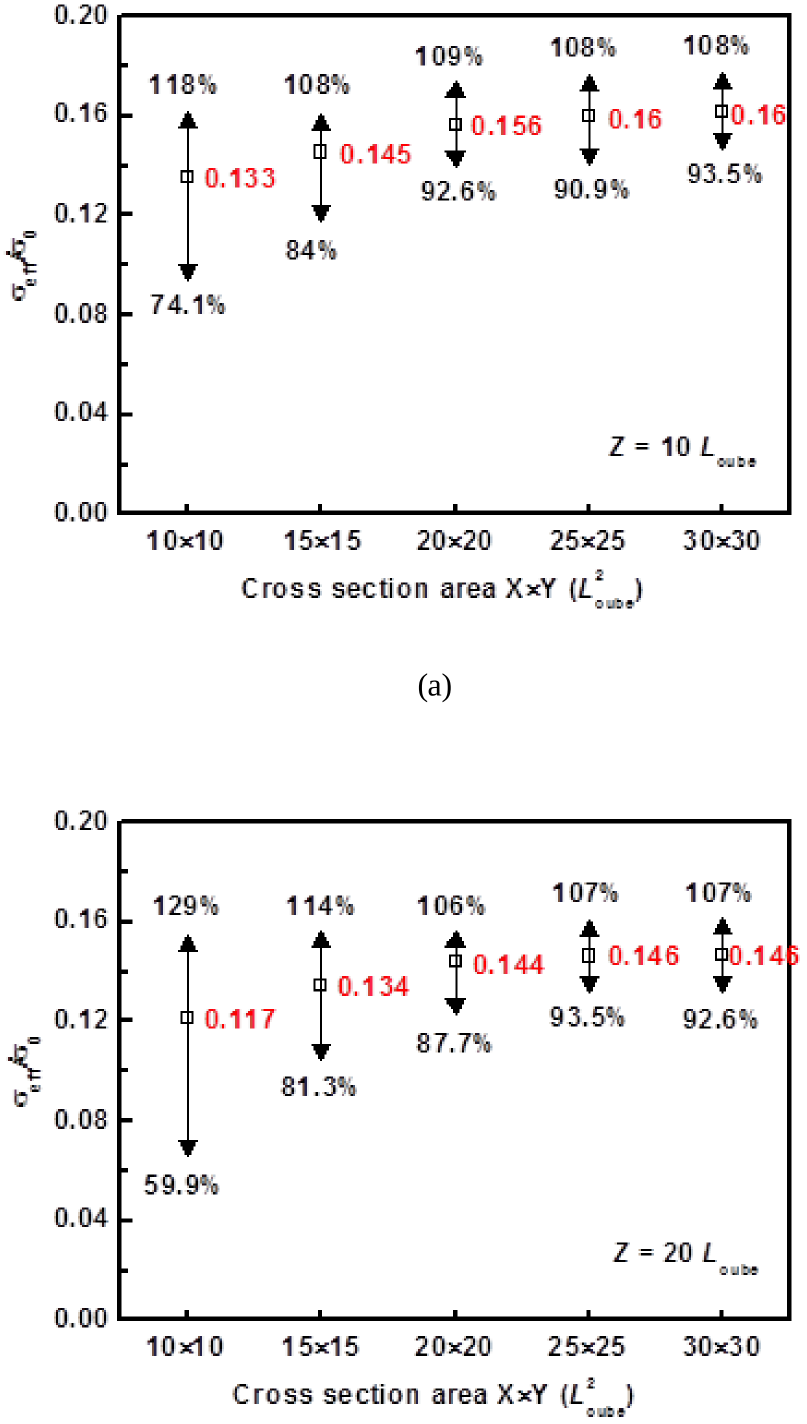

(a)

(b)

Figure 3.2 Effects of computational domain

Figure 3.2(a) shows the cases with electrolyte thickness of 10 μm ($10L_{\mathrm{cube}}$), and Figure 3.2(b) shows the cases with electrolyte thickness of 20 μm ($20L_{\mathrm{cube}}$). The red characters in Figure 3.2 represent the 20 times average values while the upper and lower fractions represent the largest positive deviations and the smallest negative deviations of a single time calculation result from the 20 times average value, respectively. It can be seen from Figure 3.2 that with the same electrolyte thickness, increasing the cross section area decreases the 20 times average value, as well as the largest deviation. Take Figure 3.2(a) as an example, for an electrolyte with 10 μm thickness, when the cross section areas are larger than 20*20 μm^2, the largest deviations are less than 10%. Moreover, only less than 5% difference exists between the 20 times average value of the 20*20 μm^2 cross section area and its value of the further increased cross section areas. Therefore, in this work, the 20*20 μm^2 cross section area is regarded as the minimum cross section area to represent the electrolyte of 10 μm thickness. Similarly, from Figure 3.2(b), a 25*25 μm^2 cross section area is determined as the minimum cross section area for the electrolyte with 20 μm thickness.

In addition, by comparing the 2 figures in Figure 3.2, it can be seen that the 10 μm thin electrolyte has a slightly higher (about 1.1 times) effective conductivity, compare with the 20 μm electrolyte.

3.3.2 Effect of volume fraction

Based on the 30×30×10 μm^3 (X×Y×Z) computational domain, the $\sigma_{\mathrm{eff}}/\sigma_0$ and P_{erco} of the computed conducting phase with different volume fractions (ψ) are calculated and compared with literature data [48, 66], as shown in Fig 3.3 and Figure 3.4. The red line in Figure 3.3 shows the measured proton conductivities in a SDC-carbonate composite electrolyte [48] while in Figure 3.4 it shows the percolation probability calculated from the traditional model developed by Chen et al. [66]. It can be seen that the calculated results agree with literature values well, which also validates the feasibility of the model in this work.

From the 20 times repeating calculation, we find that when the volume fraction of the conducting phase is less than 0.35, the constructed electrolyte is quite unstable and percolation can be found only in particular structures. In addition, the $\sigma_{\mathrm{eff}}/\sigma_0$ of the calculated conducting phase is almost zero when its volume fraction is less than 0.35. However, when the volume fraction is larger than 0.35, the $\sigma_{\mathrm{eff}}/\sigma_0$ is increased with the increasing volume fraction. This result agrees with the experimental finding, in which an abrupt increase occurs in the total conductivity of the dense Ag/YSB composite when the volume fraction of the Ag phase increases to 0.34 [111]. Besides, as shown in Figure 3.4, the calculated conducting phase begins percolate at a volume fraction of about 0.25, and forms a well percolated network ($P_{\mathrm{erco}}\approx 1$) at a volume fraction of about 0.5. Therefore, to maintain the conduction of 2 kinds of charges in such a co-ionic electrolyte, the volume fraction of each constituent phase is suggested to be between 0.35~0.65.

3.3.3 Effect of electrolyte particle size

Based on the electrolyte of 10 μm thickness, the $\sigma_{\mathrm{eff}}/\sigma_0$ and P_{erco} with different particle size (r) is calculated, as shown in Figure 3.5 and Figure 3.6. It can be seen that as the particle radius changes from 0.25 μm to 1 μm, $\sigma_{\mathrm{eff}}/\sigma_0$ only increases slightly. However, it is worth noting that the percolation threshold of large particles is obviously lower than that of small particles.

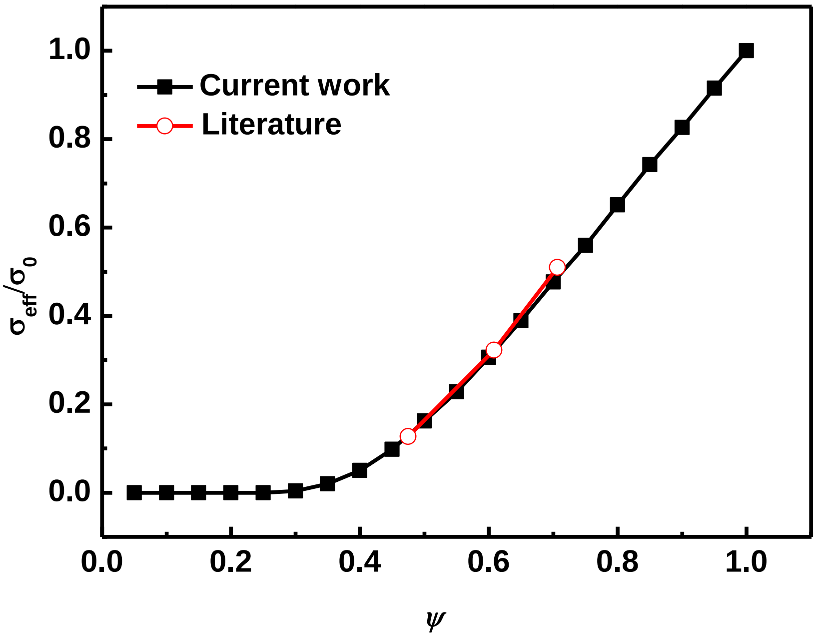

Figure 3.3 Effect of volume fraction Ψ on σ_{eff}/σ_0

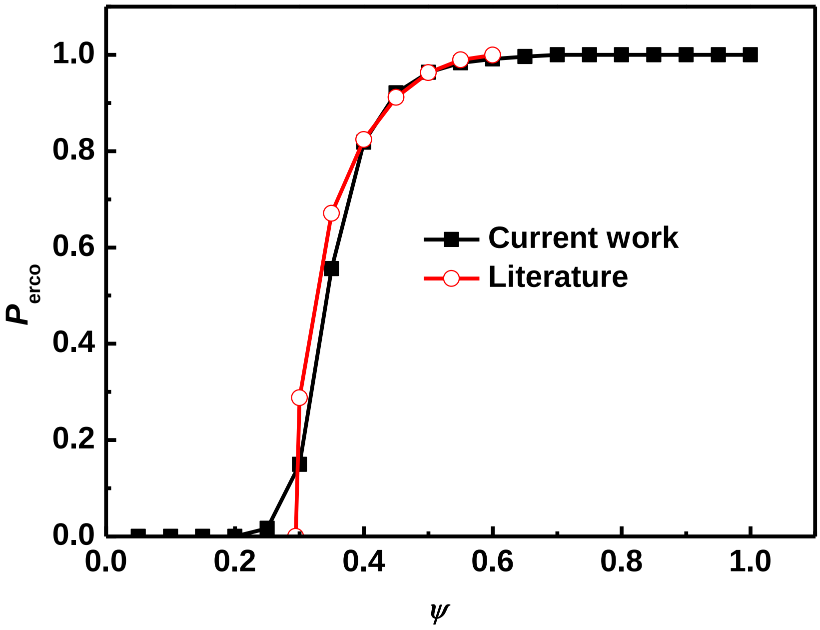

Figure 3.4 Effect of volume fraction Ψ on P_{erco}

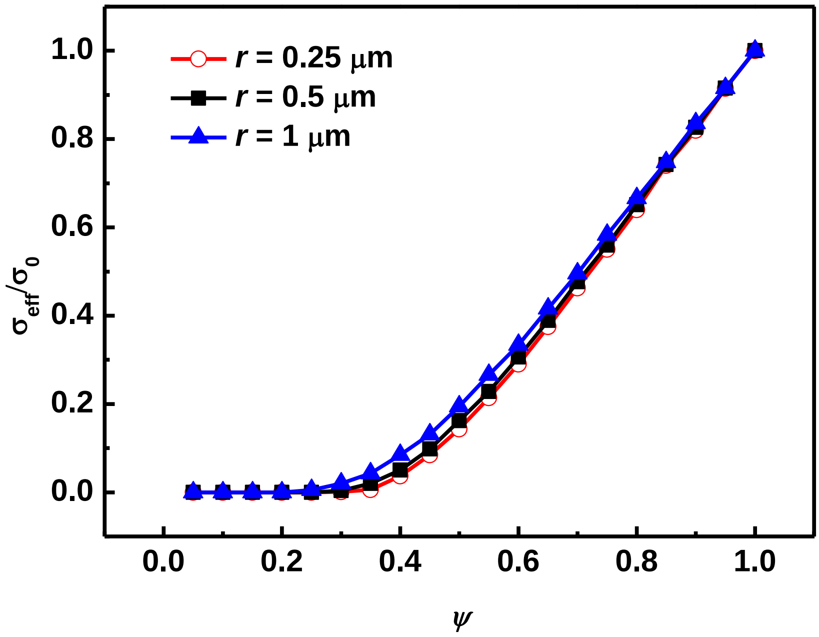

Figure 3.5 Effect of particle radius r on σ_{eff}/σ_0

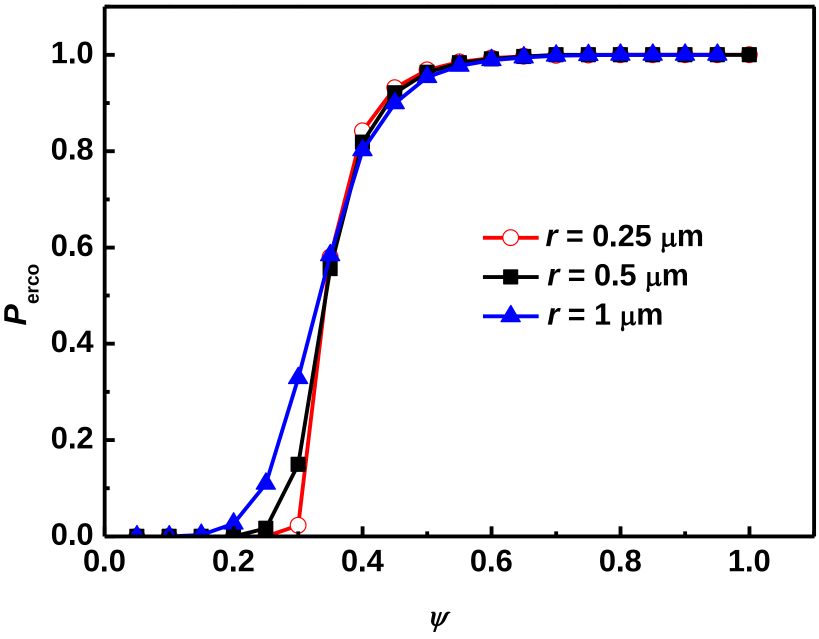

Figure 3.6 Effect of particle radius r on P_{erco}

3.3.4 New relationship

Finally, as the σ_{eff}/σ_0 is insensitive to the electrolyte particle size, a new relationship is proposed by fitting the calculated σ_{eff}/σ_0 with different volume fractions (ψ), as shown in Eq. (3.4). The comparison between the new relationship and the calculated results are shown in Figure 3.7. Such an expression provides an efficient approach to calculate the effective partial conductivities of the different conducting phases in co-ionic conducting electrolyte with varying compositions.

$$\frac{\sigma_{eff}}{\sigma_0} = 1.6\psi - 0.63 \tag{3.4}$$

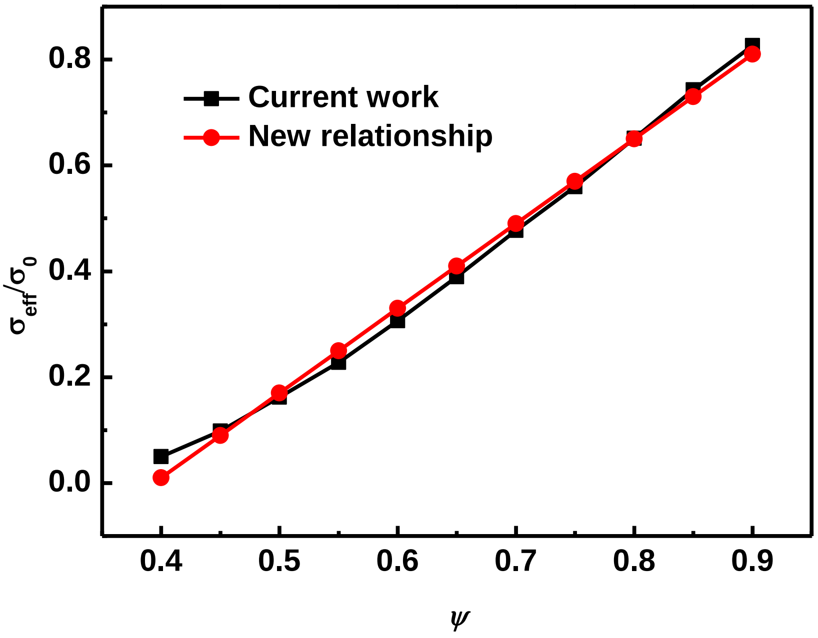

Figure 3.7 Comparison between the new relationship and modeling results

3.4 Conclusions

In this chapter, the 3D microstructure of dual-phase composite co-ionic conducting electrolyte is numerically constructed by randomly packing cubes, based on which the effective partial conductivity of different conducting phase is calculated. The effective conductivity ratio $\sigma_{\text{eff}}/\sigma_0$ is used to show the results so that all the results are free of any material property and can be applied to any material. Results show that the $\sigma_{\text{eff}}/\sigma_0$ is more sensitive to its volume fraction rather than particle size. Based on the calculated results, a relationship is fitted to predict the $\sigma_{\mathrm{eff}}/\sigma_0$ with different volume fraction. Although this work is motivated by the co-ionic conducting electrolyte in SOFC, pure geometric method is employed in the calculation process, therefore, the approach and conclusion can be generalized to any binary composite membranes [111].

CHAPTER 4 RECONSTRUCTION AND PROPERTY ANALYSIS SOFC COMPOSITE ELECTRODE

In chapter 4 and chapter 5, the relationship between SOFC electrode micro parameters and SOFC cell performance is developed, aiming at improving SOFC performance by optimizing SOFC electrodes. The whole relationship can be divided into 2 parts: the relationship between electrode micro parameters and electrode effective properties (Chapter 4) and the relationship between electrode effective properties and cell performance (Chapter 5).

4.1 Introduction

As known to all, the electrode performance is mainly determined by three kinds of losses: the activation loss due to local electrochemical reactions, the concentration loss due to gas transport and the ohmic loss due to ion/electron transport. Under typical operating conditions, the activation loss and the ohmic loss of an electrode are usually much higher than the concentration loss, thus they are the key for improving the SOFC performance.

The effective TPB length and effective conductivity are important electrode effective parameters which determine the activation loss and ohmic loss in electrode, respectively. However, by now, the relationship between electrode micro parameters and the effective TPB length are well investigated [55, 57, 59-61, 76] while the relationship between electrode micro parameters and the effective conductivity are still lacking (detailed discussion can be found in section 1.2.3.2).

Consequently, a comprehensive study was conducted in this work to investigate the σ_{eff} of SOFC composite electrode via numerical simulation. The microstructure of porous electrode is constructed numerically by randomly packing spherical particles in a computational domain, followed by a geometrical dilating procedure to simulate the sintering process [55, 113]. The effects of various parameters (particle size, contact angle, material composition, and porosity) on σ_{eff} are investigated. After that, the percolation model for the calculation of σ_{eff} is improved based on the numerical results. This work provides further insight into the relationship between electrode micro parameters and its effective conductivities.

4.2 Methodology

4.2.1 Electrode construction

A typical composite electrode is fabricated from a mixture of ion-conducting particles and electron-conducting particles, followed by a sintering process to generate penetrated networks of different conducting phases [114-116]. The approach used in this work to construct SOFC electrode is briefly introduced as following (implemented by MATLAB®):

Step 1: construction of the 3D particle packing structure. In this step, a three dimensional (3D) zero matrix is predefined to simulate the empty container. After that, spherical particles are numerically generated and dropped into the container until no vacancy exists. In the particle dropping process, the location of the particle is randomly selected from candidates with the lowest coordinate in the dropping direction. It should be mentioned that, the lowest coordinate rule for particle position selection pledged a better connection between particles in the dropping direction than the other two directions [113]. Finally, the particles are randomly assigned with values to represent their properties: positive values represent the ion-conducting phase and negative values represent the electron-conducting phase. The generated original packing structure is shown in Figure 4.1(a). The initial porosity of the packing structure is about 0.41, similar to the value in [72]. The final porosity of electrode is controlled by randomly deleting solid particles.

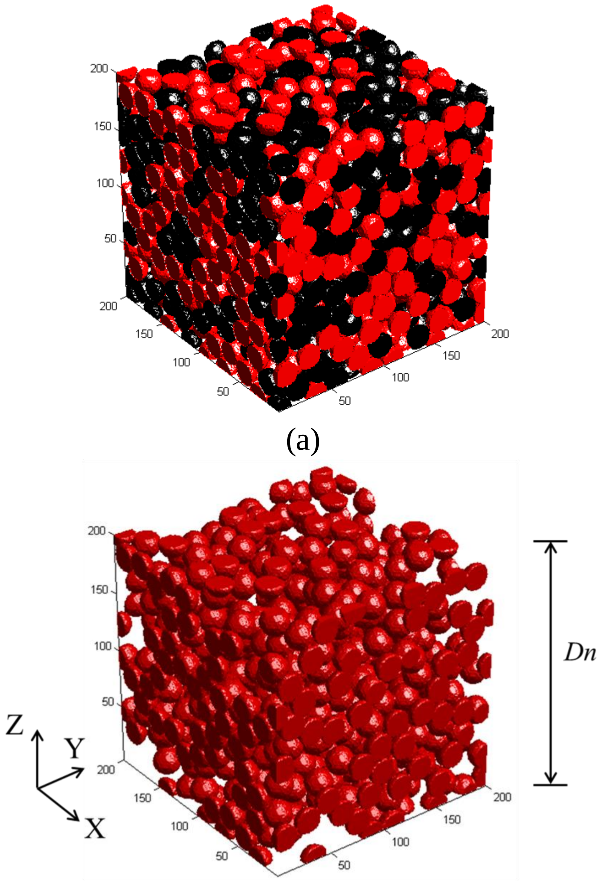

(a)

Boundary conditions:

$face\ Z = 0: \quad \phi = 0;$

$face\ Z = Dn: \quad \phi = 1;$

$other\ faces: \quad \nabla\phi = 0.$

(b)

Figure 4.1 (a) Constructed electrode by random particle packing;
(b) Boundary conditions for the calculation of effective conductivity

Step 2: dilation of particles to simulate the sintering process. In this work, the voxel length (L_{vox}) in the computational domain is unfixed while the particle radius (r) is set as 10 times of the voxel length (i.e., r=10L_{vox}) to ensure the model accuracy [74, 116]. Therefore, by expanding the particles along the particle radius by a factor of 1.1 (1 L_{vox}), contact angles of around 34$^{\mathrm{o}}$ can be generated between neighboring electrode particles [113]. Different contact angles can be formed by dilating electrode particles with different factors.

4.2.2 Calculation of effective conductivity

Based on the constructed electrode, the effective conductivity ratio ($\sigma_{\mathrm{eff}}/\sigma_0$) can be calculated. The effective conductivity ratio ($\sigma_{\mathrm{eff}}/\sigma_0$) is calculated instead of the σ_{eff} so that all the results are free of any material property and can be applied to any materials. By solving the steady-state charge conservation equations (Eq. (4.3)) in the computed conducting phase and free space, current fluxes j_{eff} and j_0 can be obtained respectively [65, 113]. The boundary conditions required for the calculation are labeled in Figure 4.1(b). The $\sigma_{\mathrm{eff}}/\sigma_0$ of the computed conducting phase can be obtained using Eq. (4.4).

$$j_i = \sigma_i \nabla \phi \quad i = 0 \;\; or \;\; eff \tag{4.3}$$

$$\frac{\sigma_{eff}}{\sigma_0} = \frac{j_{eff}}{j_0} \tag{4.4}$$

where, j_{eff} and j_0 refer to the current fluxes in the computed conducting phase and free space, respectively.

4.2.3 Calculation of percolation probability

To compare with the percolation model, the percolation probability (P_{erco}) of the computed conductive phase is also calculated. After finding the percolated network of the computed conductive phase using the built-in function *bwlabeln* in MATLAB®, the determination of percolation probability is straightforward:

$$P_{erco} = \frac{N_{i,perco}}{N_i} \tag{4.5}$$

where, N_{i} and $N_{\mathrm{i,perco}}$ refer to the element number of the *i*-conducting phase in the constructed electrode and in the percolated network, respectively.

4.3 Results and Discussion

In this section, the effects of porosity (ε), volume fraction (Ψ), contact angle (θ) and particle radius (r), on the effective conductivity ratio (σ_{eff}/σ_0) of the computed conductive phase in SOFC electrode are presented. It should be mentioned that, considering the random nature of the particle packing process to construct the electrode, different electrode microstructures can be produced even with the same manufacturing parameters [116], each case is repeated for 20 times to ensure the results are statistically invariant.

4.3.1 Effect of computational domain

A sufficient large computational domain is necessary to ensure the constructed structure can be used as a representative of a real electrode and the calculation results are reliable [62, 64]. To investigate the computational domain effect on the calculation of σ_{eff}/σ_0, 9 cases with different kinds of cross section areas (X direction × Y direction) and domain heights (Z direction, the electrode thickness direction) are designed. This is different from literature studies, in which the minimum computational domain is examined as a cube [62, 64, 116]: It is reported by choi et al. [64] that, a cubic computational domain with size length of 10*d* (*d* is the electrode particle diameter) is necessary to get a reliable σ_{eff} while Rhazaoui et al. [62] suggested that a cubic domain with size length of 8*d* is sufficient. In fact, electrodes in SOFC should be regarded as a 2D infinite thin film with limited thickness [117], for example, the cathode interlayer is commonly about 20um [27]. Therefore, as a representative of the real electrode structure, the computational domain should have the same thickness with the real electrode while the cross section area should be large enough: by further enlarging the cross section area but keep the thickness unchanged, only negligible effect can be found in σ_{eff}. The volume ratio of the ion-conducting phase to the electron-conducting phase is kept as 1:1 during calculation. The porosities of the constructed electrodes are 0.28 after dilating.

The calculated σ_{eff}/σ_0 with different domain size is shown in Figure 4.2. The red characters represent the 20 times average values of each case while the upper and lower fractions represent the largest positive deviations and the smallest negative deviations of a single time calculation result from the 20 times average value, respectively. Different figures show the results with different domain heights. The three cases in each figure show the effects of cross section area.

It can be seen from Figure 4.2 that with the same domain height (electrode thickness), the average values and the largest deviations are decreased with an increasing cross section area. In addition, compare with cases with cross section areas of $10d\times10d$, the average values with $15d\times15d$ cross section areas change within 5%. Therefore, the $15d\times15d$ is regarded as the minimum cross section area for domain heights less than $15d$. It can be also found that, with such a cross section area, the largest deviations are always less than 15%.

In addition, by comparing the three figures in Figure 4.2, only slight differences are found in σ_{eff}/σ_0 in electrodes with different domain heights (0.059 and 0.055 for domain heights of $10d$ and $15d$, respectively), which means that the σ_{eff}/σ_0 is not very sensitive to the domain height. Therefore, in the follow calculation, computational domains with cross section areas of 15*d*×15*d* and heights of 10*d* are used, as a compromise between computational cost and accuracy.

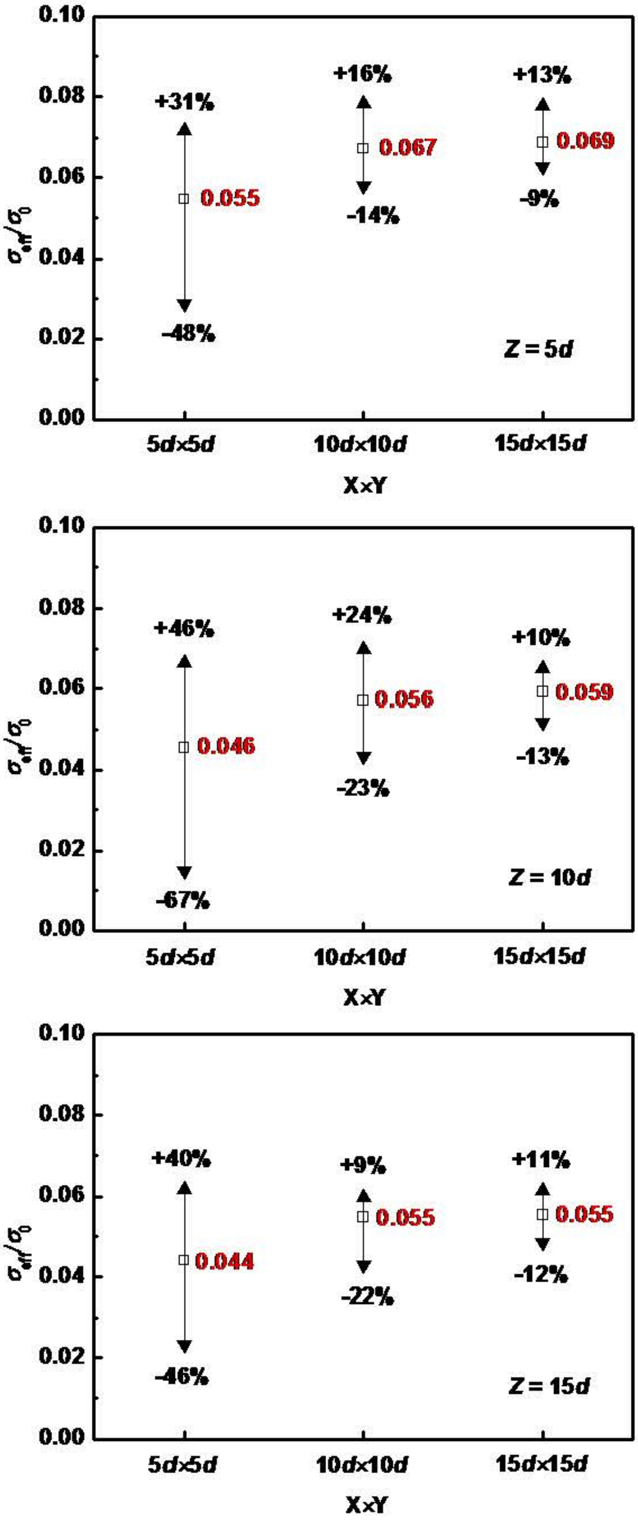

Figure 4.2 σ_{eff}/σ_0 with different computational domain

4.3.2 Effect of porosity and volume fraction

The σ_{eff}/σ_0 of the computed conducting phase with different porosities (ε=0.3, 0.4 and 0.5) and volume fractions (Ψ from 0.3 to 0.7) are calculated and compared with literature results in [64], as shown in Figure 4.3. Due to lack of experimental data, this part can be also regarded as a validation of the present model. It can be seen that, present results are slightly higher than the results in [64]. Such a difference is acceptable and it can be explained by the different particles used in present work (mono-sized particles) and literature model (poly-disperse particle size distributions) [64]. For comparison, it also can be concluded from [64] that the σ_{eff}/σ_0 for mono-sized particles are higher than its value for poly-disperse particles, as shown in Figure 4.4.

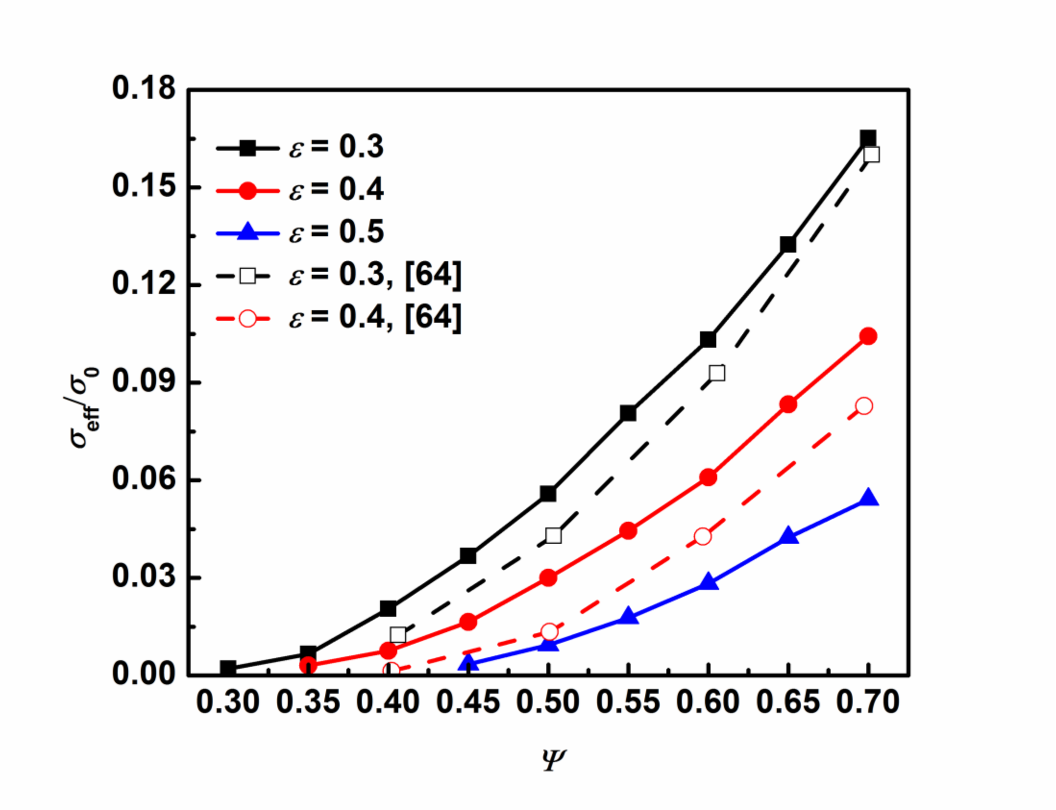

Figure 4.3 Effect of Ψ and ε on σ_{eff}/σ_0

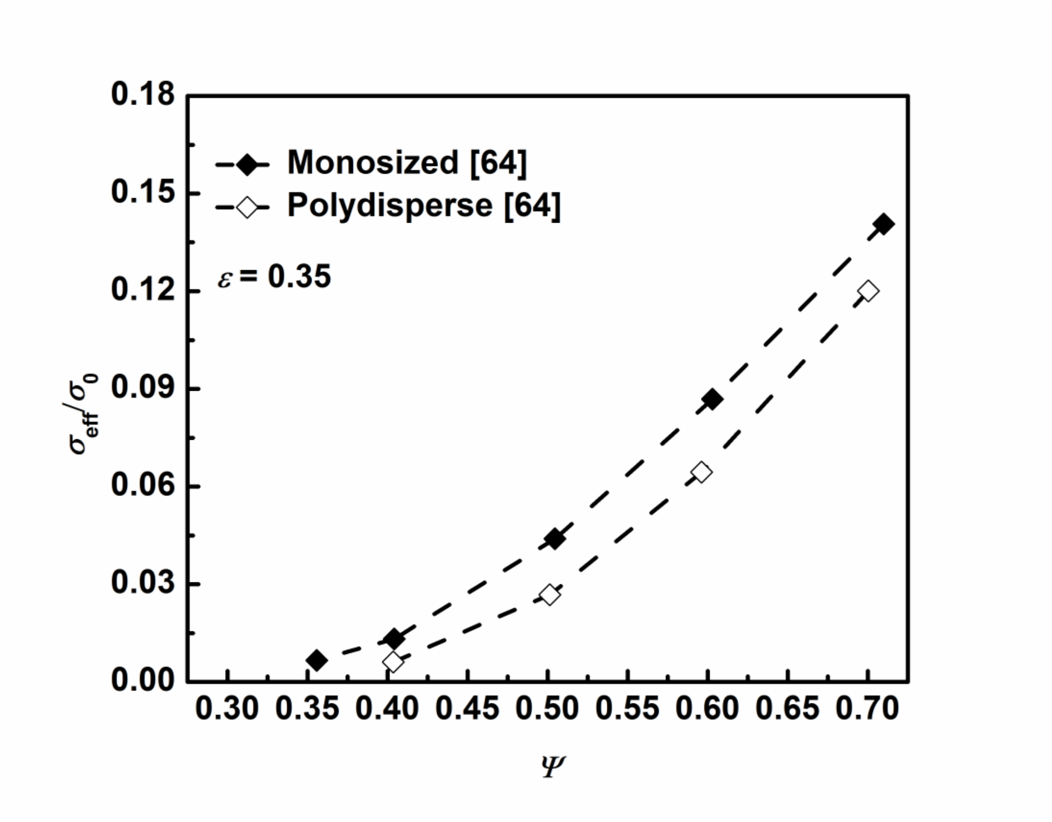

Figure 4.4 Comparison between mono-sized and poly-disperse particles

From Figure 4.3, it can be seen that as the volume fraction (Ψ) increases, the σ_{eff}/σ_0 increases. A relative low porosity (ε) always leads to a higher σ_{eff}/σ_0, when volume fraction Ψ is unchanged. This is easy to understand, because with a lower ε or a larger Ψ, the total volume fraction of the computed conducting phase (*VF*) in the electrode (including the gas phase) is increased, which is supposed to be better for the conduction. If the results in Figure 4.3 are presented as a function of *VF*, it can be found that the σ_{eff}/σ_0 is determined by the *VF*, as shown in Figure 4.5. For the conduction of the computed solid phase, the gas phase and the left solid conducting phases produce the similar insulating effect [118].

The percolation probabilities P_{erco} with different ε and Ψ are also calculated and compared with the percolation model developed by Bertei et al. [71]. When ε is 0.4 and contact angle is 30°, Z_{ave} equals to 6.2 [72]. As shown in Figure 4.6, the simulated results from present model coincide well with the percolation model results. By fitting with the simulated results, the Z_{ave} for porosity 0.3 and 0.5 are 7.5 and 5.2, respectively.

Figure 4.7 shows the P_{erco} as a function of *VF*. It can be seen that P_{erco} is also mainly determined by its *VF*. When the *VF* of the computed conducting phase is about 0.15, a percolated conducting network begins to form. This is in agreement with [71], in which the percolation threshold is 0.17 (when ε=0.55, the Ψ_{perco}=0.38). Until *VF* is around one third, P_{erco} approaches to 1, which means that all the conductive particles belong to the percolated conductive network.

Finally, the σ_{eff}/σ_0 with different ε and Ψ are calculated with the traditional percolation model (Eq. (4.1)). It is found that, the calculated σ_{eff}/σ_0 values are much higher than present numerical results, when the Bruggeman factor μ is assumed as 1.5. By adjusting the μ from 1.5 to 2.7, good agreement between present results and the percolation model results can be achieved, as shown in Figure 4.8.

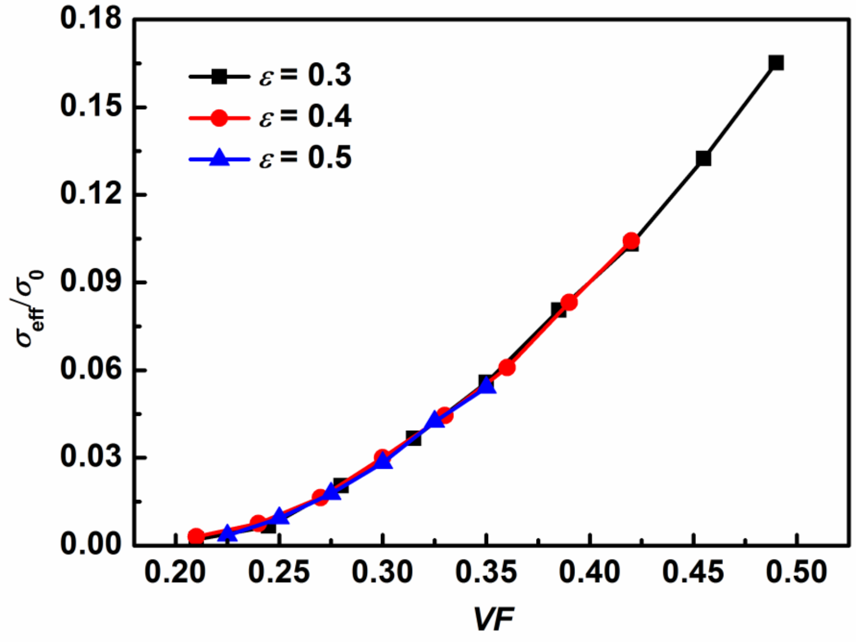

Figure 4.5 Effect of *VF* and ε on σ_{eff}/σ_0

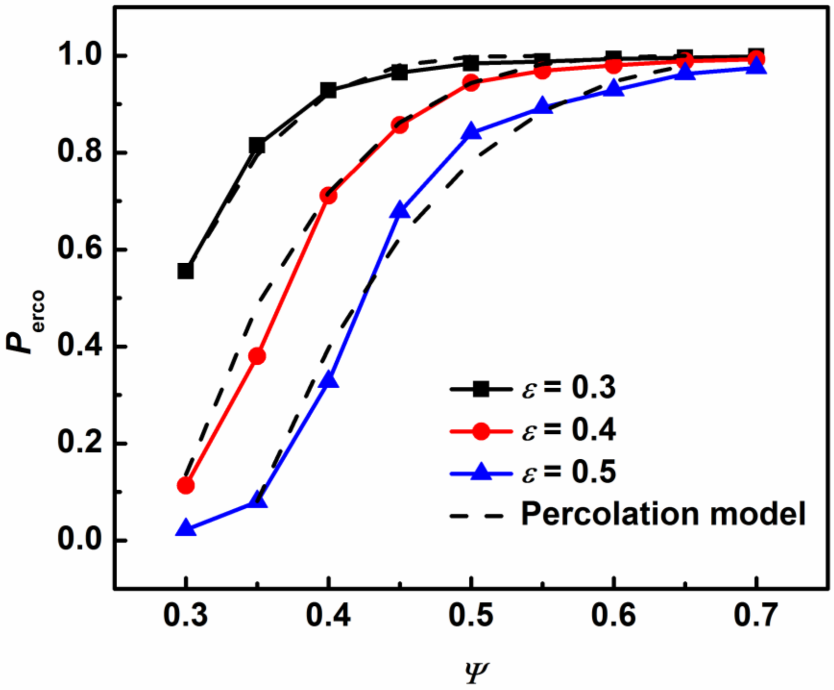

Figure 4.6 Effect of Ψ and ε on P_{erco}

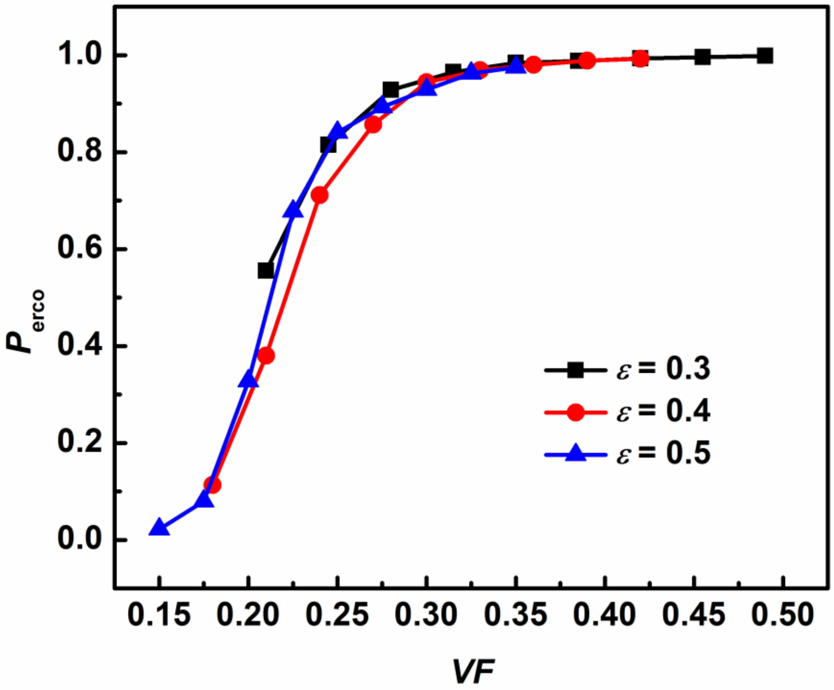

Figure 4.7 Effect of VF and ε on P_{erco}

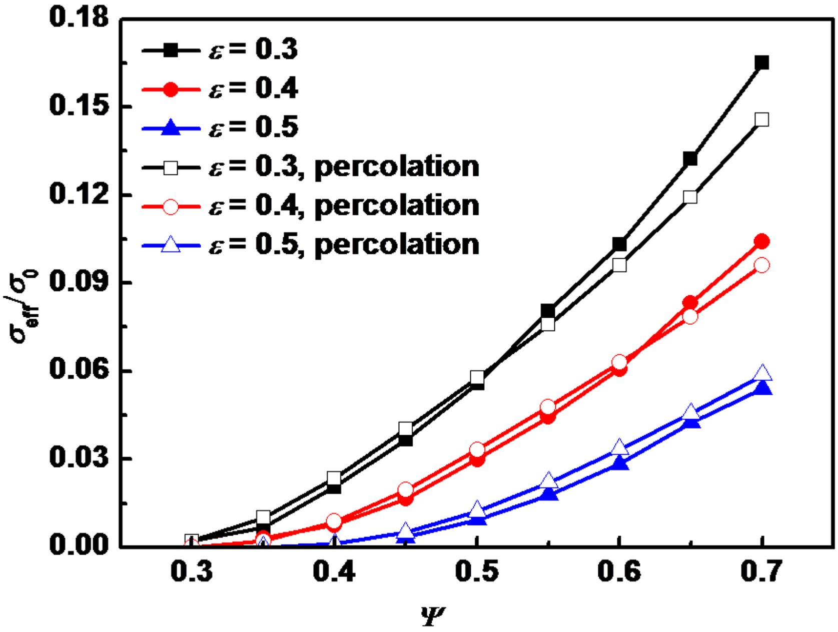

Figure 4.8 Compare the calculated σ_{eff}/σ_0 with percolation model

4.3.3 Effect of particle radius

When fabricate electrode in practice, the electrode particle size may vary from sub-microns to a few microns. To investigate the particle size effect on σ_{eff}/σ_0, the particle radius (r) is changed from 0.25 μm to 1 μm while keeping the porosity ε as 0.3. As shown in Figure 4.9, a higher σ_{eff}/σ_0 can be found in electrodes with large electrode particles. When ε=0.3 and Ψ=0.5, as r increases from 0.25 μm to 1 μm, the σ_{eff}/σ_0 increases from 0.052 to 0.064.

For a better understanding of the particle size effect on σ_{eff}/σ_0, the P_{erco} of the computed conducting phase with different r is also calculated (the particle radius ratio between different conducting phases is kept as 1). As shown in Figure 4.10, for electrodes with typical compositions (0.3<Ψ<0.7), no obvious difference can be found between P_{erco} of different r. Therefore, the better conduction should be attributed to the less tortuous conducting paths formed by the large electrode particles. However, it should be mentioned that small particles are desired to increase the triple-phase boundary (TPB) length [66, 119]. The results indicate that infiltration electrodes with larger ionic-conducting particles as backbone structure coated by nano-sized electronic-conducting particles could well balance the needs for a larger TPB length and a higher ionic conductivity [120-121].

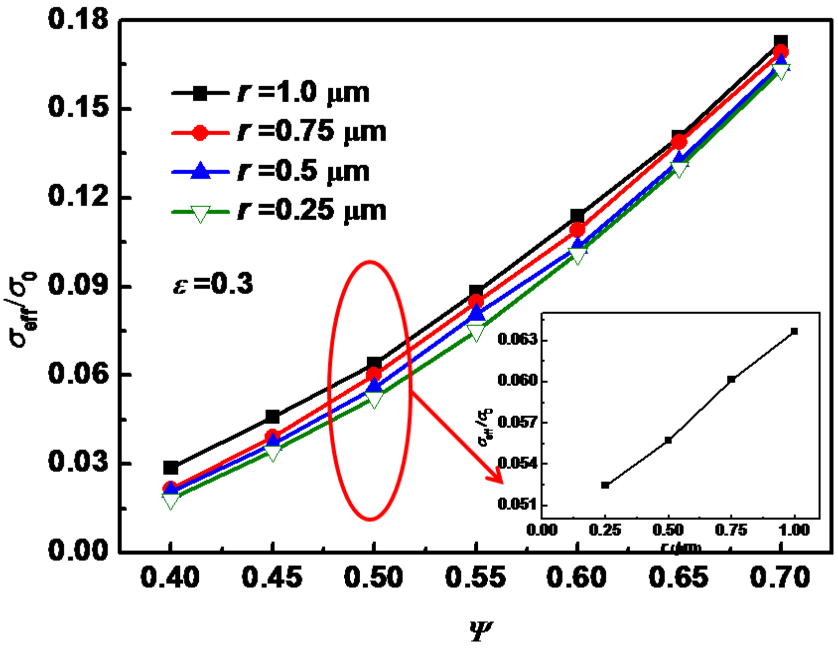

Figure 4.9 Effect of Ψ and r on σ_{eff}/σ_0

4.3.4 Effect of contact angle

Different contact angles (θ) can be generated by controlling the sintering temperature and sintering time [55]. By changing the contact angle θ from about 34^o to 72^o (limited by our calculation procedure), the σ_{eff}/σ_0 is found to increase from 0.057 to about 0.08 (when ε =0.3, Ψ=0.5), as shown in Figure 4.11. This is also attributed to the less tortuous conducting paths formed at larger contact angles since the P_{erco} are found to be almost independent of the contact angle θ, as shown in Figure 4.12. In addition, the TPB length can be also improved with a larger contact angle [66, 72]. The results denote that increasing the contact angle between electrode particles should be a feasible approach to improve the electrode performance.

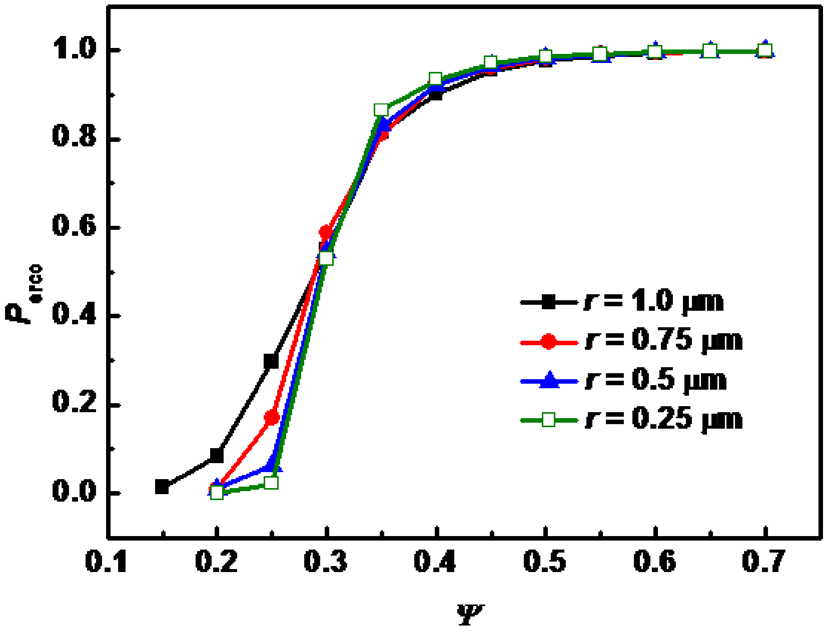

Figure 4.10 Effect of Ψ and r on P_{erco}

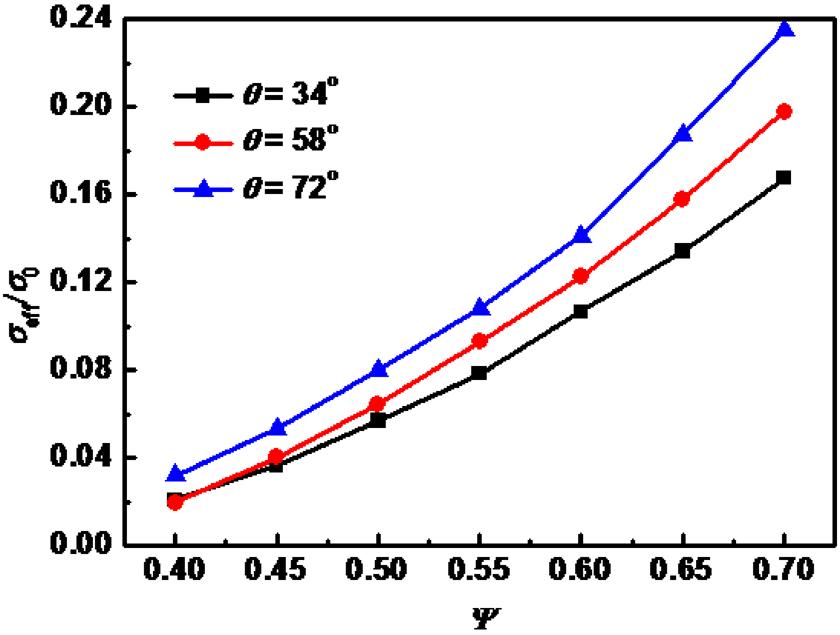

Figure 4.11 Effect of Ψ and θ on σ_{eff}/σ_0

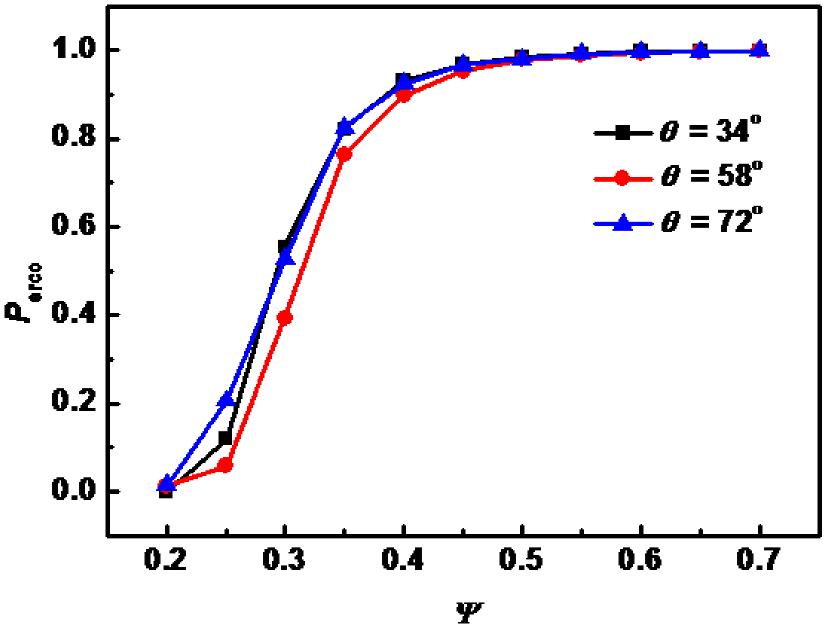

Figure 4.12 Effect of Ψ and θ on P_{erco}

4.4 Conclusions

In this chapter, the relationship between electrode micro parameters (porosity, volume fraction, particle radius and contact angle) and electrode effective conductivity is investigated by numerical modeling. The composite electrode is constructed by random particle packing. The effective conductivity of the computed conducting phase is calculated by solving the steady-state charge conservation equations. Results show that, the effective conductivity of the computed conducting phase is mainly determined by its volume fraction in electrode (including the gas phase). Besides, electrode effective conductivity can be improved by using large electrode particles or large contact angle. Finally, by comparing with the commonly used percolation model for electrode effective conductivity prediction, results in this work suggest an adjustment of the Bruggeman factor in percolation model from 1.5 to 2.7 for a more accurate prediction. The improved percolation model for the calculation of electrode effective conductivity in this chapter, and the previously well validated percolation model [66] for TPB calculation, provide numerical descriptions of the relationship between electrode micro parameters and electrode effective properties. By further incorporating with SOFC macro model describing the relationship between electrode effective properties and cell performance (chapter 5), the whole relationship from electrode micro parameters to SOFC performance can be built.

CHAPTER 5 MULTISCALE MODELING OF SOFC

In this chapter, the relationship between SOFC electrode effective properties and SOFC performance are described by an electrochemical model. By incorporating with electrode micro models describing the relationship between electrode micro parameters and electrode effective properties (chapter 4), the whole relationship between SOFC electrode micro parameters and SOFC cell performance can be built. The combined multi-scale model can be used for electrode design and optimization. As a step towards electrode optimization, the electrochemical active thickness (EAT) in SOFC anode is investigated using the developed multi-scale model (section 5.3) [122].

5.1 Model development

A 1D anode-supported planar type SOFC model is developed in this chapter. The computational domain and boundaries of the developed model is shown in Figure 5.1. The materials used in anode, cathode and electrolyte are Ni/YSZ, LSM/YSZ and YSZ. Hydrogen and air are used as the fuel and oxidant, respectively.

Major assumptions adopted in this model include:

1) Isothermal and steady state conditions;
2) Uniformly distributed and well percolated reaction sites (TPBs) inside the electrodes;
3) Neglect the convection flows and gas pressure gradients effect in electrodes [13, 123-124].

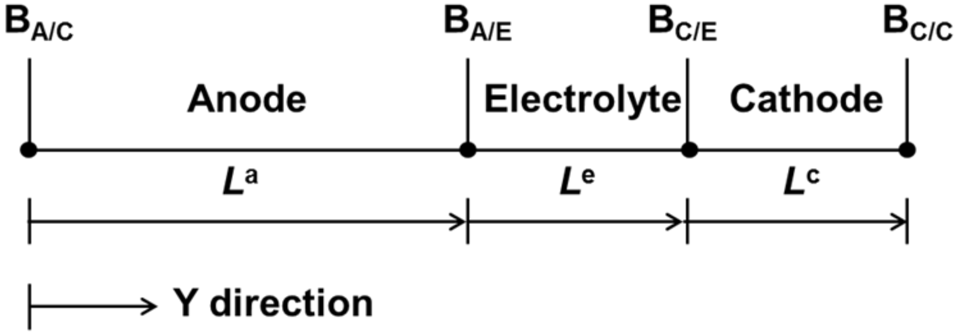

Figure 5.1 Computational domain and boundaries

5.1.1 Electrochemical reaction kinetics

In this model, YSZ is used as the electrolyte material. Therefore, when hydrogen and air are used as the fuel and the oxidant respectively, the electrochemical reactions at the TPBs of the two electrodes are:

Anode:

$$H_2 + O^{2-} \rightarrow H_2O + 2e^- \tag{5.1}$$

Cathode:

$$0.5O_2 + 2e^- \rightarrow O^{2-} \tag{5.2}$$

The relationship between local current densities j_{TPB} (A/m) and local overpotentials η_{local} (V) at the TPBs of anode and cathode can be described by the Bulter-Volmer equations as [77, 92]:

$$j_{TPB}^{a} = j_{ref}^{a}\left(\frac{p_{H2,TPB}}{p_{H2,ref}}\right)\left(\frac{p_{H2O,TPB}}{p_{H2O,ref}}\right)\left\{\exp\left(\frac{F\eta_{local}^{a}}{RT}\right) - \exp\left(\frac{-F\eta_{local}^{a}}{RT}\right)\right\} \tag{5.3}$$

$$j_{TPB}^{c} = j_{ref}^{c}\left(\frac{p_{O2,TPB}}{p_{O2,ref}}\right)^{0.25}\left\{\exp\left(\frac{F\eta_{local}^{c}}{RT}\right) - \exp\left(\frac{-F\eta_{local}^{c}}{RT}\right)\right\} \tag{5.4}$$

where, p_{TPB} is the partial pressure at the TPBs, p_{ref} is the reference partial pressure (equals to 0.968 atm, 0.21 atm and 0.032 atm for H_2, O_2 and H_2O in this study), F, R, and T are the Faraday constant (96485 C/mol), ideal gas constant

(8.314 J/(mol K)) and operating temperature (K). Superscripts *a* and *c* represent anode and cathode, respectively. j_{ref} is the reference exchange current density.

5.1.2 Output voltage

The cell output voltage V_{cell} and related variables are derived as following (more details can be found in [83, 92, 125-126]):

$$V_{cell} = \phi_{el}^{C/C} - \phi_{el}^{A/C} \tag{5.5}$$

$$\eta_{local}^{c} = \phi_{el}^{c} - \phi_{io}^{c} - E_{eq}^{c} \tag{5.6}$$

$$\eta_{local}^{a} = \phi_{el}^{a} - \phi_{io}^{a} - E_{eq}^{a} \tag{5.7}$$

where, ϕ is the electrical potential and E_{eq} is the equilibrium electrical potential difference; subscripts *io* and *el* represent the ion conducting phase and electron conducting phase; superscripts C/C, A/C represent boundaries labeled in Figure 5.1; superscripts *a* and *c* represent the anode and cathode, respectively. The equilibrium electric potential differences are given as:

$$E_{eq}^{a} = 0; \quad E_{eq}^{c} = E_{Nernst} \tag{5.8}$$

$$E_{Nernst} = E_{T} - \frac{RT}{2F}\ln\left(\frac{p_{H2O,TPB}}{p_{H2,TPB}\,p_{O2,TPB}^{0.5}}\right) \qquad 5.9)$$

$$E_{T} = 1.253 - 0.00024516T \tag{5.10}$$

5.1.3 Conservation equations

The conservation equations used to describe the current and mass distributions inside the cell are summarized in Table 5.1. The effective properties of electrodes (λ_{TPB}, σ_{io} and σ_{el}) are calculated using the percolation model developed by Chen et al. [66]. The diffusion process is described by the commonly used dusty gas model.

5.1.4 Boundary conditions

The required boundary conditions to solve the governing equations are listed in Table 5.2. At the inlets, constant gas compositions ($p_{\mathrm{H2,inlet}}$, $p_{\mathrm{H2O,inet}}$, and $p_{\mathrm{O2,inlet}}$) are set for the anode/channel ($B_{\mathrm{A/C}}$) and cathode/channel ($B_{\mathrm{C/C}}$) interfaces. Mass fluxes in $B_{\mathrm{A/C}}$ and $B_{\mathrm{C/C}}$ are determined by the total current density j. Pure ionic current flux is set at $B_{\mathrm{A/E}}$ and $B_{\mathrm{C/E}}$. Pure electronic current flux is set at $B_{\mathrm{A/C}}$ and $B_{\mathrm{C/C}}$.

The conservation equations are solved using the commercial software COMSOL®. Grid independence is achieved by refining the grids in the computational domain. The output voltage is given as the known condition so that the current density distribution in the cell and the gas distribution in the electrodes can be obtained.

Table 5.1 Conservation equations [92, 122]

Anode	charge	$\frac{dj_{el}^a}{dy} = -\frac{dj_{io}^a}{dy} = -\sigma_{el}^a \frac{d^2\phi_{el}^a}{dy^2} = -j_{TPB}^a \lambda_{TPB}^a$
	mass	$\frac{dN_{H2}}{dy} = -\frac{dN_{H2O}}{dy} = -\frac{j_{TPB}^a \lambda_{TPB}^a}{2F}$
Cathode	charge	$\frac{dj_{el}^c}{dy} = -\frac{dj_{io}^c}{dy} = -\sigma_{el}^c \frac{d^2\phi_{el}^c}{dy^2} = j_{TPB}^c \lambda_{TPB}^c$
	mass	$\frac{dN_{O2}}{dy} = -\frac{j_{TPB}^c \lambda_{TPB}^c}{4F}$
Electrolyte	charge	$\frac{dj_{io}}{dy} = -\sigma_{io} \frac{d^2\phi_{io}}{dy^2} = 0$

Table 5.2 Boundary conditions [122]

	$B_{A/C}$	$B_{A/E}$	$B_{C/E}$	$B_{C/C}$
Ionic charge balance	$\overrightarrow{j_{io}^{a}}\cdot\vec{n}=0$	$\overrightarrow{j_{io}^{a}}\cdot\vec{n}=j$	$\overrightarrow{j_{io}^{c}}\cdot\vec{n}=j$	$\overrightarrow{j_{io}^{c}}\cdot\vec{n}=0$
Electronic charge balance	0	$\overrightarrow{j_{el}^{a}}\cdot\vec{n}=0$	$\overrightarrow{j_{el}^{c}}\cdot\vec{n}=0$	V_{cell}
Mass balance	$p_{\mathrm{H2,inlet}}$ $p_{\mathrm{H2O,inlet}}$	$\overrightarrow{N_{H2}}\cdot\vec{n}=0$ $\overrightarrow{-N_{H2O}}\cdot\vec{n}=0$	$\overrightarrow{N_{O2}}\cdot\vec{n}=0$ $\overrightarrow{N_{N2}}\cdot\vec{n}=0$	$p_{\mathrm{O2,inlet}}$

5.2 Model validation

Validation of the model is conducted by comparing the cell performance with experimental results in [27], as shown in Figure 5.2. The basic parameters used for model validation can be found in Table 5.3. The reference exchange current density (j_{ref}) is obtained by fitting with the experimental data. It can be seen that the simulated cell performance using the present model coincides well with the measured results in [27].

5.3 Electrochemical active thickness (EAT)

5.3.1 Introduction to EAT

It is well known that, in composite SOFC electrodes, electrochemical reactions only occur at the intersection places where the gas phase, ion-conducting phase and electron-conducting phase meet, namely the triple phase boundaries (TPBs) [91-92]. However, not all the TPBs are active in working conditions. It is commonly recognized that only TPBs in a very narrow zone near the electrode/electrolyte (E/E) interface are active in typical SOFC operating conditions. The thickness of the electrochemical active zone is called as the electrochemical active thickness (EAT) [122].

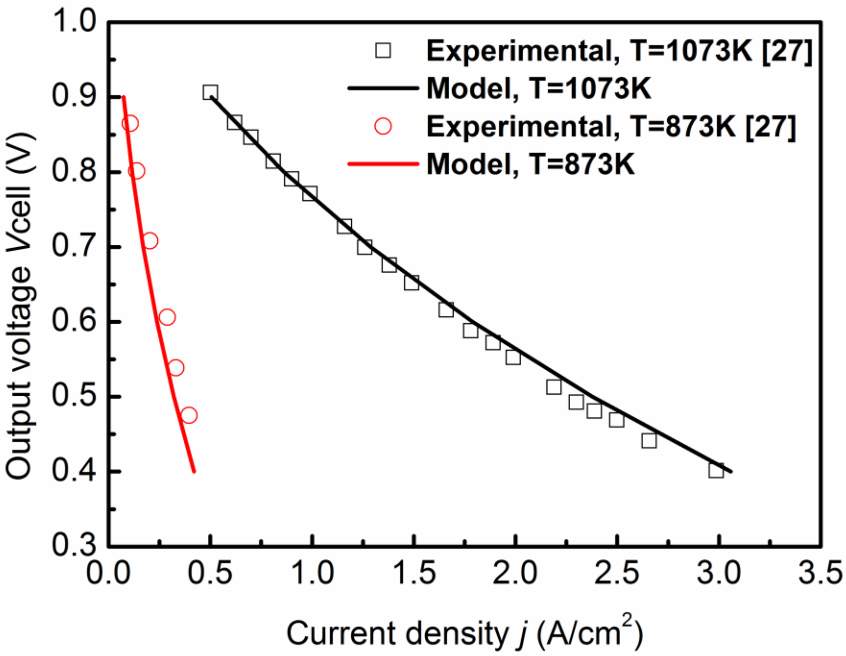

Figure 5.2 Comparison between experimental data and model results

EAT is of paramount importance in determining the optimum electrode thickness [127]. An electrode with thickness much larger than the EAT will bring about increased concentration losses due to the insufficient gas transportation while a thinner thickness will lead to reduced active TPBs and consequently degrade the cell performance. Besides, the EAT could also provide useful guidance for the development of the functionally graded electrode [34], where the electrode are purposely designed in different zones according to their functions.

Table 5.3 Basic Parameters for performance analysis [122]

Operating temperature, T	1073K
Operating pressure, p	101325 Pa
Inlet gas composition (molar fraction):	
Anode, $x_{\mathrm{H2}} + x_{\mathrm{H2O}}$	96.8% H_2+3.2% H_2O [83]
Cathode, $x_{\mathrm{O2}} + x_{\mathrm{N2}}$	21% O_2+79% N_2
Structure parameter:	
Thickness, $L^a/L^e/L^c$ (for model validation)	400 μm /50 μm /50 μm (1000 μm /8 μm /20 μm)
Porosity, $\varepsilon^a \& \varepsilon^c$ (for model validation)	0.4 & 0.4 (0.48 & 0.26) [27]
Tortuosity factor, $\xi^a \& \xi^c$	3
Mean particle radius, $r_{el} \& r_{io}$	0.5 μm
Volume fraction of ionic phase, $\psi_{io}^a \& \psi_{io}^c$ (for model validation)	0.5 & 0.5 (0.33 & 0.67) [27]
YSZ conductivity	$\sigma_{YSZ}^0 = 3.34\times10^4 \exp(-\frac{10300}{T})$ [128]
Ni conductivity	$\sigma_{Ni}^0 = 3.27\times10^6 - 1065.3T$ [129]
LSM conductivity	$\sigma_{LSM}^0 = \frac{8.85\times10^7}{T}\exp(\frac{1082.5}{T})$ [130]

By now, numerous studies can be found about the determination of EAT. However, the reported values (from 13 μm [89] to 253 μm [94] for cathode and from 5 μm [80] to 160 μm [83] for anode) are quite different, probably due to the different experimental or calculation conditions used in their studies. Besides, it is commonly regarded that EAT is limited by the poor ionic conductivity of the electrode and thus increasing the temperature can enlarge the EAT due to the increased ionic conductivity, which is in agreement with results in [9, 45, 60]. However, opposite trend is found in [94] where EAT decreases from 126 μm to 36 μm with temperature increasing from 923K to 1073K. In addition, a decreased EAT is found in [60] when a lower concentration H_2 is used as fuel. The underlying reason for this phenomenon is also unclear. Therefore, a better understanding of the relationship between EAT and its affecting parameters is still required.

5.3.2 EAT in SOFC anode

In this section, the EAT in SOFC anode is numerically investigated based on the 1D model developed above. The basic parameters used for parametric analysis can be found in Table 5.3. The EAT in SOFC anode is defined as the zone thickness in which 99% ionic current is changed into electronic current [122], as labeled in Figure 5.3.

5.3.2.1 Effects of operating parameters

The operating parameters affecting EAT mainly include: the output voltage (V_{cell}), the operating temperature (T), and the inlet gas composition.

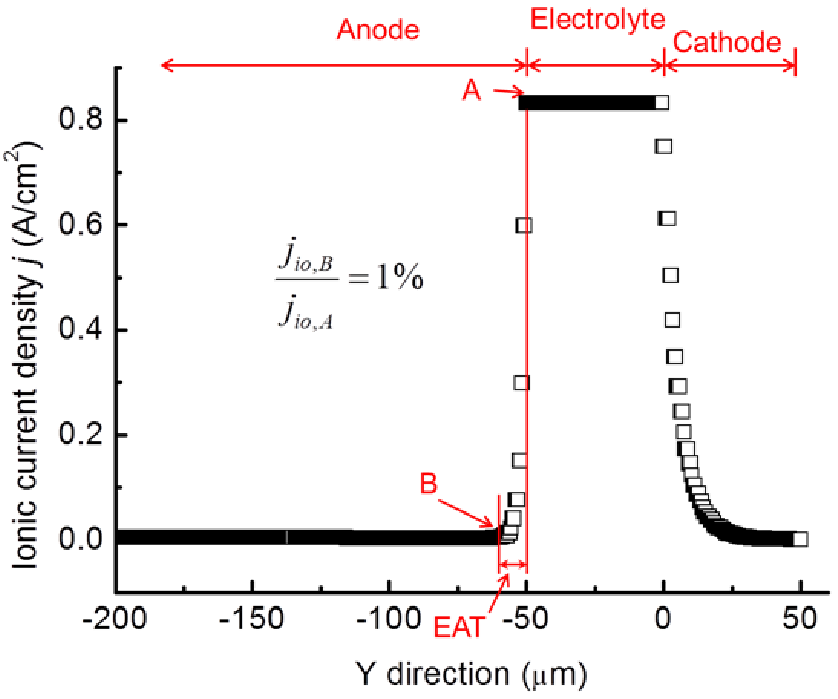

Figure 5.3 Distribution of the ionic current density j_{io} in a typical SOFC

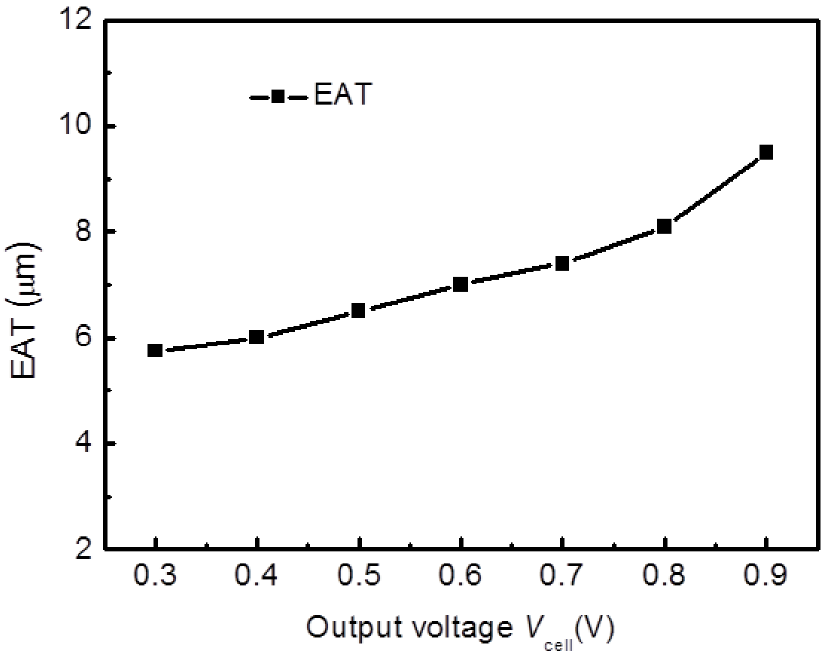

Figure 5.4 Effect of output voltage V_{cell}

The effect of output voltage V_{cell} on EAT is shown in Figure 5.4. It can be seen that as the output voltage increases, the EAT value increases. However, the EAT values are always less than 10 μm which is thinner than the typical electrode interlayer thickness (commonly about 20μm [27]). For comparison, it is also found in [92, 127] that high output voltage leads to a larger EAT. However, [45] concluded that the output voltage only had a negligible effect on EAT. In the following part, analysis are conducted only with output voltage V_{cell}=0.8 V and V_{cell}=0.5 V considering SOFC actual operating range.

Figure 5.5 shows the effect of H_2 inlet concentration ($x_{H2,inlet}$) on EAT. It can be found that a larger EAT value can be obtained with a higher H_2 concentration, which is in agreement with findings in [60]. Since the H_2 concentration decreases along the gas channel, it can be deduced that at the downstream part of SOFC, the EAT value should be lower than that in the upstream part.

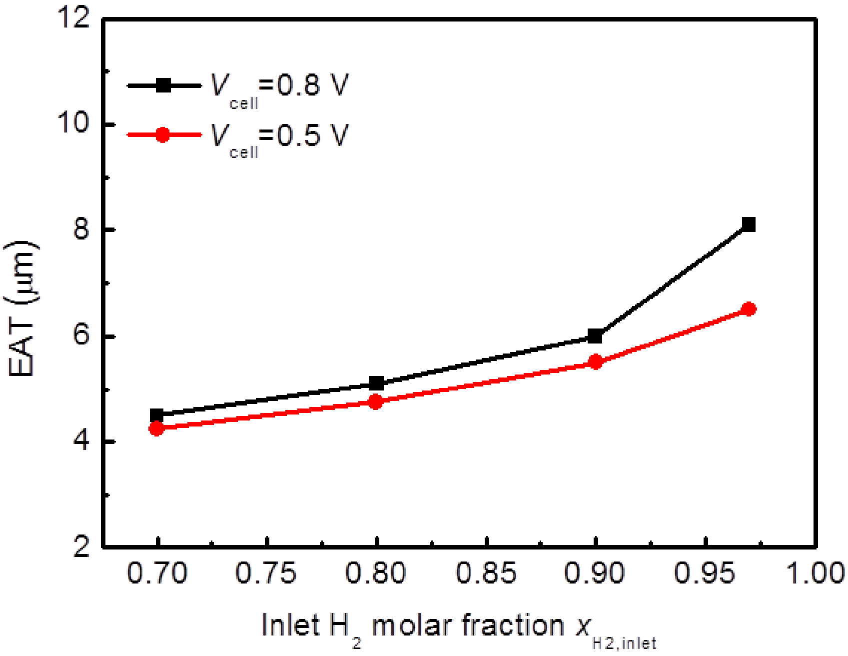

Figure 5.5 Effect of inlet H_2 molar fraction $x_{H2,inlet}$

Operating temperature T has a complex effect on SOFC performance. It not only affects the electrochemical reaction rates in TPBs, but also affects the effective conductivities in electrolyte as well as electrodes. As shown in Figure

5.6, as the operating temperature increases from 873K to 1173K, the EAT decreases. However, the decreasing rate of EAT with V_{cell}=0.8 V is not so obvious compared with V_{cell}=0.5 V. For comparison, [94] found similar trends but [45, 80-81, 92] reported a negative relationship between EAT and operating temperature T.

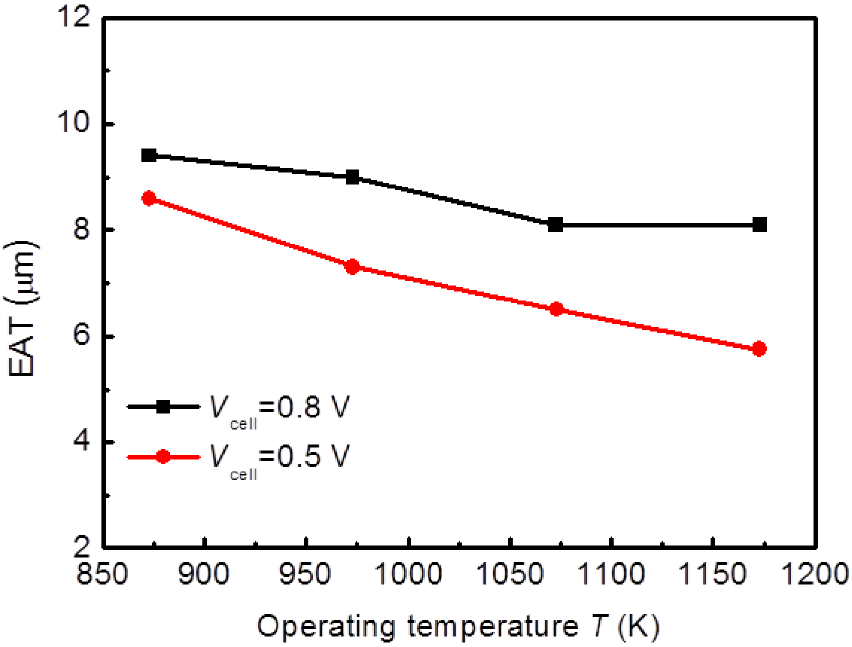

Figure 5.6 Effect of operating temperature T

5.3.2.2 Effects of different material properties

When different catalyst materials are used, different reaction rates (reference exchange current densities, j_{ref}) can be achieved. The effect of j_{ref} on EAT is shown in Figure 5.7. By increasing j_{ref} from $0.1j_{\mathrm{ref\_standard}}$ to $2j_{\mathrm{ref\_standard}}$ ($j_{\mathrm{ref\_standard}}$ refers to the j_{ref} fitted from experimental data in [27]), the corresponding EAT decreases from nearly 30 μm to about 5μm, which is consistent with the result trends in [92]. Since the TPB density in unit volume (λ_{TPB}) affects SOFC performance in the same way with j_{ref}, the negative relationship between λ_{TPB} and EAT can be deduced.

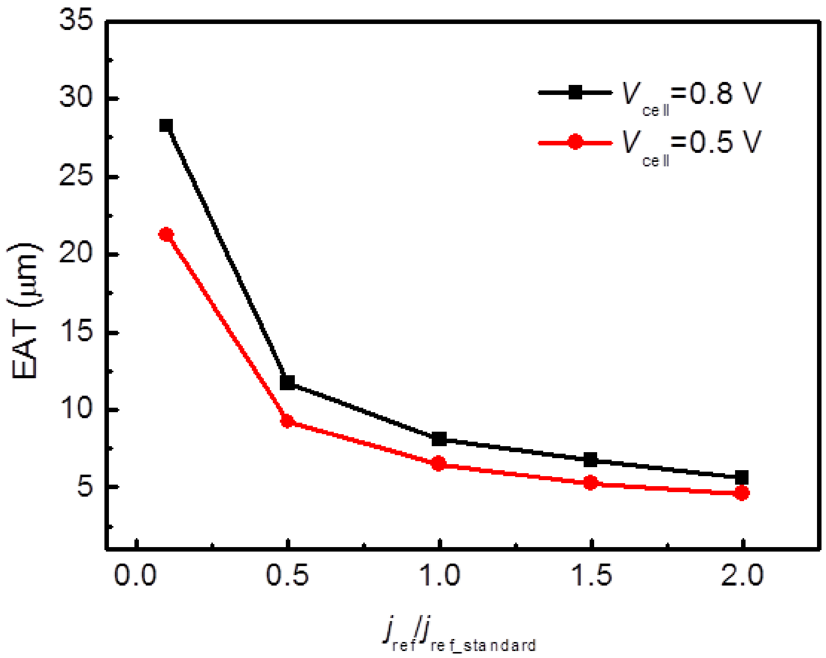

Figure 5.7 Effect of reference exchange current density j_{ref}

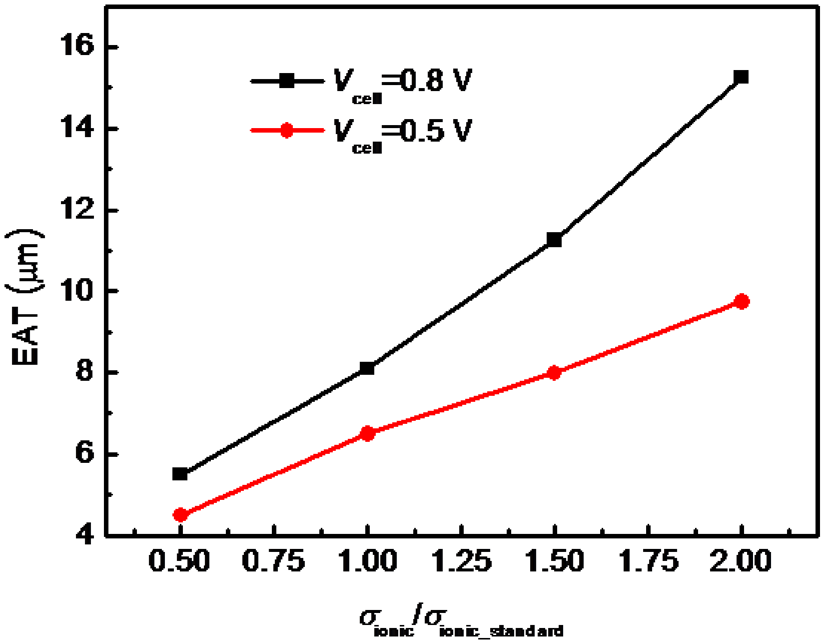

Figure 5.8 Effect of ionic conductivity σ_{io}

Similarly, different effective ionic conductivity (σ_{io}) can be obtained by using different ion-conducting materials. By increasing the σ_{io} from $0.5\sigma_{io\_standard}$ to $2\sigma_{io\_standard}$ (The σ_{io} of YSZ is defined as the $\sigma_{io\_standard}$), the EAT is found to increase from 5.5 µm to 15.25 µm when the output voltage is 0.8V, as shown in Figure 5.8. Similar trends can be seen in [94].

5.3.2.3 Effects of structure parameters

The microstructure parameters affecting electrode performance mainly include: the mean particle radius (r), the particle radius ratio (r_{io}/r_{el}) and the porosity (ε). The effect of r on EAT can be found in Figure 5.9. It can be seen that as r increases from 0.5 µm to 2 µm, the EAT value increases greatly from 3.75 µm to 18 µm when V_{cell}=0.8 V, as reported in [81, 89, 92]. However, it should be noted that, as the particle size increases, the cell performance decreases significantly due to the reduced TPBs [83].

The effect of r_{io}/r_{el} on EAT is shown in Figure 5.10. By keeping the particle radius of the electron-conducting phase (r_{el}) to constant (0.5µm) and changing the particle radius of ion-conducting phase (r_{io}) from 0.25 µm to 1 µm, the EAT value increases slightly. However, it is indicated by [92] that the effect of r_{io}/r_{el} on EAT depends on the resulted relative variations of σ_{io} and λ_{TPB}.

The EAT values in electrodes with different porosities (ε) are shown in Figure 5.11. A larger ε decreases the TPBs and effective conductivities but facilitates the gas transport in electrodes simultaneously. A larger EAT is found in electrode with higher porosity in [92] while only negligible effect of ε on EAT is found in present study, as shown in Figure 5.11.

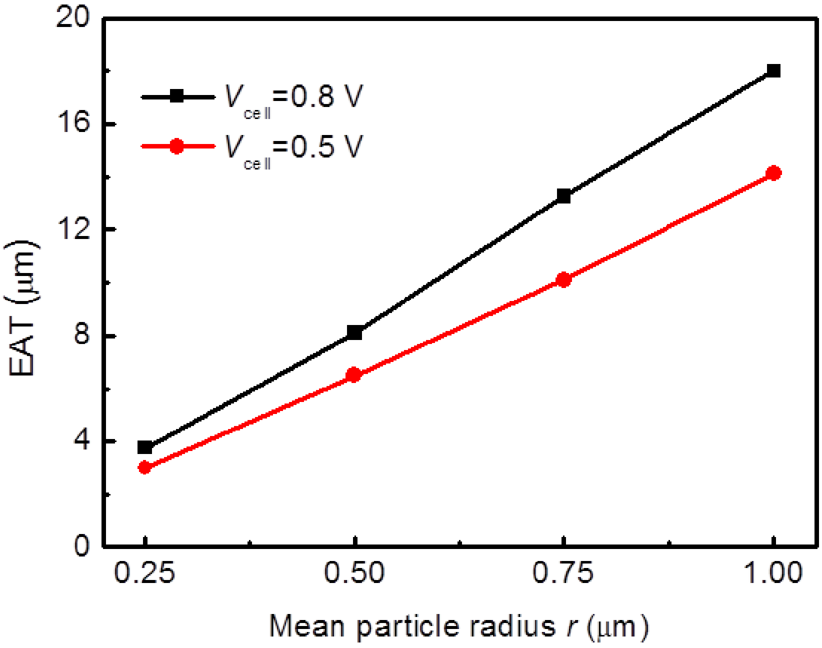

Figure 5.9 Effect of particle radius r

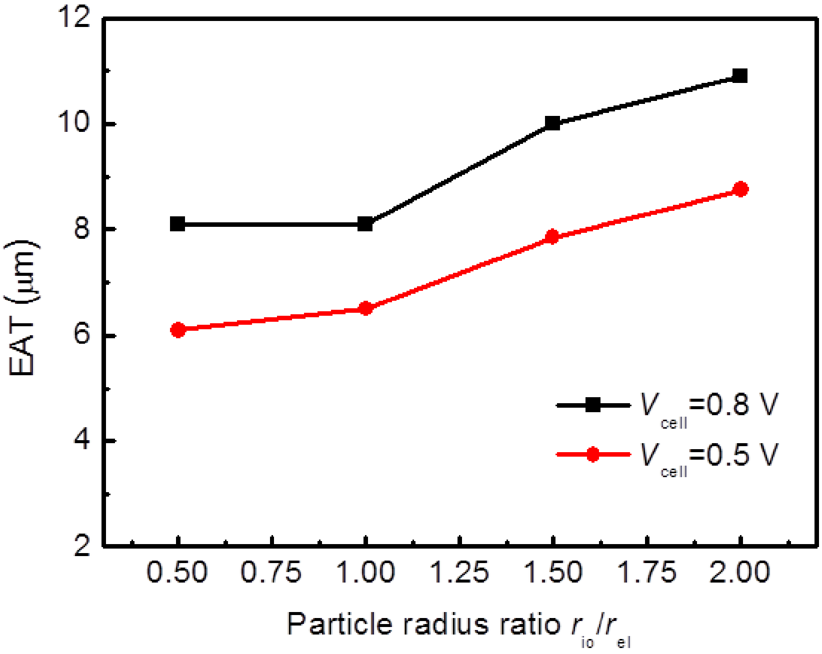

Figure 5.10 Effect of particle radius ratio r_{io}/r_{el}

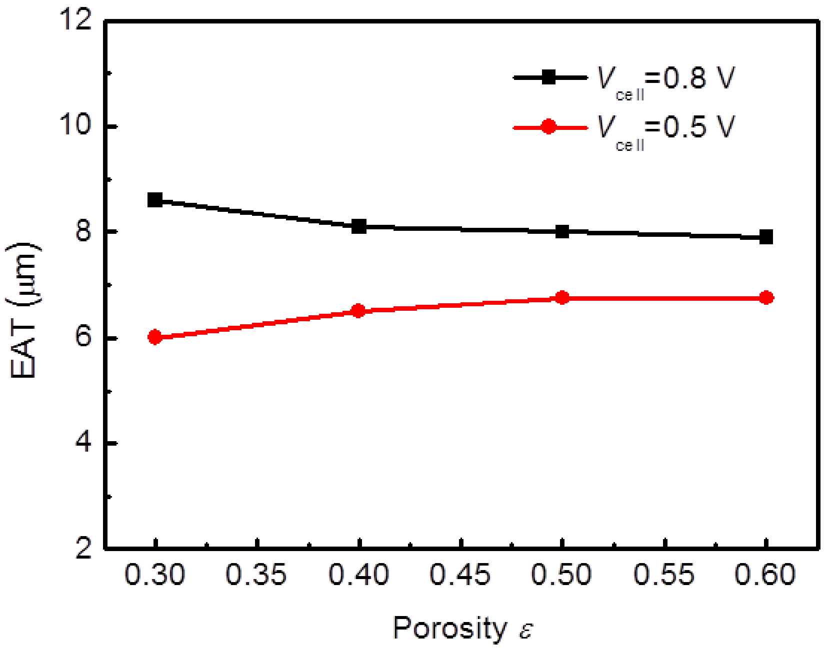

Figure 5.11 Effect of porosity ε

5.3.3 Theoretical analysis on EAT

In section 5.3.2, the effects of different factors on EAT is investigated numerically. However, comparing with literature results, effect of some factors (e.g. the operating temperature T) on EAT is still conflicting. Therefore, in this section, the effects of various parameters on EAT is analyzed from another point of view, aiming to have a more clear understanding about the relationship between EAT and its affecting parameters.

The analysis begins from the electrode performance and its major losses. Take SOFC anode as an example, to produce electronic current j_y (or consume the same amount of ionic current) in an optional position y in SOFC anode, the related losses include (as illustrated in Figure 5.12):

1) Activation loss (R_{act}) caused by the local electrochemical reactions.

2) Ohmic loss (R_{ohmic}) caused by the ion transport from the anode/electrolyte

interface ($B_{A/E}$) to position y and the electron transport from position y to the anode/gas channel interface ($B_{A/C}$).

3) Concentration loss (R_{con}) caused by the different gas compositions in position y and reference conditions.

As the local electrochemical reaction rates are also affected by the local gas distributions, the R_{con} and R_{act} can be combined into a $R_{act,con}$. Therefore, the total voltage loss to generate j_y in position y is ($R_{act,con}$+ R_{ohmic}), which determines the possibility that the electrochemical reactions occur in position y. In other words, for any two positions $y1$ and $y2$ in the SOFC anode, to generate equivalent electronic current, if the ($R_{act,con,y1}$+$R_{ohmic,y1}$) is less than ($R_{act,con,y2}$+$R_{ohmic,y2}$), electrochemical reactions are more likely to occur in position $y1$.

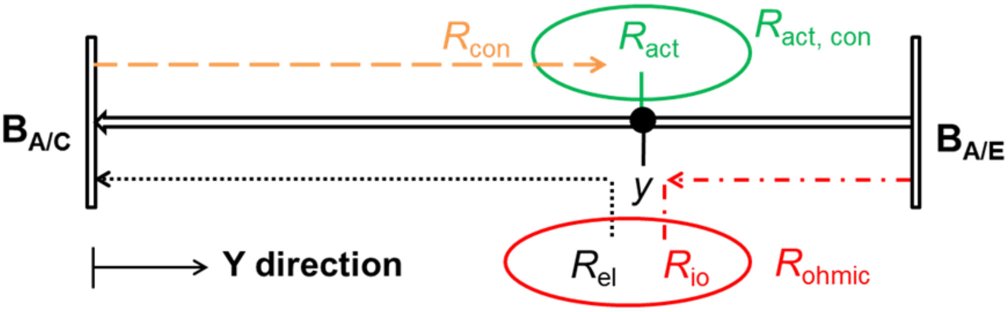

Figure 5.12 Diagram of various losses in SOFC anode

Based on the above analysis, two extreme cases are considered:

1) R_{ohmic} is the dominant loss and $R_{act,con}$ is negligible. Since the electron conductivity is several orders of magnitude higher than the oxygen ion conductivity in the typical SOFC composite electrodes, the ohmic loss caused by the electron transport can be neglected. Therefore, R_{ohmic} is mainly determined by the ion transport and is in inverse proportion to the ion transport distance, i.e. the closer to the anode/electrolyte interface ($B_{A/E}$), the more likely the electrochemical reactions occur.

2) $R_{act,con}$ is the dominant loss and R_{ohmic} is negligible. The gas distribution

effect is not significant in typical SOFC operating conditions. Therefore, in most cases, the activation loss associated with the local electrochemical reactions can be regarded to be independent of its location, which means electrochemical reactions should occur uniformly throughout the electrode when TPBs are well percolated and homogeneously distributed.

Therefore, it can be concluded that the EAT value mainly depends on the ratio of $R_{\mathrm{act,con}}/R_{\mathrm{ohmic}}$ in typical SOFC composite electrodes. When the gas distribution effect is ignorable, a larger ratio means a more even distribution of the electrochemical reactions in the electrode and thus a thicker EAT while a smaller ratio drives the electrochemical reactions to the electrolyte and thus leads to a thinner EAT.

Explanation of results in section 5.3.2:

From the above analysis, it is easy to find that increased exchange current density j_{ref} (Figure 5.7) and TPB length λ_{TPB} will bring about thinner EATs by decreasing the $R_{\mathrm{act,con}}$, while higher ionic conductivity σ_{io} (Figure 5.8) will lead to a thicker EAT by decreasing the R_{ohmic}.

As the output voltage V_{cell} decreases from 0.9 to 0.3, the dominant loss of the SOFC actual performance changes from the activation loss to the ohmic loss, which leads to a decreased ratio of $R_{\mathrm{act,con}}/R_{\mathrm{ohmic}}$ and a thinner EAT, as shown in Figure 5.4. But it should be noted that different conclusion might exist when concentration loss is dominant.

Higher inlet hydrogen molar fraction $x_{\mathrm{H2,inlet}}$ causes a lower reaction rate in anode (see Eq. (5.3)) and thus results in a larger ratio of $R_{\mathrm{act,con}}/R_{\mathrm{ohmic}}$ and a thicker EAT, as shown in Figure 5.5. However, it should be mentioned that higher inlet oxygen molar fraction $x_{\mathrm{O2,inlet}}$ improves the electrochemical reaction in the cathode side and indicates a thinner EAT.

Decreasing of the operating temperature T reduces the reaction rate and effective conductivity simultaneously. Therefore, the effect of operating temperature on EAT depends on the resulted variation in $R_{act,con}/R_{ohmic}$. Moreover, variations in mean particle radius r, particle radius ratio r_{io}/r_{el}, porosity and volume fraction of electron conducting phase Ψ_{el} also affect the $R_{act,con}$ and R_{ohmic} at the same time. Consequently, their effects on EAT require further study for a detailed cell.

5.3.4 Conclusion on EAT

In this work, the electrochemical active thickness (EAT) in SOFC anode is investigated. The effects of various parameters on EAT are examined both numerically and theoretically. Theoretical analysis results show that the EAT values highly depend on the ratio of the concentration related activation loss $R_{act,con}$ to the ohmic loss R_{ohmic}. A larger ratio leads to a thicker EAT.

Although the work is conducted for EAT in SOFC anode, the positive relation between the EAT and the ratio $R_{act,con}/R_{ohmic}$ can be generalized to SOFC cathode. As the electrochemical reaction rates in SOFC cathode are usually lower than those in anode, it can be deduced that the EAT value in the cathode will be larger than that in the anode, when the same electrode structures and ion-conducting materials are used. For the cell defined in Table 5.3, the EAT in anode and cathode are about 10 μm and 25μm, respectively, coincides with our above prediction. Besides, a positive correlation is found between the H_2 concentration and the EAT in anode, because a high H_2 concentration leads to a lower reaction rate and thus a larger $R_{act,con}$. However, for SOFC cathode, a higher O_2 concentration will lead to a higher reaction rate and a smaller $R_{act,con}$, therefore, a negative relationship between EAT and SOFC cathode can be deduced. Furthermore, the concentrations of H_2 and O_2 decrease along the gas channels, therefore, in the downstream part of SOFC anode, the EAT value should be smaller than that in the anode inlet. Reversely, the EAT value in the downstream part of SOFC cathode should be larger than that in the cathode inlet. This provides theoretical basis for optimizing the electrode thickness along the gas main flow direction.

Fuel flexibility is one of the advantages of SOFC. When CO is used as fuel, the EAT values is predicted to be larger than those in situations with H_2 (under typical operating voltages), due to the much lower reaction rates of carbon fuel compared with that of H_2. When CH_4 is used as fuel, anode provides reaction sites not only for electrochemical reactions but also for steam reforming reaction, therefore, the EAT value may also be larger than that in the pure H_2 situation.

5.4 Conclusion

In this chapter, the relationship between SOFC electrode effective properties and SOFC performance is described by an electrochemical model (section 5.1). By incorporating with electrode micro models describing the relationship between electrode micro parameters and electrode effective properties (chapter 4), the multi-scale model describing the whole relationship between SOFC electrode micro parameters and SOFC cell performance is be built (section 5.1 & 5.2). The combined multi-scale model can be used for electrode design and optimization.

In section 5.3, the electrochemical active thickness (EAT) of SOFC anode is calculated based on the developed multi-scale model. For typical conditions, the

EAT values in SOFC anode are about 10 μm. For a better understanding of the relationship between EAT and its affecting parameters, theoretical analysis about the electrode performance and its main losses is conducted, from which we conclude that the EAT is mainly determined by a ratio: $R_{\mathrm{act,con}}/R_{\mathrm{ohmic}}$.

CONCLUSIONS

As a new kind of power generation device, SOFC has attracted much attention for its high efficiency, environmental friendly property and fuel flexibility. By now, one major limitation for SOFC commercialization is its high cost, which can be lowered down either by reducing SOFC operating temperature or improving SOFC performance. This work investigates SOFC by numerical modeling aiming at improving SOFC performance. The whole work consists of 2 parts: chapter 2 and chapter 3 focus on SOFC electrolyte, while chapter 4 and chapter 5 focus on SOFC electrode.

Chapter 2 and chapter 3 investigate SOFC with co-ionic conducting electrolyte (co-ionic SOFC). Comparing with traditional SOFC with pure ion conducting electrolyte (O-SOFC and H-SOFC), it is found that co-ionic SOFC can achieve better performance than H-SOFC and O-SOFC by chosen an appropriate proton transfer number (t_H) value. Besides, syngas mixture is superior to hydrogen when used as fuel in co-ionic SOFC. The results provide theoretical basis to improve co-ionic SOFC performance by adjusting the proton transfer number in electrolyte. Since it is also stated that carbon deposition in SOFC anode can be alleviated by the co-ionic property, more detailed modeling studies can be conducted in future to further investigate the performance of co-ionic SOFC using hydrocarbon fuels (such as CH_4), considering the carbon deposition effect in SOFC anode.

SOFC performance can be also improved by optimizing SOFC electrodes, which relies on a clear understanding of the relationship between SOFC electrode micro parameters and SOFC cell performance. In chapter 4, the relationship between electrode micro parameters and electrode effective properties is investigated and finally described using an improved percolation model, while in chapter 5, the relationship between electrode effective properties and SOFC performance is described with an electrochemical model. By combining the two models together, the whole relationship between electrode micro parameters and SOFC performance can be built. The combined multi-scale model can be used for SOFC electrode design and optimization.

As a first step of optimizing SOFC electrodes to improve SOFC cell performance, the electrochemical active thickness (EAT) in SOFC anode is analyzed using the developed multi-scale model. From the results, a positive relation between the EAT and the ratio $R_{\mathrm{act,con}}/R_{\mathrm{ohmic}}$ is summarized. This provides theoretical guide on how to optimize SOFC electrode thickness. For example, for SOFC cathode, a higher O_2 concentration will lead to a higher reaction rate and a smaller $R_{\mathrm{act,con}}$, therefore, in the downstream part of SOFC cathode, the electrode active thickness should be larger than its value in cathode inlet. In addition, CO can be also electrochemically oxidized in SOFC. When CO is used as fuel, the electrode active thickness should be larger than those in SOFC fed with pure H_2 (under typical operating voltages when concentration loss can be neglected), due to the much lower reaction rates of CO compared with that of H_2.

REFERENCES

1. Chu, S. and A. Majumdar, *Opportunities and challenges for a sustainable energy future*. Nature, 2012. **488**(7411): p. 294-303.
2. *World Energy Outlook 2011*, I.E. Agency, Editor. 2011. p. 546-547.
3. O'Hayre, R., et al., *Fuel Cell Fundamentals*. 2006: Wiley.
4. Appleby, A.J., *Fuel cell handbook*. 1988.
5. Larminie, J. and A. Dicks, *Fuel Cell Systems Explained* 2003: wiley.
6. Wang, X., *Dual-ion Conducting Nanocompoiste for Low Temperature Solid Oxide Fuel Cell*, in *School of Information and Communication Technology (ICT)*. 2012, KTH Royal Institute of Technology.
7. Ni, M., M.K.H. Leung, and D.Y.C. Leung, *Parametric study of solid oxide fuel cell performance*. Energy Conversion and Management, 2007. **48**(5): p. 1525-1535.
8. Andersson, M., et al., *Three dimensional modeling of an solid oxide fuel cell coupling charge transfer phenomena with transport processes and heat generation*. Electrochimica Acta, 2013. **109**: p. 881-893.
9. Andersson, M., J. Yuan, and B. Sundén, *SOFC modeling considering electrochemical reactions at the active three phase boundaries*. International Journal of Heat and Mass Transfer, 2012. **55**(4): p. 773-788.
10. Ni, M., D.Y.C. Leung, and M.K.H. Leung, *Modeling of methane fed solid oxide fuel cells: Comparison between proton conducting electrolyte and oxygen ion conducting electrolyte*. Journal of Power Sources, 2008. **183**(1): p. 133-142.
11. Chan, S.H., K.A. Khor, and Z.T. Xia, *A complete polarization model of a solid oxide fuel cell and its sensitivity to the change of cell component thickness*. Journal of Power Sources, 2001. **93**(1–2): p. 130-140.
12. Chan, S. and Z. Xia, *Polarization effects in electrolyte/electrode-supported solid oxide fuel cells*. Journal of Applied Electrochemistry, 2002. **32**(3): p. 339-347.
13. Ni, M., D.Y.C. Leung, and M.K.H. Leung, *Importance of pressure gradient in*

solid oxide fuel cell electrodes for modeling study. Journal of Power Sources, 2008. **183**(2): p. 668-673.

14. Ni, M., D.Y.C. Leung, and M.K.H. Leung, *Electrochemical modeling and parametric study of methane fed solid oxide fuel cells.* Energy Conversion and Management, 2009. **50**(2): p. 268-278.
15. Wachsman, E.D. and K.T. Lee, *Lowering the Temperature of Solid Oxide Fuel Cells*. Science, 2011. **334**(6058): p. 935-939.
16. Wachsman, E.D., C.A. Marlowe, and K.T. Lee, *Role of solid oxide fuel cells in a balanced energy strategy*. Energy & Environmental Science, 2012. **5**(2): p. 5498-5509.
17. Maru, H.C., et al., *1-10 kW Stationary Combined Heat and Power Systems Status and Technical Potential: Independent Review*. 2010. p. Medium: ED; Size: 40 pp.
18. Jing, Y., et al., *Enhanced conductivity of SDC based nanocomposite electrolyte by spark plasma sintering*. International Journal of Hydrogen Energy, 2014. **39**(26): p. 14391-14396.
19. Medvedev, D.A., et al., *Advanced materials for SOFC application: Strategies for the development of highly conductive and stable solid oxide proton electrolytes*. Progress in Materials Science, 2016. **75**: p. 38-79.
20. Leng, Y.J., et al., *Low-temperature SOFC with thin film GDC electrolyte prepared in situ by solid-state reaction*. Solid State Ionics, 2004. **170**(1–2): p. 9-15.
21. Will, J., et al., *Fabrication of thin electrolytes for second-generation solid oxide fuel cells*. Solid State Ionics, 2000. **131**(1–2): p. 79-96.
22. Hong, S., et al., *High-performance ultra-thin film solid oxide fuel cell using anodized-aluminum-oxide supporting structure*. Electrochemistry Communications, 2014. **47**: p. 1-4.
23. Rossmeisl, J. and W.G. Bessler, *Trends in catalytic activity for SOFC anode materials*. Solid State Ionics, 2008. **178**(31–32): p. 1694-1700.
24. Choi, H., et al., *Effect of Ce Doping on the Performance and Stability of*

Strontium Cobalt Ferrite Perovskites as SOFC Anode Catalysts. Topics in Catalysis, 2015. **58**(4-6): p. 359-374.

25. Gorte, R.J. and J.M. Vohs, *Nanostructured anodes for solid oxide fuel cells.* Current Opinion in Colloid & Interface Science, 2009. **14**(4): p. 236-244.
26. Bellino, M.G., et al., *High-Performance Solid-Oxide Fuel Cell Cathodes Based on Cobaltite Nanotubes.* Journal of the American Chemical Society, 2007. **129**(11): p. 3066-3067.
27. Zhao, F. and A.V. Virkar, *Dependence of polarization in anode-supported solid oxide fuel cells on various cell parameters.* Journal of Power Sources, 2005. **141**(1): p. 79-95.
28. Demin, A. and P. Tsiakaras, *Thermodynamic analysis of a hydrogen fed solid oxide fuel cell based on a proton conductor.* International Journal of Hydrogen Energy, 2001. **26**(10): p. 1103-1108.
29. Ni, M., D.Y.C. Leung, and M.K.H. Leung, *An improved electrochemical model for the NH3 fed proton conducting solid oxide fuel cells at intermediate temperatures.* Journal of Power Sources, 2008. **185**(1): p. 233-240.
30. Ni, M., D.Y.C. Leung, and M.K.H. Leung, *Electrochemical modeling of ammonia-fed solid oxide fuel cells based on proton conducting electrolyte.* Journal of Power Sources, 2008. **183**(2): p. 687-692.
31. Iwahara, H., *Oxide-ionic and protonic conductors based on perovskite-type oxides and their possible applications.* Solid State Ionics, 1992. **52**(1-3): p. 99-104.
32. Iwahara, H., *High-temperature proton conducting oxides and their applications to solid electrolyte fuel-cells and steam electrolyzer for hydrogen-production.* Solid State Ionics, 1988. **28**: p. 573-578.
33. Iwahara, H., et al., *Performance of solid oxide fuel-cell using proton and oxide-ion mixed conductors based on* $BaCe_{1-x}Sm_xO_{3-a}$. Journal of the Electrochemical Society, 1993. **140**(6): p. 1687-1691.
34. Ni, M., M.K.H. Leung, and D.Y.C. Leung, *Micro-scale modelling of solid oxide fuel cells with micro-structurally graded electrodes.* Journal of Power

Sources, 2007. **168**(2): p. 369-378.

35. Ni, M., M.K.H. Leung, and D.Y.C. Leung, *Micro-scale modeling of a functionally graded Ni-YSZ anode*. Chemical Engineering & Technology, 2007. **30**(5): p. 587-592.
36. Wang, Z., et al., *Improved SOFC performance with continuously graded anode functional layer*. Electrochemistry Communications, 2009. **11**(6): p. 1120-1123.
37. Xia, C., et al., *Functionally Graded Cathodes for Honeycomb Solid Oxide Fuel Cells*. Electrochemical and Solid-State Letters, 2002. **5**(10): p. A217-A220.
38. Yang, Y.Z., et al., *Fabrication of functionally graded SOFC by APS*. Journal of Thermal Spray Technology, 2007. **16**(5-6): p. 768-775.
39. Liu, Y., C. Compson, and M. Liu, *Nanostructured and functionally graded cathodes for intermediate temperature solid oxide fuel cells*. Journal of Power Sources, 2004. **138**(1–2): p. 194-198.
40. Deseure, J., et al., *Modelling of a SOFC graded cathode*. Journal of the European Ceramic Society, 2005. **25**(12): p. 2673-2676.
41. Deseure, J., et al., *Micromodeling of functionally graded SOFC cathodes*. Journal of the Electrochemical Society, 2007. **154**(10): p. B1012-B1016.
42. Deseure, J., et al., *Theoretical optimisation of a SOFC composite cathode*. Electrochimica Acta, 2005. **50**(10): p. 2037-2046.
43. Greene, E.S., W.K.S. Chiu, and M.G. Medeiros, *Mass transfer in graded microstructure solid oxide fuel cell electrodes*. Journal of Power Sources, 2006. **161**(1): p. 225-231.
44. Anandakumar, G., et al., *Thermal stress and probability of failure analyses of functionally graded solid oxide fuel cells*. Journal of Power Sources, 2010. **195**(19): p. 6659-6670.
45. Hussain, M.M., X. Li, and I. Dincer, *A numerical investigation of modeling an SOFC electrode as two finite layers*. International Journal of Hydrogen Energy, 2009. **34**(7): p. 3134-3144.
46. Uchida, H., N. Maeda, and H. Iwahara, *Relation between proton and hole*

conduction in SrCeO3-based solid electrolytes under water-containing atmospheres at high-temperatures. Solid State Ionics, 1983. **11**(2): p. 117-124.

47. Gorbova, E., et al., *Charge transfer properties of BaCe0.88Nd0.12O3−δ co-ionic electrolyte*. Journal of Power Sources, 2006. **157**(2): p. 720-723.

48. Zhao, Y., et al., *Oxide ion and proton conduction in doped ceria–carbonate composite materials*. International Journal of Hydrogen Energy, 2013. **38**(3): p. 1553-1559.

49. Pérez-Coll, D., et al., *Transport-number determination of a protonic ceramic electrolyte membrane via electrode-polarisation correction with the Gorelov method*. Journal of Power Sources, 2014. **245**: p. 445-455.

50. Demin, A., et al., *A SOFC based on a co-ionic electrolyte*. Journal of Power Sources, 2004. **131**(1-2): p. 231-236.

51. Huang, J., et al., *Analysis and Modeling of Novel Low-Temperature SOFC With a Co-Ionic Conducting Ceria-Based Composite Electrolyte*. Journal of Fuel Cell Science and Technology, 2010. **7**(1).

52. Bavarian, M., et al., *Mathematical Modeling and Steady-State Analysis of a Co-Ionic-Conducting Solid Oxide Fuel Cell*. 2012 American Control Conference (Acc), 2012: p. 4269-4274.

53. Bavarian, M., M. Soroush, and Ieee, *Control of a Heat-Integrated Co-Ionic-Conducting Solid Oxide Fuel Cell System*. 2013 American Control Conference (Acc), 2013: p. 5356-5361.

54. Deng, X. and A. Petric, *Geometrical modeling of the triple-phase-boundary in solid oxide fuel cells*. Journal of Power Sources, 2005. **140**(2): p. 297-303.

55. Zhang, Y., C. Xia, and M. Ni, *Simulation of sintering kinetics and microstructure evolution of composite solid oxide fuel cells electrodes*. International Journal of Hydrogen Energy, 2012. **37**(4): p. 3392-3402.

56. Sunde, S., *Monte Carlo simulations of polarization resistance of composite electrodes for solid oxide fuel cells*. Journal of the Electrochemical Society, 1996. **143**(6): p. 1930-1939.

57. Gokhale, A., S. Zhang, and M. Liu, *A stochastic geometry based model for*

total triple phase boundary length in composite cathodes for solid oxide fuel cells. Journal of Power Sources, 2009. **194**(1): p. 303-312.

58. Kenney, B., et al., *Computation of TPB length, surface area and pore size from numerical reconstruction of composite solid oxide fuel cell electrodes.* Journal of Power Sources, 2009. **189**(2): p. 1051-1059.

59. Vivet, N., et al., *Effect of Ni content in SOFC Ni-YSZ cermets: A three-dimensional study by FIB-SEM tomography.* Journal of Power Sources, 2011. **196**(23): p. 9989-9997.

60. Shikazono, N., et al., *Numerical Assessment of SOFC Anode Polarization Based on Three-Dimensional Model Microstructure Reconstructed from FIB-SEM Images.* Journal of the Electrochemical Society, 2010. **157**(5): p. B665-B672.

61. Iwai, H., et al., *Quantification of SOFC anode microstructure based on dual beam FIB-SEM technique.* Journal of Power Sources, 2010. **195**(4): p. 955-961.

62. Rhazaoui, K., et al., *Towards the 3D Modelling of the Effective Conductivity of Solid Oxide Fuel Cell Electrodes – Validation against experimental measurements and prediction of electrochemical performance.* Electrochimica Acta, 2015. **168**: p. 139-147.

63. Vivet, N., et al., *3D Microstructural characterization of a solid oxide fuel cell anode reconstructed by focused ion beam tomography.* Journal of Power Sources, 2011. **196**(18): p. 7541-7549.

64. Choi, H.W., et al., *Effective transport properties of the porous electrodes in solid oxide fuel cells.* Proceedings of the Institution of Mechanical Engineers Part a-Journal of Power and Energy, 2011. **225**(A2): p. 183-197.

65. Sanyal, J., et al., *A particle-based model for predicting the effective conductivities of composite electrodes.* Journal of Power Sources, 2010. **195**(19): p. 6671-6679.

66. Chen, D., et al., *Percolation theory to predict effective properties of solid oxide fuel-cell composite electrodes.* Journal of Power Sources, 2009. **191**(2): p. 240-252.

67. Suzuki, M. and T. Oshima, *Estimation of the Co-ordination number in a Multi-Component Mixture of Spheres*. Powder Technology, 1983. **35**(2): p. 159-166.

68. Bouvard, D. and F.F. Lange, *Relation between percolation and particle coordination in binary powder mixtures*. Acta Metallurgica et Materialia, 1991. **39**(12): p. 3083-3090.

69. Chen, D., et al., *Percolation micro-model to predict the effective properties of the composite electrode with poly-dispersed particle sizes*. Journal of Power Sources, 2011. **196**(6): p. 3178-3185.

70. Bertei, A. and C. Nicolella, *Percolation theory in SOFC composite electrodes: Effects of porosity and particle size distribution on effective properties*. Journal of Power Sources, 2011. **196**(22): p. 9429-9436.

71. Bertei, A. and C. Nicolella, *A comparative study and an extended theory of percolation for random packings of rigid spheres*. Powder Technology, 2011. **213**(1–3): p. 100-108.

72. Bertei, A., et al., *Percolating behavior of sintered random packings of spheres*. Powder Technology, 2012. **231**: p. 44-53.

73. Rhazaoui, K., et al., *Towards the 3D modeling of the effective conductivity of solid oxide fuel cell electrodes: I. Model development*. Chemical Engineering Science, 2013. **99**: p. 161-170.

74. Rhazaoui, K., et al., *Towards the 3D modeling of the effective conductivity of solid oxide fuel cell electrodes – II. Computational parameters*. Chemical Engineering Science, 2014. **116**: p. 781-792.

75. Bertei, A., B. Nucci, and C. Nicolella, *Microstructural modeling for prediction of transport properties and electrochemical performance in SOFC composite electrodes*. Chemical Engineering Science, 2013. **101**: p. 175-190.

76. Kenney, B., et al., *Computation of TPB length, surface area and pore size from numerical reconstruction of composite solid oxide fuel cell electrodes*. Journal of Power Sources, 2009. **189**(2): p. 1051-1059.

77. Nam, J.H. and D.H. Jeon, *A comprehensive micro-scale model for transport*

and reaction in intermediate temperature solid oxide fuel cells. Electrochimica Acta, 2006. **51**(17): p. 3446-3460.

78. Fukunaga, H., M. Ishino, and K. Yamada, *Effective thickness of Ni-Sm-doped ceria cermet anode for solid oxide fuel cell*. Electrochemical and Solid State Letters, 2007. **10**(1): p. B16-B18.

79. Menzler, N.H. and V.A.C. Haanappel, *Influence of anode thickness on the power output of solid oxide fuel cells with (La,Sr)(Co,Fe)-type cathode*. Journal of Power Sources, 2010. **195**(16): p. 5340-5343.

80. Suzue, Y., N. Shikazono, and N. Kasagi, *Micro modeling of solid oxide fuel cell anode based on stochastic reconstruction*. Journal of Power Sources, 2008. **184**(1): p. 52-59.

81. Primdahl, S. and M. Mogensen, *Oxidation of hydrogen on Ni/yttria-stabilized zirconia cermet anodes*. Journal of the Electrochemical Society, 1997. **144**(10): p. 3409-3419.

82. Xia, Z.T., S.H. Chan, and K.A. Khor, *An improved anode micro model of SOFC*. Electrochemical and Solid State Letters, 2004. **7**(3): p. A63-A65.

83. Chan, S.H. and Z.T. Xia, *Anode micro model of solid oxide fuel cell*. Journal of the Electrochemical Society, 2001. **148**(4): p. A388-A394.

84. Abudula, A., et al., *Oxidation mechanism and effective anode thickness of SOFC for dry methane fuel*. Solid State Ionics, 1996. **86-8**: p. 1203-1209.

85. Tanner, C.W., K.Z. Fung, and A.V. Virkar, *The effect of porous composite electrode structure on solid oxide fuel cell performance .1. Theoretical analysis*. Journal of the Electrochemical Society, 1997. **144**(1): p. 21-30.

86. Kawada, T., et al., *Structure and polarization characteristics of solid oxide fuel-cell anodes*. Solid State Ionics, 1990. **40-1**: p. 402-406.

87. Koyama, M., et al., *The mechanism of porous Sm0.5Sr0.5CoO3 cathodes used in solid oxide fuel cells*. Journal of the Electrochemical Society, 2001. **148**(7): p. A795-A801.

88. Brown, M., S. Primdahl, and M. Mogensen, *Structure/performance relations for Ni/yttria-stabilized zirconia anodes for solid oxide fuel cells*. Journal of the

Electrochemical Society, 2000. **147**(2): p. 475-485.

89. Lu, Z., et al., *Extended reaction zone of La0.6Sr0.4Co0.2Fe0.8O3 cathode for solid oxide fuel cell.* Journal of Power Sources, 2012. **198**: p. 90-94.

90. Chan, S.H., X.J. Chen, and K.A. Khor, *Cathode micromodel of solid oxide fuel cell.* Journal of the Electrochemical Society, 2004. **151**(1): p. A164-A172.

91. Costamagna, P., P. Costa, and V. Antonucci, *Micro-modelling of solid oxide fuel cell electrodes*. Electrochimica Acta, 1998. **43**(3-4): p. 375-394.

92. Chen, D., et al., *Combined micro-scale and macro-scale modeling of the composite electrode of a solid oxide fuel cell.* Journal of Power Sources, 2010. **195**(19): p. 6598-6610.

93. Kenjo, T., S. Osawa, and K. Fujikawa, *High-temperature air cathodes containing ion conductive oxides*. Journal of the Electrochemical Society, 1991. **138**(2): p. 349-355.

94. Jiang, Z.-y., C.-r. Xia, and F.-l. Chen, *Efficient Thickness of Solid Oxide Fuel Cell Composite Electrode*. Chinese Journal of Chemical Physics, 2010. **23**(2): p. 217-225.

95. Zheng, K.-Q., et al., *Mathematical analysis of SOFC based on co-ionic conducting electrolyte*. Acta Mechanica Sinica, 2013. **29**(3): p. 388-394.

96. Huang, J., Z. Gao, and Z. Mao, *Effects of salt composition on the electrical properties of samaria-doped ceria/carbonate composite electrolytes for low-temperature SOFCs.* International Journal of Hydrogen Energy, 2010. **35**(9): p. 4270-4275.

97. Zhao, Y., et al., *Nanocomposite electrode materials for low temperature solid oxide fuel cells using the ceria-carbonate composite electrolytes.* International Journal of Hydrogen Energy, 2012. **37**(24): p. 19351-19356.

98. Ni, M., *2D thermal-fluid modeling and parametric analysis of a planar solid oxide fuel cell.* Energy Conversion and Management, 2010. **51**(4): p. 714-721.

99. Suwanwarangkul, R., et al., *Performance comparison of Fick's, dusty-gas and Stefan–Maxwell models to predict the concentration overpotential of a SOFC anode*. Journal of Power Sources, 2003. **122**(1): p. 9-18.

100. Kong, W., et al., *A modified dusty gas model in the form of a Fick's model for the prediction of multicomponent mass transport in a solid oxide fuel cell anode*. Journal of Power Sources, 2012. **206**: p. 171-178.

101. Todd, B. and J.B. Young, *Thermodynamic and transport properties of gases for use in solid oxide fuel cell modelling*. Journal of Power Sources, 2002. **110**(1): p. 186-200.

102. Poling, B.E., J.M. Prausnitz, and J.P. O'connell, *The properties of gases and liquids*. Vol. 5. 2001: McGraw-Hill.

103. Hernández-Pacheco, E., et al., *A macro-level model for determining the performance characteristics of solid oxide fuel cells*. Journal of Power Sources, 2004. **138**(1–2): p. 174-186.

104. Tseronis, K., I.K. Kookos, and C. Theodoropoulos, *Modelling mass transport in solid oxide fuel cell anodes: a case for a multidimensional dusty gas-based model*. Chemical Engineering Science, 2008. **63**(23): p. 5626-5638.

105. Shen, S. and M. Ni, *2D segment model for a solid oxide fuel cell with a mixed ionic and electronic conductor as electrolyte*. International Journal of Hydrogen Energy, 2015. **40**(15): p. 5160-5168.

106. Haberman, B.A. and J.B. Young, *Three-dimensional simulation of chemically reacting gas flows in the porous support structure of an integrated-planar solid oxide fuel cell*. International Journal of Heat and Mass Transfer, 2004. **47**(17–18): p. 3617-3629.

107. Ni, M., *Is steam addition necessary for the landfill gas fueled solid oxide fuel cells?* International Journal of Hydrogen Energy, 2013. **38**(36): p. 16373-16386.

108. Matsuzaki, Y. and I. Yasuda, *Electrochemical Oxidation of H2 and CO in a H2-H2O-CO-CO2 System at the Interface of a Ni-YSZ Cermet Electrode and YSZ Electrolyte*. Journal of the Electrochemical Society, 2000. **147**(5): p. 1630-1635.

109. Ni, M., *Modeling of SOFC running on partially pre-reformed gas mixture*. International Journal of Hydrogen Energy, 2012. **37**(2): p. 1731-1745.

110. Alcock, C.B., J. Butler, and E. Ichise, *A vapour pressure technique for the determination of the oxygen transport number of a solid oxide electrolyte.* Solid State Ionics, 1981. **3–4**: p. 499-502.

111. Wu, Z. and M. Liu, *Modelling of ambipolar transport properties of composite mixed ionic-electronic conductors.* Solid State Ionics, 1996. **93**(1–2): p. 65-84.

112. Tian, D., et al., *Low-temperature co-sintering of co-ionic conducting solid oxide fuel cells based on* $Ce_{0.8}Sm_{0.2}O_{1.9}$-$BaCe_{0.8}Sm_{0.2}O_{2.9}$ *composite electrolyte.* Ionics, 2015. **21**(3): p. 823-828.

113. Zheng, K., et al., *On the tortuosity factor of solid phase in solid oxide fuel cell electrodes.* International Journal of Hydrogen Energy, 2015. **40**(1): p. 665-669.

114. Yamahara, K., et al., *Ionic conductivity of stabilized zirconia networks in composite SOFC electrodes.* Solid State Ionics, 2005. **176**(15–16): p. 1359-1364.

115. Zhang, Y., et al., *A Sintering Kinetics Model for Ceramic Dual-Phase Composite.* Journal of the American Ceramic Society, 2014. **97**(8): p. 2580-2589.

116. Cai, Q., C.S. Adjiman, and N.P. Brandon, *Modelling the 3D microstructure and performance of solid oxide fuel cell electrodes: Computational parameters.* Electrochimica Acta, 2011. **56**(16): p. 5804-5814.

117. Zhang, Y. and C. Xia, *Film percolation for composite electrodes of solid oxide fuel cells.* Electrochimica Acta, 2011. **56**(13): p. 4763-4769.

118. Yu, J.H., et al., *Microstructural effects on the electrical and mechanical properties of Ni–YSZ cermet for SOFC anode.* Journal of Power Sources, 2007. **163**(2): p. 926-932.

119. Zhang, Y., et al., *Geometric Properties of Nanostructured Solid Oxide Fuel Cell Electrodes.* Journal of the Electrochemical Society, 2013. **160**(3): p. F278-F289.

120. Zhang, Y., C. Xia, and F. Chen, *Tortuosity factor of three-dimensional infiltrate network.* Journal of Power Sources, 2014. **269**: p. 189-193.

121. Jiang, S.P., *A review of wet impregnation—An alternative method for the*

fabrication of high performance and nano-structured electrodes of solid oxide fuel cells. Materials Science and Engineering: A, 2006. **418**(1–2): p. 199-210.

122. Zheng, K., L. Li, and M. Ni, *Investigation of the electrochemical active thickness of solid oxide fuel cell anode*. International Journal of Hydrogen Energy, 2014. **39**(24): p. 12904-12912.
123. Vural, Y., et al., *Comparison of the multicomponent mass transfer models for the prediction of the concentration overpotential for solid oxide fuel cell anodes*. Journal of Power Sources, 2010. **195**(15): p. 4893-4904.
124. García-Camprubí, M., A. Sánchez-Insa, and N. Fueyo, *Multimodal mass transfer in solid-oxide fuel-cells*. Chemical Engineering Science, 2010. **65**(5): p. 1668-1677.
125. Ho, T.X., et al., *Modeling of transport, chemical and electrochemical phenomena in a cathode-supported SOFC*. Chemical Engineering Science, 2009. **64**(12): p. 3000-3009.
126. Xia, Z.T., S.H. Chan, and K.A. Khor *An Improved Anode Micro Model of SOFC*. Electrochemical and Solid-State Letters, 2004. **7**(3): p. A63-A65.
127. Cai, Q., C.S. Adjiman, and N.P. Brandon, *Investigation of the active thickness of solid oxide fuel cell electrodes using a 3D microstructure model*. Electrochimica Acta, 2011. **56**(28): p. 10809-10819.
128. Ferguson, J.R., J.M. Fiard, and R. Herbin, *Three-dimensional numerical simulation for various geometries of solid oxide fuel cells*. Journal of Power Sources, 1996. **58**(2): p. 109-122.
129. Anselmi-Tamburini, U., et al., *Electrical properties of Ni/YSZ cermets obtained through combustion synthesis*. Solid State Ionics, 1998. **110**(1-2): p. 35-43.
130. Kiatkittipong, W., et al., *Oxygen transport through LSM/YSZ/LaAlO system for use of fuel cell type reactor*. Chemical Engineering Journal, 2005. **106**(1): p. 35-42.